Detection of Low Velocity Micrometeoroids and Space Debris impacts

An Experimental Investigation

Yurij Pettinari

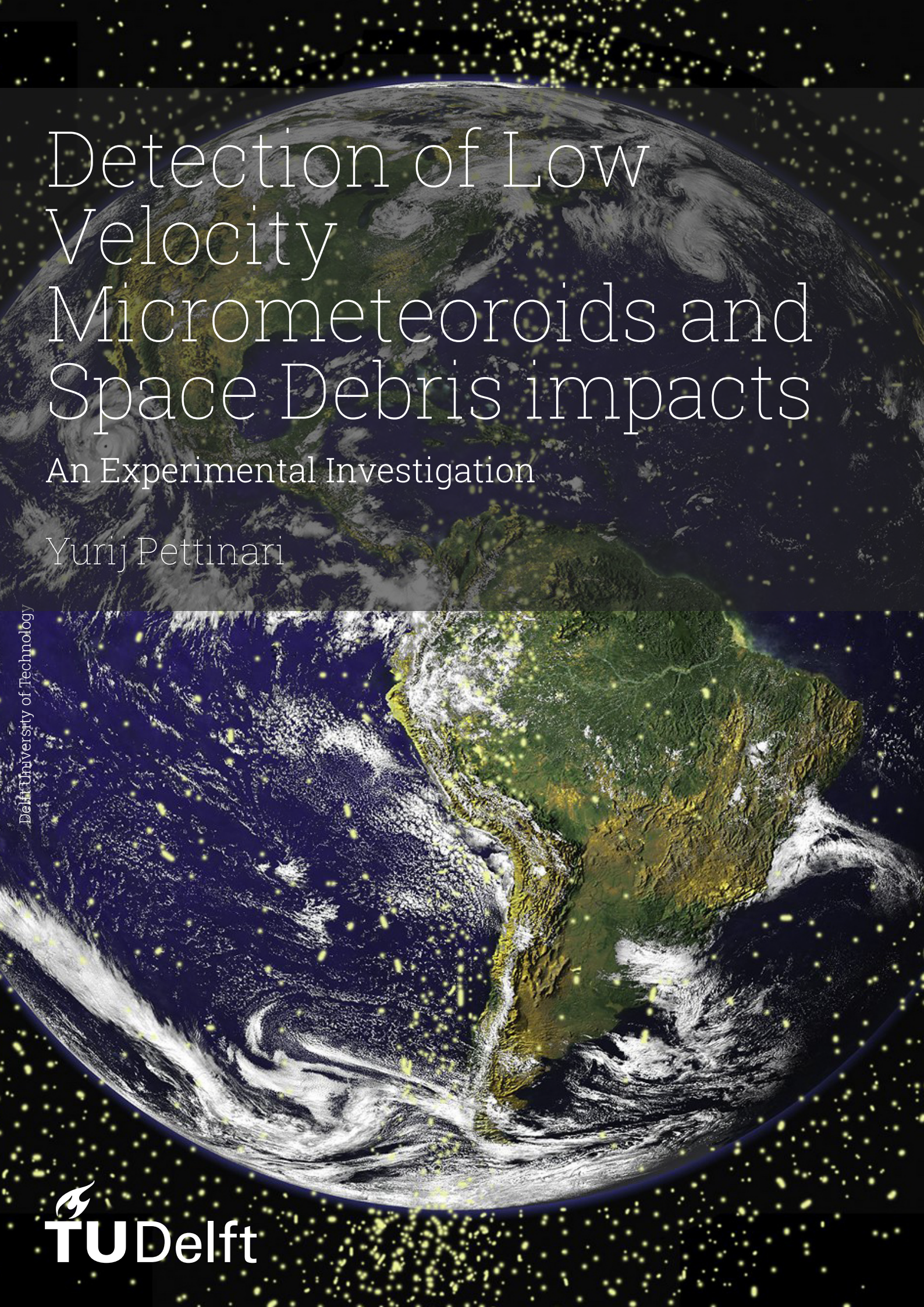

Delft University of Technology

TU Delft

Detection of Low Velocity Micrometeoroids and Space Debris impacts

An Experimental Investigation

by

Yurij Pettinari

Yurij Pettinari 5259061

Instructor: Bert Vermeersen & Håkan Svedhem
Faculty of Aerospace Engineering, Department of Astrodynamics and Space Missions

TU Delft

Preface

As I sit down to write these acknowledgements, I am struck by how much has changed since I began this journey almost three years ago. I left my home country, my comfort zone, and my loved ones to start a new adventure in an unfamiliar land. In the years that followed, I experienced both triumphs and setbacks, made new friends, and learned countless lessons. Now, as I reflect on my master's thesis, I feel a sense of gratefulness for the people that helped me along the way.

I would like to express my deep gratitude to my family for their unwavering love and support throughout my master's program, especially as I pursued it abroad and away from them. Their encouragement and faith in me at all times helped me when life was not going as I had planned it.

I would like to extend my sincere appreciation to my supervisor, Ir. Svedhem. From arranging the use of the setup at ESTEC to helping me with research, even when it just meant figuring out why the accelerator broke down, I am thankful for having had you as support throughout my research project.

I would also like to thank my boyfriend Pepijn, your love and support have been essential during the ups and downs of this master's program. From late-night talks to surprise care packages, you always knew how to lift my spirits and keep me going. Your presence has been a source of comfort and motivation, and I am grateful for your understanding and encouragement.

I would like to express my gratitude to the people i met at ESTEC for making me feel welcome and supported. I would like to thank Bruno for his support in getting me started with the research, from helping me obtain a badge to ordering all the necessary tools for my project. I also want to thank all the other people that I met in the lab: they were always willing to assist me with my questions and help me when I was not sure about how to handle something.

Finally, I want to express my appreciation for my friends: those that supported me from Italy and those that I made during my time in Delft. Despite the start of the programme during COVID restrictions I met a lot of amazing people. I will always remember the late nights on teams, the endless discussions, the pizzas, trips to Rijswijk, bouldering nights and all the other moments shared together. Your help, be it an answer to a question about orbits or a call in the evening when I was feeling down, was invaluable and I am thankful for having you in my life. I would also like to thank Benni, started as my mentor during the introduction week and turned friend along the way: thank you for always being willing to answer my questions and being a role model throughout my time here in Delft.

In conclusion, I would like to thank everyone who has supported me throughout this journey. Your contributions have been significant, and I could not have done it without you.

Yurij Pettinari
Delft, April 2023

Abstract

Space debris and micrometeoroids are abundant around our home planet and offer both an opportunity of research for scientists and a threat to human's endeavours in space. Impacts with even the smallest particles can happen at such high velocities that they can damage or destroy an operational spacecraft, creating even more debris and possibly endangering its crew, if manned. Detecting and cataloguing the debris and micrometeoroid population has thus been a priority for many space agencies around the world to ensure safe space access. Unfortunately, small debris in high orbits cannot be detected by ground based observatories that can detect objects with a minimum diameter of 10 cm in LEO and 1m in GEO. This is why space based detectors are needed. Current detectors are small in size and can often detect only high velocity impacts due to relying on ionisation of particles upon impact. This MSc thesis investigated the possibility of using the whole spacecraft as a detector, by employing vibration sensors on its structure to detect impact-induced oscillations. These vibrations could contain information on the impactor's mass, speed, material class and other features. Impacts of pieces of debris were simulated in a laboratory environment and the vibrations generated in a spacecraft-like structure were measured and processed to study the effectiveness of such a detection method. Three types of projectiles were used, beads of glass (3mm diameter, 0.04g average mass), teflon (3.2 mm average diameter and 0.033g average mass) and steel (3 mm average diameter and 0.11 g average mass). As target, to represent a spacecraft, a 3mm thick aluminium panel, a 5 mm thick aluminium-skin aluminium-honeycomb sandwich panel and a flight spare model of a solar array were used. An impact-location estimation algorithm was developed that can successfully determine the point of impact based on the signal of at least 4 sensors with centimetre accuracy. Analysis of the waveforms acquired by the sensors showed that deformation phenomena upon impact affect the frequency content of the signal, showing that to preserve as much as possible the high frequency content of the signal stiffer parts of a satellite are more indicated for this type of technology. Lastly, it was observed that the maximum voltage measured grows linearly with the momentum of the particles, making it possible to estimate the impact momentum solely based on the signal acquired. The dependence of voltage from the impact momentum together with the experimentally calculated coefficient of vibration dissipation of -0.05 cm^{-1} was used to determine the maximum distance of sensors from the point of impact as a function of particle speed and mass for successful detection of the impact. Particles as light as 0.03 g (the lightest used in the experiments) travelling at speeds as low as 15 m/s are expected to be detectable from sensors as far as 50cm, while for objects of 0.2 g travelling at speeds exceeding 200 m/s it is expected that a sensor can be as far as 1 meter away from the point of impact. The method, for its simplicity and low-cost provides an easy way to greatly increase the amount of data on small pieces of debris and micrometeoroid around our planet, enhancing space exploration safety and supporting future missions.

Contents

Acronyms

AE Acoustic Emission. 2, 6, 7, 42, 75

BNC Bayonet Neill–Concelman. 17, 85

CDA Cassini Dust Analyser. 6

DLR Deutsches Zentrum für Luft-und-Raumfahrt. 10, 65

EM Electromagnetic. 13, 15, 29, 85
ESA European Space Agency. 4, 7–9, 13, 16
ESTEC European Space Research and Technology Centre. ii, 2, 8, 12, 13
EuReCa European Retrievable Carrier. 9

GEO Geosynchronous Equatorial Orbit. 1, 4, 11, 12
GIADA Grain Impact Analyser and Dust Accumulator. 7
GNSS Global Navigation Satellite System. 37, 38
GPS Global Positioning System. 33

ISS International Space Station. 9, 16, 75

LDEF Long Duration Exposure Facility. 7
LEO Low Earth Orbit. 1, 7

MASTER Meteoroid and Space Debris Terrestrial Environment Reference. xiii, 8, 9
MLI Multi Layer Insulation. 80

NASA National Aeronautics and Space Administration. 7–9

ORDEM ORbital Debris Engineering Model. xiii, 8, 9
OTS Orbital Test Satellites. 69

PTFE Polytetrafluoroethylene. xi, xiii, 43, 46, 47, 49, 51, 54, 57, 59–61, 63, 79

SDMM Space Debris and Micrometeoroid. 75
SHM Structural Health Monitoring. 9, 80
SUDA SUrface Dust Analyser. 6

List of Figures

List of Tables

1

Introduction

Ever since the first successful satellite started orbiting the Earth in 1957, the mass of man-made objects in space has been steadily increasing while the mass that makes it back to Earth is just a fraction of that [1]. All of these objects, including weather satellites, space stations, science spacecraft and so on, when out of use become part of the so called *space debris* population. Space debris, which comprises not only non-operational satellites but also pieces of satellites that are the results of collision, explosion or material degradation, has been increasing in number, mass and volume steadily since the start of the space age. Space debris is a risk for any future space mission we, as humans, will launch and even more so for manned missions that so many public and private organisations are working on right now. But space debris is not the only class of objects that can impact a spacecraft: our home planet is orbited by a variety of natural objects including dust and micrometeoroid that pose a threat to our endeavours in space.

Given the risk of impact that can range from damage to systems and subsystems to complete destruction of the spacecraft, space agencies and private companies are investing more and more resources in detecting, tracking, avoiding debris and micrometeoroid impacts and protecting satellites in case an impact happens. Objects bigger than 10 cm in LEO and 1m in GEO can be accurately tracked from ground based detectors [2], and the information can be used to perform collision avoidance manoeuvres or plan trajectories with low collision risk. Small debris are hard (if not impossible) to track and their orbits difficult to model. Nonetheless, given the damage that even the smallest objects can cause it is important to assess the risk of collision if not in a deterministic way (via tracking) via a probabilistic or statistical approach. This is what led space agencies across the world to develop space debris and micrometeoroid populations models. These are tools that help assess the flux of debris and micrometeoroids given an orbit: the mass, velocity and orbit distribution of the impacts can be obtained as output.

These models are an important tool in the development process of space missions as they allow engineers to assess the risk of collision for the orbit chosen. These models are data-driven: what this means is that they are built based on real observations of debris and micrometeoroid and that the output of the model should match the real observations that were used to develop it. For small objects the input are scarce and come mostly from LEO detectors. This means that for LEO the output debris flux is most often generated by extrapolation of data for big debris size in the same orbit, while for GEO data the extrapolation is based on detectors in Low Earth Orbit, resulting in estimations that are not necessarily close to reality.

Current detectors in space suffer from a number of limitations, namely small size and minimum impact speed threshold. With many of the detectors relying on impact ionisation for a successful detection, any impact below 1-1.3 km/s is de-facto invisible to the instrument. Although these instruments can provide a detailed analysis of the impactor, in terms of composition, mass and impact speed, the limited number of detectors results in sparse data.

What if we could solve the problem of limited data on small debris and micrometeoroid by transforming every satellite into a detector? Instead of equipping satellites with complex and expensive instruments, what if the spacecraft itself could act as a detector? This is what this thesis tried to investigate and study. Every time a spacecraft is impacted, no matter where, vibrations are generated in the structure, these

vibrations could contain information on the impactor. Using Acoustic Emission (AE) for the detection of debris and micrometeoroids would solve many of the issues of current detectors. The detection area would be the whole satellite surface, there is no minimum impact speed required and any spacecraft can be equipped with vibration sensors so that most orbits would benefit from this, it would be sufficient to place on the spacecraft structure vibration sensors, cheap and widely available, or reuse the accelerometers already present as part of the test campaign prior to any launch.
An electromagnetic accelerator was used to simulate debris and micrometeoroid impacts at the TEC-QEE laboratories of ESTEC. A target plate representing the side panel of a spacecraft was designed and built and impacted with projectiles of different materials at different speeds in the low-velocity regime. Piezo-sensors were mounted on the target plate to detect the vibrations that would then be processed using time-frequency analysis tools. At a later stage in the research a flight spare model of a solar array was used as a target.
The simplicity of the detection method would allow for its use on virtually any satellite. The detection method lacks the resolution offered by more advanced detectors but it compensates with the collection of orders of magnitude more data points that can be used to give us a much more detailed knowledge of the space debris and micrometeoroids environment around our planet: this can be used to validate existing debris and micrometeoroid models.

2

Literature review

This chapter will review past and current literature relevant for the research done during the master thesis. In particular the following topics will be reviewed:

- Space dust, micrometeoroids and space debris
- In-situ detection of space debris and micrometeoroids
- Impact detection on space structures
- Vibration of plate-like structures

2.1. Space dust, micrometeoroids and space debris

The environment around our planet is surrounded by a variety of objects of different size, mass and speed of both natural and artificial origin. These objects pose a threat to human space activities as a collision between a spacecraft and an object at orbital velocities will damage (or even destroy) the spacecraft [3]. Impacts between spacecraft and these objects happen at orbital speeds: in addition to damaging the spacecraft itself, new debris is created increasing the collision risk for future missions [4].

2.1.1. Space Debris

Space debris refers to man-made objects in space that serve no useful purpose. This includes objects of different types and sizes: from non-operational satellites, expended fuel tanks, rocket upper stages, to small residuals of solid rocket burns, paint chips and other small particles. As the number of debris grows every year, so does the probability of collision (Figure 2.1 shows the result of such a collision with the window of the Challenger Space Shuttle). Over the past two decades on average more than 12 fragmentation events happen every year [1]. This is why it is important to both monitor the current population of space debris and work on strategies to limit the amount of debris left in orbit with every space mission. The danger posed by space debris has been known for decades now [5] but only lately space agencies and private companies are really focusing on solutions to this issue [6].

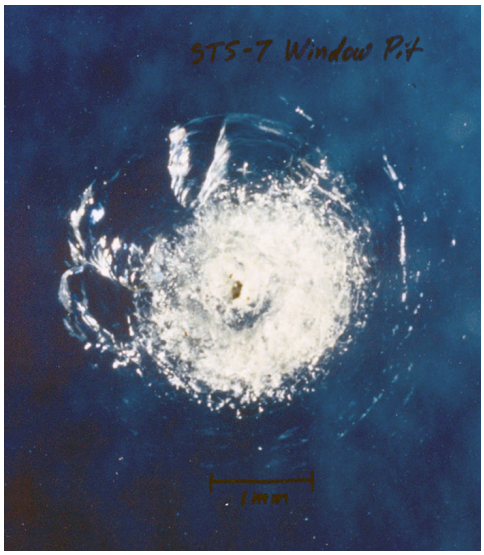

Figure 2.1: Crack on the Space Shuttle Challenger due to a debris impact. Credits: NASA.

As of today, May 2023, space debris far outweighs operational spacecraft in number, mass and volume [7]. Figure 2.2 shows the total number of objects tracked around our planet compared to the number of payloads: the difference is made up of expended rocket bodies, debris, decommissioned satellites and unknown objects. It can be clearly

seen how payloads represent less than half of the total amount of objects. The plot also shows sharp increases in objects tracked that are often the result of fragmentation events, like the Cosmos-Iridium collision in 2009 [8].

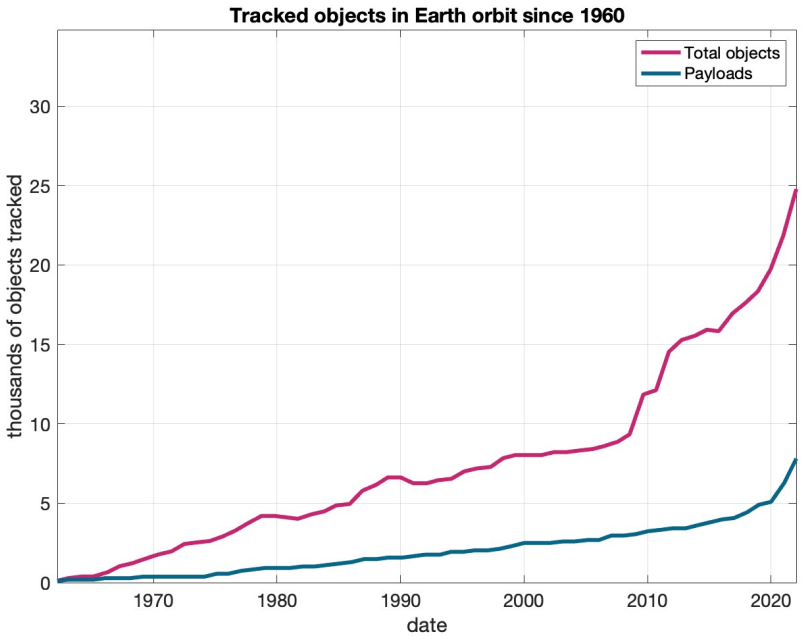

Figure 2.2: Tracked objects in Earth orbit [1]

Debris can be categorised based on their origin. Folliwing ESA's classification [9], the following categories can be listed:

- **Propulsion**: result of accidental explosions due to fuel left undisposed on satellites
- **Deliberate**: intentional breakup events due to anti-satellite missile tests, detonation as end-of-life strategy or due to non-nominal operations
- **Anomalous**: Non-planned separation of parts of a spacecraft due to material degradation (paint chips, solar panels, insulation material..)
- **Collision**: this includes collision between spacecraft, or between debris and a spacecraft
- **Electrical**: Design flows that lead to breakup events
- **Aerodynamics**: for low-altitude satellites, atmospheric drag can create overpressure that leads to breakup
- **Unknown**: almost 15% of debris is of unknown origin due to lack of information needed for its classification

Debris in different orbits have different properties, in terms of orbit, behaviour and dynamics.For example, GEO region is becoming more and more crowded due to its attractiveness for satellite communication missions and no natural cleanup mechanism (like aerodynamic drag at lower altitudes). Due to small perturbing forces acting on objects at these altitudes, debris due to perigee raising, material degradation and solid rocket firing tend to reside in the same orbit of the generating body.

Debris come in different sizes requiring different tracking technologies. The bigger the debris the easier it is to track as radars and optical telescopes can be used. Unfortunately, smaller debris are much more abundant than bigger debris, as Figure 2.3 shows.

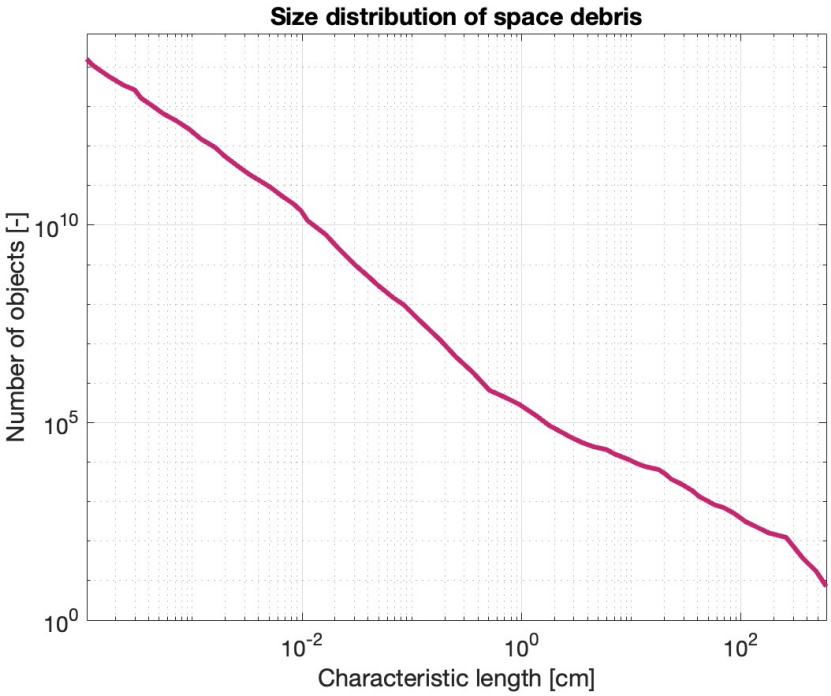

Figure 2.3: Size distribution of space debris [10].

2.1.2. Space Dust and Micrometeoroids

Space Dust and micrometeoroids are some of the natural bodies that can be found orbiting our planet. Objects below hundreds of micrometers are classified as dust, objects bigger than dust but smaller than meteoroids are classified as micrometeoroids.
The first studies on space dust started already at the end of the 17th century, when scientist looking at the night sky noticed what they would call ”zodiacal light”[11]. Initial observation, due to the available instruments, mostly focused on its appearance. Zodiacal light was found to be the result of space dust reflecting and refracting light from the Sun only when measurement of light polarisation became available[12]. Despite the advancements in knowledge, the faint light observed combined with air distortion and noise and light pollution on Earth make ground-based observations difficult. This is why the advent of the space age allowed for new instruments and measurement techniques to be used to study space dust not only in Earth’s neighbourhood (1 AU) but also across the solar system. Pioneer 10 and 11, for example, helped map space dust distribution during their mission[13] [14].
Space dust, like any body in the solar system, is subject to the gravitational influence of the bodies surrounding it. Due to its small size (and thus high area to mass ratio), space dust is heavily influenced by solar radiation [15]. Another important effect, for dust grains from $1\mu m$ to $1mm$ is the Poyinting-Robertson effect [15] [16].

Based on the combination of size of the dust grain and its distance from the Sun the dust may spiral into the Sun due to loss of orbital angular momentum, have a larger and larger orbit until it is blown out of the Solar System or have its orbit changed due to impacts with other bodies.
Dust particles in the inner solar system have an average life of 10^6 years [17], the fact that dust is present today and was present in the Solar System for billions of years [18] means that there has to be a constant resupply of dust keeping the total amount of cosmic dust in the Solar System in a quasi equilibrium that is believed to be mostly due to comets [19] and large meteoroids [20].
The cosmic dust replenishment mechanism is not completely understood: comets on unbound or highly elliptical orbits are not able to eject dust that stays in orbit around the Sun [21], while short-period comets that have the ability to release dust in Sun-bound orbits are not abundant enough [19]. It is thus believed that dust is also generated as fragmentation of bigger parts released by comets [22].

2.2. In-situ debris and micrometeoroid detection

Given the interest in the debris and natural bodies population around our planet and in our galaxy, since the beginning of the space age various detection techniques have been developed. A first classification can be made based on the location of the detector: ground based detection and in-situ detection. Although ground-based detectors are able to track and detect a higher amount of objects, smaller debris can only be detected from space [2].Considering the scope of the thesis only the second category will be analysed.
In-situ detectors can be further differentiated in active and passive detectors. Active detectors rely on sensors to study the objects they interact with while passive detectors only act as collectors of material that has to be retrieved from space to be inspected to obtain a time-integrated value for the debris and micrometeoroid flux.
The average number of objects interacting with a spacecraft is given by Equation 2.1 [23]:

$$N = F \cdot A \cdot \Delta t \tag{2.1}$$

Where F is the debris and/or micrometeoroid flux, A is the cross section of the spacecraft (or detector) and Δt is the time period considered. From the equation it follows that in order to increase the amount of data points collected one or more of the parameters of the equations should be increased. The flux depends on the orbit considered, so for a given orbit bigger detector or longer mission lifetimes would allow for an increased detection rate.
For detection to happen, the debris or micrometeoroid has to interact with the detector: i.e. an impact has to happen. The impact velocity is given by the magnitude of the difference of the velocity vector of the detector and the objects being detected. This is why, despite orbital speeds being around 10 km/s, relative velocities between the detector and detected objects can be as low as tens of meters per second and as high as 20 km/s or more.

2.2.1. Active Detection

A variety of active detection techniques exist used for different application. Even instruments based on the same physical phenomenon can have different characteristics based on how the phenomenon is used to obtain data. This is why an overview of the most common detection strategies will be given, with some notable examples of instruments that have been flown.

Time-of-flight mass spectrometer

As the name suggest, this detectors measures the time it takes for a particle to go from one point to another within the detector. In order for detection to be successful the impactor has to hit the detector with enough energy to undergo ionisation.
Usually an ionisation detector starts the time measurement. The ionisation process generates charged particles that can interact with the electromagnetic field within the detector. The trajectory of the particle, and thus it's time of flight, is proportional to the mass to charge ratio: this is unique for each element and allows to characterise the composition of the debris or micrometeoroid. Notable examples of this type of detector are Cassini's Cassini Dust Analyser (CDA) and SUrface Dust Analyser (SUDA) set to launch on Europa Clipper in 2024[24].
Figure 2.4, based on the Europa Clipper's SUDA shows the most important elements making up such a detector. The reflector grid prevents electrons and particles without sufficient kinetic energy from entering the detector with an electrostatic field. Once the particle hits the detector it undergoes an ionisation process: this starts the time measurement. The generated charged particles then hit a secondary detector, stopping the time measurement. Slow particles are invisible to this detector as they do not have the necessary kinetic energy to undergo ionisation.

Acoustic Detection

This class of detectors is based on Acoustic Emission (AE): vibrations in materials due to impacts. Sensors (pieoelectric, optical, accelerometers) can be used to detect these vibrations. If more than 3 sensors are used, multilateration algorithms can be used to identify the impact location. Studies have been done with two layers of material [27] that can be penetrated by the debris or microemeteoroid. Locating the impact on the two layers of the detector allows for the identification of the trajectory of the particle. The hurdle to overcome when developing a detector of this type consists in finding materials

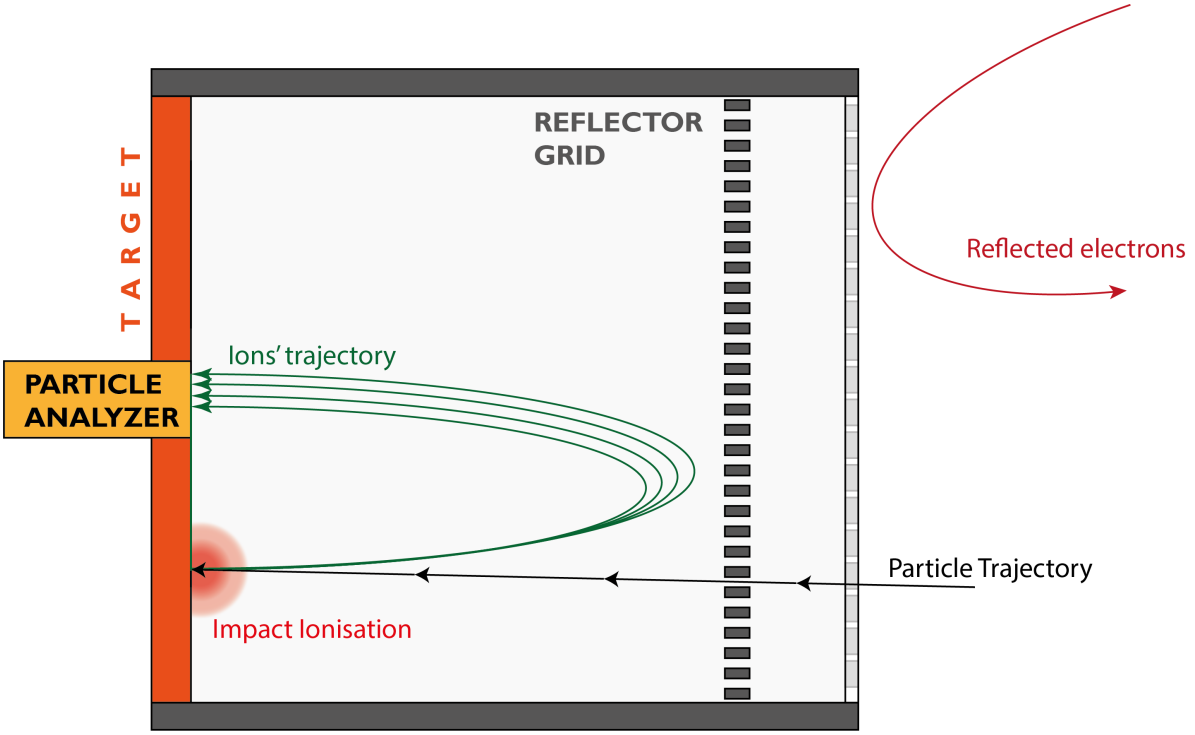

Figure 2.4: Basic elements in a (refelctron) time of flight mass spectrometer for space applications. Illustration based on the SUDA dust analyzer [25] [26]

that are rigid enough to transmit vibrations but still allow for penetration to happen. Based on AE is also the Grain Impact Analyser and Dust Accumulator (GIADA) on board the Rosetta spacecraft by ESA built for detecting and measuring the number, mass, momentum and velocity distribution of dust particles coming from the comet 67P/Churyumov-Gerasimenko [28]. The detector consists in a square metal plate with 5 sensors, that allow for the identification of the impact location [29]. Coupled with another detector on the same spacecraft that gives a first estimate of the particle size and location when entering the instrument, it is possible to find the particle's speed. From calibration curves it is possible to find the particle's momentum which, when combined with information on the size, gives information on the density of the particle.

2.2.2. Passive Detectors

Passive detectors allow for the characterisation of the space dust and debris environment they were exposed to once they are retrieved from space. Although the retrieval allows for analysis using advanced instruments in laboratories around the world, only the time-integrated flux of impacts can be known: any seasonal variation won't be known. A number of passive detectors have been flown over the years, some of the most important ones will be described in this section.

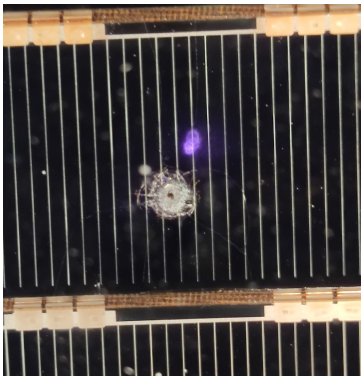

Figure 2.6: Impact damage on the solar array of the Hubble Space Telescope.

Long Duration Exposure Facility (LDEF)

The LDEF was a facility developed by NASA placed in orbit by the space shuttle Challenger in April 1984 and retrieved by the space shuttle Columbia in January 1990 in order to study the effect of exposure to the space environment on materials, systems and spores[30]. In the shape of a 12-sided cylinder, the LDEF [30] contained 57 experiments to test materials, systems, subsystems and technologies in space. Having been in orbit for 6 years, it provided valuable data on the debris and natural small bodies environment in LEO.

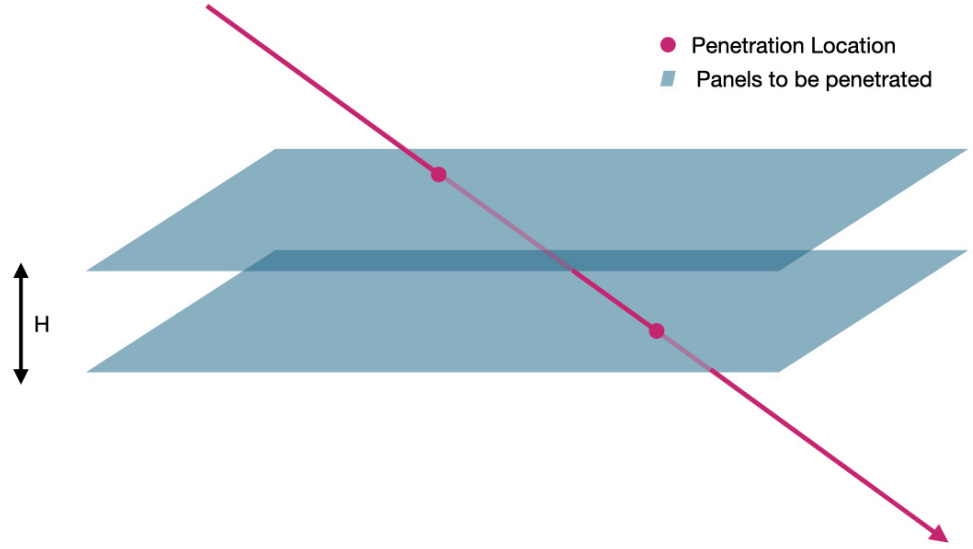

Figure 2.5: Diagram illustrating the working principle of a penetration based detector.

The Hubble Space Telescope solar arrays

The Hubble Space Telescope in 1993 underwent a solar array servicing mission: one of the arrays burned up in the atmosphere during reentry while the other was retrieved on board the Space Shuttle to be analysed. The solar panel, designed and built by ESA is now located at ESTEC, where Figure 2.6 was taken.

2.3. Space Debris and meteoroid Population Models

Given the impossibility of having live tracking of all the objects, natural and artificial, of any size and shape orbiting our planet population models were developed to help scientists and engineers working on space missions. The models are useful for:

- assessing the risk of debris strike during a given trajectory, when planning a new mission
- evaluating the impact of new measures and policies on the evolution of space debris around the Earth
- understanding the physical phenomena impacting the evolution of the debris and meteorite population

Different models exist for different applications, with two of the most used being maintained by NASA and ESA. The models are based on scientific models describing the evolution of the debris and meteorite due to natural variations of gravity, Sun radiation pressur and more. One such model has been developed by Grün[31]. The models are most of the time data driven: what this means is that the output of the model must match observations. Inputs for the model come both from ground based observations and in-situ detection. Ground based telescopes and radars give the majority of the data points, although observations are limited to low altitude and big objects. In-situ detectors are rare and as a result data on small debris and debris in higher orbits is scarce. This means that the output of these models for small debris is usually the result of extrapolation, making the models less trustworthy [32]. The two most used tools are MASTER by ESA and ORDEM by NASA. The two models differ in the reference epoch they use and in the underlying population evolution model they are based on. The input data used is very similar, mostly for small debris where the amount of data is very scarce. Table 2.1 shows the main. differences of the two models

PARAMETER	ORDEM	MASTER
Analysis time period	2010 - 2035	1957 - 2060
Orbital regime	LEO to GEO	LEO to GEO
Debris size	>$10\mu m$	>$1\mu m$
Reference Epoch	Jan 1 2010	May 1 2009
Data Sources	STS returned surfaces	LDEF, EuReCa, HST
	Radar	Radar
	Telescope	Telescope
	Ground tests	Ground tests

Table 2.1: Comparison of the MASTER and ORDEM population models [33].

The two models give very similar results in terms of debris flux for the altitude range and size range for which real data is available. Outside of these ranges the results are heavily dependant on the theoretical models describing the populations and results tend to diverge [33] [34] [35].

2.4. Impact Detection on Space Structures

Structural Health Monitoring (SHM) is an engineering discipline focused on observing the state of structures in order to detect loss of performance, structural stability. Monitoring implies that the evolution of the state over time is known, giving interested parties more information to work with. SHM is use a lot in civil engineering applications and in later years efforts in the aerospace industry have been made [36][37]. Considering the cost and complexity of aerospace systems, having a structural health monitoring system in place can help to identify potential sources of failure before they happen, saving thus time and money during maintenance.

When it comes to space structures, Dr. William Prosser managed a number of projects within NASA on non-destructive solutions for SHM[38]. The focus of the research carried out consisted in finding the location of the impact and possibly the extent of the damage based on acoustic emissions from the impact loaction.

Research on detection of impact started already in 1987 [39] with experiments focused on detecting impact location on the ISS. The experiments by Lempriere were performed at different speeds in order to have both penetrative shots and non-penetrative shots. The presence of both extensional and flexural waves (described in section 2.5) was observed. An impact location algorithm based on a least-squares approach was developed with impact location and time being the unknowns. The speed of the wave was considered known, despite the dispersive nature of Lamb waves. The location of the impact could be identified with an error of 75 mm. The waveforms were furthere analysed with Fourier analysis. One limitation of the study is the need of having a vibration sensor at the point of impact (on the other side of the plate) that is used for for calculating the speed of the wave. In a real-life scenario it is impossible to have a sensor exactly where an impact happens making this method hard to use on a real satellite. Improvements were made in 1999 when the need of a sensor at the location of impact was dropped. The solution proposed by NASA [40]. Once again the co-presence of the extensional and flexural mode was observed (section 2.5). With increased velocity, and thus deformation of the plate, the extensional mode amplitude increased until it generated a voltage comparable to that of the flexural mode. When penetration occurred, only the extensional mode was observed.

Research has been ongoing in the past two decades on impact location identification using accelerometers or piezo-sensors. Most of the research has been on algorithms [41] [42] including methods relying on neural networks[43]. Research on a complete detection system or on the hardware needed for detection is more limited. The research led by Spencer at ESA [44] looked into a complete debris detection system based on piezoelectric sensor. Other groups investigated the use of a piezoelectric film instead of an array of sensors.

2.5. Vibration of Plates

Vibrations in solids are a complex phenomenon that has been studied for more than a hundred years, by physicists and mathematicians such as Horace Lamb and sir Rayleigh [45].

Given the complexity of the phenomenon and the vastness of literature regarding vibrations in solids, this section will focus on the vibrations of plate-like structures. These structures only exhibit extensional

and flexural modes of vibration.
The equations of motion of the extensional mode for a plate structure (i.e. wavelength is bigger than the thickness) can be written as [46]:

$$\frac{\partial^2 u^0}{\partial x^2} + \frac{1-\nu}{2}\frac{\partial^2 u^0}{\partial y^2} + (1+\nu)\frac{\partial^2 v^0}{\partial x \partial y} = \frac{\rho}{A}\frac{\partial^2 u^0}{\partial t^2} \tag{2.2}$$

and

$$\frac{\partial^2 v^0}{\partial y^2} + \frac{1-\nu}{2}\frac{\partial^2 v^0}{\partial x^2} + (1+\nu)\frac{\partial^2 u^0}{\partial x \partial y} = \frac{\rho}{A}\frac{\partial^2 v^0}{\partial t^2} \tag{2.3}$$

x and y are the coordinates in the plane of the plate, u and v the displacement in these directions, ρ the density of the material, ν Poisson's ration and A is given by:

$$A = \frac{Eh}{1-\nu^2} \tag{2.4}$$

with E being Young's modulus and h the plate thickness. The equations describe the motion of the mid-plane of the plate, hence the superscript 0. The speed of the extensional waves is given by [46]:

$$c_e = \sqrt{\frac{E}{\rho}(1-\nu^2)} \tag{2.5}$$

When it comes to the flexural mode, the motion is governed by the following equation:

$$D\nabla^4 w + \rho\frac{\partial^2 w}{\partial t^2} = 0 \tag{2.6}$$

With w being the displacement along the z axis (orthogonal to the plate and the x-y plane). D is the so-called bending stiffness:

$$D = \frac{Eh^3}{12(1-\nu^2)} \tag{2.7}$$

This vibration mode exhibits frequency dispersion, i.e. waves of different frequency travel at different speed. The speed is given by:

$$c_f = \sqrt[4]{\frac{D}{\rho h}}\sqrt{f} \tag{2.8}$$

Where f is the frequency considered. The equations written so far separate the in-plane from the out-of-plane motion of the plate. This is an approximation as the extensional mode results in some out-of-plane displacement and vice versa.
The characteristics of the waves depend, as the equations show, on the material properties and geometry. An open-source calculator has been made available by Deutsches Zentrum für Luft-und-Raumfahrt (DLR), the German aerospace centre. The Matlab-based software can be used to calculate dispersion curves (frequency-velocity curves) for different materials and conditions (in vacuum, fluid...) [47].

3

knowledge gap and research questions

After the literature review of chapter 2 the current knowledge gap can be analysed. The current knowledge about the space debris and micrometeoroid environment is quite limited, especially when it comes to small objects in high-altitude orbits. The only way to acquire information on this class of debris and micrometeoroid is with in-situ detection. Considering the importance that debris population models have in planning current and future space missions and their reliance on debris and meteoroid data, the need to gather more information on the environment around our planet is clear. Current detectors suffer a number of limitations:

- small detection area: given Equation 2.1 describing the debris flux, having a bigger detection area leads to a higher number of objects detected.
- Minimum impact velocity needed: many of the the detectors currently in orbit require impact ionisation to happen, making any object impacting with a velocity lower than 1.3 km/s invisible to the detector

One way to solve both of these issues consists in using the satellite structure as a detection surface. Impact-induced vibrations can be picked up by vibration sensors and used to characterise the debris or micrometeoroid that impacted. Thus the main question of the thesis:

Can the vibrations generated by a micrometeoroid or space debris impact in the structure of a spacecraft be used to derive information on the impactor?

The idea of using acoustic emissions to identify debris or meteoroid strikes is not new, but it has been mostly used in the area of structural health monitoring of space structures. Using vibrations to obtain information on the impactor has been investigated [44] but information could only be obtained when additional instruments were used, instead of relying only on the analysis of the waveform and the arrival time of the vibrational signal. In particular for GEO orbits, the altitude of the orbit prevents ground based observation of objects smaller than 1 meter making this a part of the near Earth environment interesting for research. A lot of the debris in this orbit is the result of raising manoeuvres, seperation events or solid rocket engine firings. All of these debris is thus in a similar orbit to that of the detectors, leading to relative speeds that can be in the order of tens of meters per second. This is why it was decided to focus the research on low velocity impacts (which is also the range of speeds that current ionisation based detectors lack). The research question above can be broken down in a set of smaller questions that the thesis will try to answer:

- What does the waveform of impact-generated vibrations look like?
- Which sensors should be used to pick up vibrations in a spacecraft?
- How can impacts on a spacecraft be simulated in a laboratory environment?
- Which data processing techniques can be used to extract data from the sensor signal
- Which information on the impactor can be obtained from the waveforms?

- Are there better suited materials or locations for such an application?
- Can the impact location be estimated?

3.1. Research strategy

In order to answer the research questions described above a research plan was developed. Two main activities were performed: one one hand simulating impacts in a laboratory environment and collecting vibrational data, on the other hand developing analysis tools and algorithms to extract information from the vibration signal. The general objective of the experiments was to obtain vibrational data with sensors in different location, different plate and projectile materials, different impact locations and impact speeds.

The first step in the research consisted in getting accustomed with the lab, the setup and the data acquisition system. The accelerator wasn't used for many years, with the help of scientists and engineers from the TMS section of ESTEC it was cleaned and the worn down components replaced. Once the accelerator was operational the old target mount was used to perform some test shots to assess the performance of the accelerator after many years of warehouse storage. The settings of the data acquisition system were tuned during this phase. The preliminary data was used to design the new target plate (subsection 4.1.3) that would be used later on in the research.

Once the target plate had been designed and built by the workshop of ESTEC, the experiments could begin. Two plates were available: a 3 mm thick aluminium plate and a 5 mm thick aluminium skin and aluminium honeycomb panel. Given the proposed area of application of the detection technology (satellites in GEO), the honeycomb structure was deemed more representative of the materials used on those types of satellites. It was thus decided to perform impacts on the aluminium plate first. This would allow to use the aluminium plate to test sensor location, sensor and plate mechanical coupling, data processing techniques and testing strategies and use the lessons learned on the more expensive honeycomb structure. What this means is that most of the experiments that were used to draw conclusions about the debris and micrometeoroid detection method were performed on honeycomb as all that was learned during test on aluminium could be used to generate the highest quality data, with quality indicating absence of noise, ease of processing, and relevance for the research question that is being answered. Nonetheless the many experiments performed on aluminium are an important source of information that, if not used to draw conclusions, was still used as a term of comparison for the results of impacts on honeycomb.

At a later stage in the research a solar panel was available for testing. Impacts were performed and the data analysed, adding thus valuable information as solar panels are on almost any satellite and have usually a big area, making them an interesting location for the application of the detection technology being investigated in this thesis.

4

Methodology

In this chapter the tools and strategies used during the research will be described. As the research is experimental in nature, both the laboratory instruments used will be introduced and the data processing techniques used to extract data from the raw signals obtained from the sensors. Experiments for this research were carried out within the ”Materials and Electrical Components” laboratory at ESTEC, from the TEC-QEE department.

4.1. Experimental setup

The setup can be broken down into its main components:

- Accelerator
- Target plate
- Sensors
- Data acquisition system
- Projectiles

Each of these will be described in this chapter.

4.1.1. Accelerator

The accelerator is used to accelerate spheres up to 3mm in diameter to speeds below 200 m/s in order to simulate low velocity impacts. Development of the accelerator began in 1983 at TU Munich in support of the ESA Rosetta mission [48] [49]. The accelerator was used to simulate cometary dust impacts on the solar arrays of the spacecraft.
Two main sections of the accelerator can be identified: one for storing energy and the other for releasing it and accelerating particles. The two parts (together with the target plate) are shown in Figure 4.1.

The acceleration is based on electromagnetic induction. Once the capacitor is discharged a high intensity current through the coil generates a time-varying electromagnetic field[1]. In the flyer plate, sitting on the coil, eddy currents are generated that oppose the change in flux of the EM field. This results in a repulsive force between the main magnetic field and the induced one that leads to the acceleration of the flyer plate. The projectile that is chosen for the impact test has to be placed on the flyer plate: a small dent is made in the centre of the plate for then projectile to sit in to make sure the projectile is aligned with the setup. As the plate is being accelerated and not the projectile itself, both electrically conductive and non-conductive projectiles can be used for tests. After travelling a distance of 2 cm, the flyer plates hits a so-called ”stopper plate” that prevents the flyer plate from continuing its trajectory. The stopper plate has a hole in its centre allowing thus only the projectile to continue flying until it hits the target.
The capacitor(C = 10μF) can be charged up to 15 kV, with higher voltages requiring more charging time. Higher voltages result in higher energy delivered by the coil, leading to higher speeds, as shown

[1]The accelerator can be seen as an RLC circuit so despite not having AC current the intensity still varies with tiem

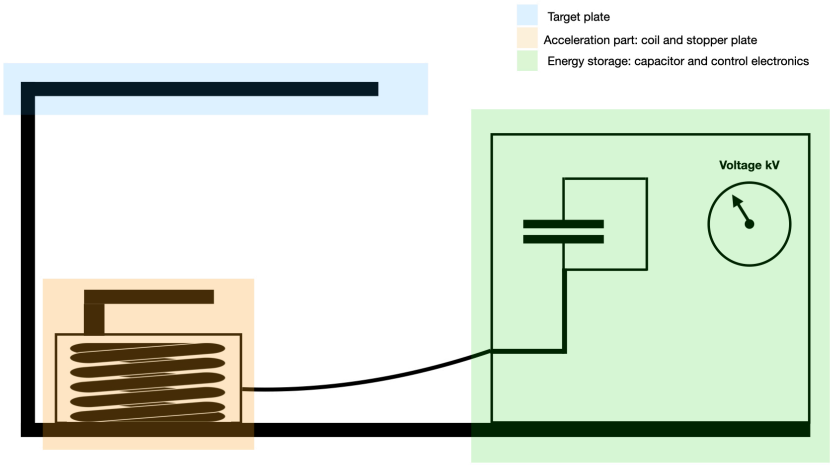

Figure 4.1: Diagram of the experimental setup. The control and energy storage section, accelerating coil and target plate are shown and marked with different colours.

in Figure 4.2. The capacitor is connected to the coil via a mercury switch that, thanks to no moving parts, is an effective way of opening and closing the high voltage section of the circuit.

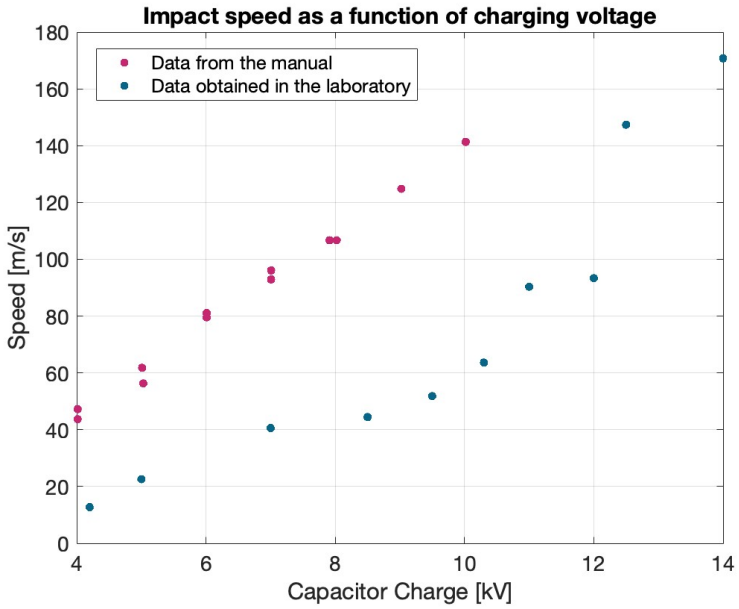

Figure 4.2: Impact speed of the projectiles as a function of charging voltage of the capacitor bank. The data obtained in compared to the values of the manual [48]. Target material: aluminium plate. Projectile material: glass.

4.1.2. Flyer plate

The flyer plate is an aluminium disk that sits on top of the coil and is used to accelerate the projectiles. The use of a metal plate allows for the acceleration of both metallic and non-metallic projectile. During development and testing of the accelerator, different flyer plates were used with a variety of sizes and composition. The acceleration of the plate is proportional to the ratio of the electric conductivity of the material and its density [49]. The force acting on the accelerator is proportional to the current in the flyer plate which, in turn, is proportional to the electrical conductivity of the material, as seen in Equation 4.1.

$$F \sim I_2 \sim \sigma \tag{4.1}$$

The mass of the plate is in turn proportional to its density. It can be concluded thus that the acceleration is proportional to the ratio of electrical conductivity to density of the material of the plate, as clear from Equation 4.2.

$$a = \frac{F}{m} \sim \frac{\sigma}{\rho} \tag{4.2}$$

Table 4.1 shows this ratio for a set of materials[49]. Magnesium and aluminium have the highest ratio, due to the lower cost and higher availability of aluminium it was selected over magnesium.

Material	Mg	Al	Be	Cu	Ag	Au	Brass	V	Pb
$\sigma/\rho\ [Am^2V^{-1}kg^{-1}]$	14740	13900	12900	6300	5950	2300	1400	1400	424

Table 4.1: Ratio of electric conductivity and density for a set of materials. [49]

On one hand, increasing the plate's diameter increases the energy transfer from the EM field to the plate, on the other it increases the mass of the plate (and thus its inertia): these two effects work against each other. The optimal plate was found to be 3 cm in diameter and 0.5 mm in thickness [49]. Figure 4.3 shows a flyer plate after acceleration. The deformation due to the inertia of the spherical projectile is clearly visible. For materials with a high density (e.g. stainless steel) accelerated to very high speeds this can lead to the plate being perforated. Figure 4.4 shows the deformation of flyer plates that were accelerated in increasingly strong EM fields.

Figure 4.3: Flyer plate after acceleration: side view. The deformation due to the inertia of the projectile is clearly visible.

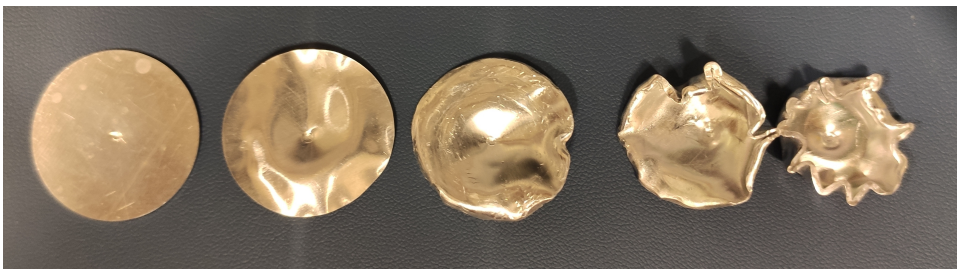

Figure 4.4: Flyer plates after being accelerated with increasing capacitor charge. The left most plate has not been accelerated.

4.1.3. Target plate

The target plate serves the main purpose of simulating the side panel of a spacecraft, specifically in relation to its vibration characteristics. The original target was of cantilever type. Figure 4.5 shows a diagram of what the setup looked like. An optical bench mounting was used to fix the target plate of interest at a distance of 20 to 30 centimetres from the coil. This setup was deemed not appropriate

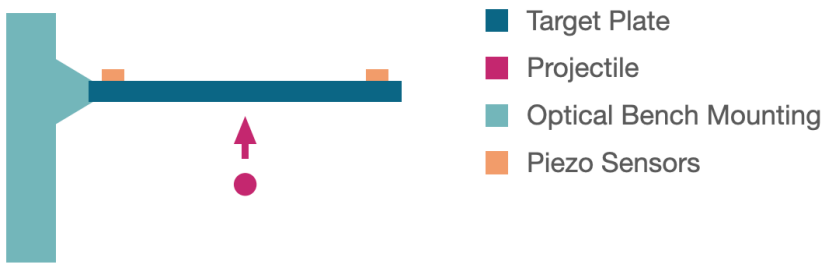

Figure 4.5: Diagram of the original setup for the target plate [48].

as it would introduce vibrational modes typical of cantilever structures. To avoid this, a new target has been designed and built. For the new target, after discussion and feedback from ESA and TU Delft researchers, the following requirements were considered:

- the plate should be fixed on all 4 sides to replicate a real side-panel of a satellite fixed to the structure and remove modes of vibration typical of structures with free boundaries
- it should be possible to (easily) replace the plate to allow for the user to independently change the plate material
- the support structure should not impact the vibrations of the plate in a significant way
- it should be possible to change the impact location of the projectile
- the structure should enclose the coil for safety of the operator while still allowing ease of loading of the projectiles
- the protection elements should allow for inspection of the setup and use of high speed cameras during testing
- the plate should be as big as possible given the available size in the laboratory

A table-like structure was designed, with the top plate being the one that is impacted. This part can be easily replaced to test impacts on different materials. A square plate with a side of 60 cm was chosen to be the target as this was the maximum size that would fit in the space available in the lab. Having a plate that is as big as possible allows to minimise the boundary effects of the plate.

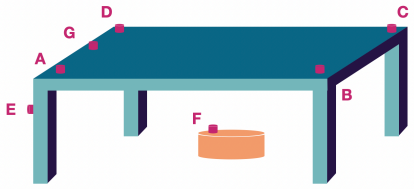

Figure 4.6: Location of the sensors on the structure

Two materials were chosen for the plate: aluminium and aluminium skin sandwich panel. The aluminium plate[2], due to its lower cost, was used to test the setup and perform impacts to tune the settings of the accelerator, data acquisition system and data processing. The aluminium sandwich panel was used at a later stage in the research as it is a material used on actual spacecraft: this results in vibration data that is closer to what a real spacecraft would experience.
To check the influence of the supporting structure on the behaviour of the plate, a sensor was placed on the support legs of the plate to compare its signal with that of the sensors on the plate. Impact tests were performed and it was observed that the the vibrations on the structures are 10-20 times lower in

[2]Although aluminium is rarely used in panel form as the structure of a satellite, manned spacecraft are sometimes equipped with a Whipple shield as protection from impacts, on the ISS it is made of aluminium. As a consequence the experiments on aluminium still bear relevance for real life applications [50] [51].

amplitude than on the plate. This reduction in amplitude was deemed sufficient to consider the plate and the structure independent.
For the experiments with the solar panel, the support structure was not big enough and an alternative solution had to be found. Given the size of the solar panel, a rectangle with sides exceeding one meter, it was decided that hanging it from a movable structure present in the lab would be the best solution. This allows for the solar panel to be moved over the accelerator to change the point of impact. Raising and lowering of the solar panel is also possible, allowing the operator to inspect impact damage and insert a new projectile in the accelerator for further testing.

4.1.4. Sensors and data acquisition

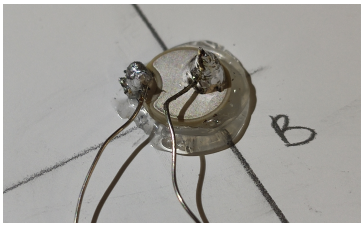

Figure 4.7: Closeup of one of the sensors used mounted on the target plate.

For the detection of vibration piezo-sensors were chosen, thanks to their availability, low cost and ease of use. Specifically, piezoelectric disks from Physik Instrumente (PI) GmbH were used. Table 4.2 shows the main characteristics of the sensors used. 7 sensors were used, 5 on the target plate, one on the support structure and one on the stopper plate, as shown in Figure 4.6 with the names that will be used throughout the report to indicate the sensor. The sensors where linked to a coaxial cable with a Bayonet Neill–Concelman (BNC) connector to allow for transfer of the signal to the data acquisition system being used. The sensors were then attached to the target plate with a heat activated adhesive. A closeup of the sensor is given in Figure 4.7.
A Picoscope model 6000 was used as data acquisition system. This model allows for up to 8 input channels and a sampling frequency of up to 20 MHz. The acquisition rate is high enough to capture the Nyquist frequency calculated from the resonant frequency of the sensors (given in Table 4.2).

Diameter [mm]	6,9
Thickness [mm]	1
Electrode Material	Ag
Resonant Frequency - diameter [kHz]	300
Resonant Frequency - transversal [MHz]	1-2

Table 4.2: Properties of the sensors used.

4.1.5. Projectiles

As analogue space debris and micrometeoroids a set of beads of different size and materials were used. Table 4.3 shows the main characteristics of the projectiles.

Material	Mean Mass [g]	Diameter [mm]
Glass	0.039	3
Teflon	0.033	2.9
Steel	0.1	3

Table 4.3: Projectiles used during the experiments. The material, mass, size is given, in addition to the manufacturer.

4.2. Data Processing techniques

In this section the tools and methods used to process the data will be described. To make it easier for the reader to understand the choices made in terms of methods the typical characteristics of the signal picked up by the piezo-sensors will be described.

4.2.1. Description of the signal

The signal picked up by the piezo- sensors depends on the location of the sensor w.r.t. the impact location, the impact speed, mass and material of the projectile and many other factors. Despite all the variability, the signal has some general characteristics that are shared among all the experiments performed during the thesis research. In this section those features will be listed and described to make it easier for the reader to understand the hurdles faced when working with the data, the decisions

made during the thesis and in general to give a better view on the work done. Figure 4.8 shows the raw signal (voltage vs time) picked up by sensor A during experiment 30. The first feature in the signal

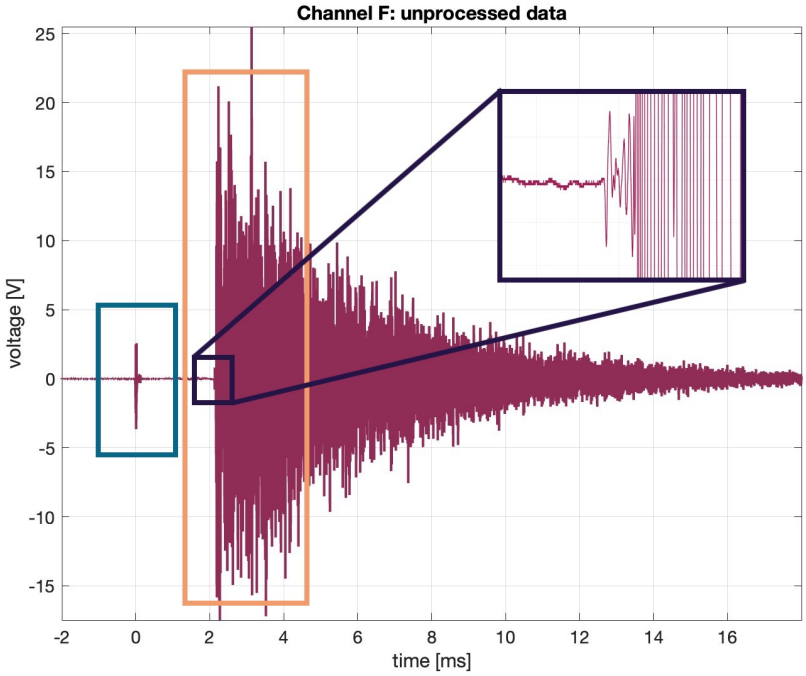

Figure 4.8: Raw data picked up by sensor A during experiment 33. A part of the signal has been magnified to show its features. Target plate: aluminium. Projectile material: steel.

has been highlighted with the light blue square. This is the result of the discharge of the capacitor and the strong electromagnetic field generated by the coil. At first it was believed that this small amplitude signal was the result of vibrational waves travelling from the stopper plate to the sensors due to the impact of the flyer plate. An experiment without accelerating any plate was performed: thus only the capacitor was discharged. This triggered the acquisition system and generated a signal with the same feature highlighted in light blue, as Figure 4.9 shows. The second feature of interest in the signal has been framed in dark blue in Figure 4.9. These small amplitude and high frequency oscillations are the extensional waves generated during the impact [38]. These waves travel at higher speeds than Lamb waves [46], hence why the appear at the start of the signal. Depending on the experiment conditions (plate material, projectile material and impact speed mainly) the magnitude of these waves can increase or decrease. In general the bigger deformation of the target plate, the bigger the amplitude of the extensional mode [38].
The last feature of the signal is framed in orange in Figure 4.9. These high amplitude vibrations are due to the Lamb waves described in section 2.5. As Lamb waves exhibit frequency dispersion due to the speed of the wave being proportional to the square root of the frequency Equation 2.8, the frequency content of this part of the signal changes over time. This can bee seen in Figure 4.10 that only shows the first part of the high amplitude part of the signal in Figure 4.8.

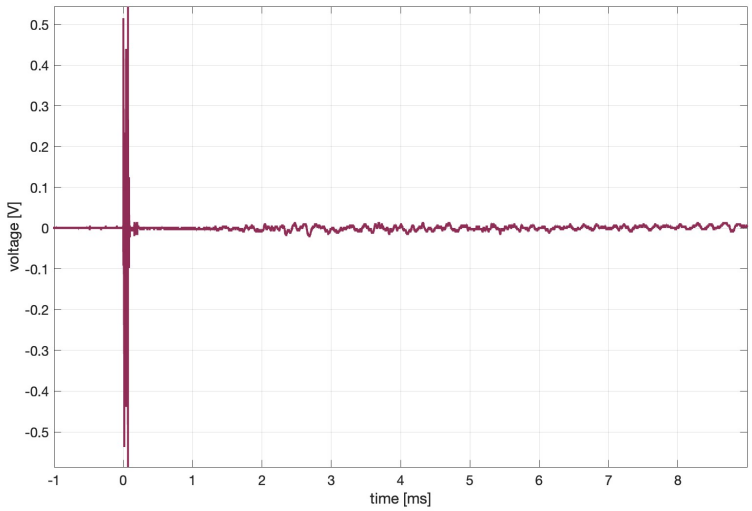

Figure 4.9: Raw data picked up by sensor A during experiment 87. Target plate: sandwich panel. Projectile material: none (blank shot).

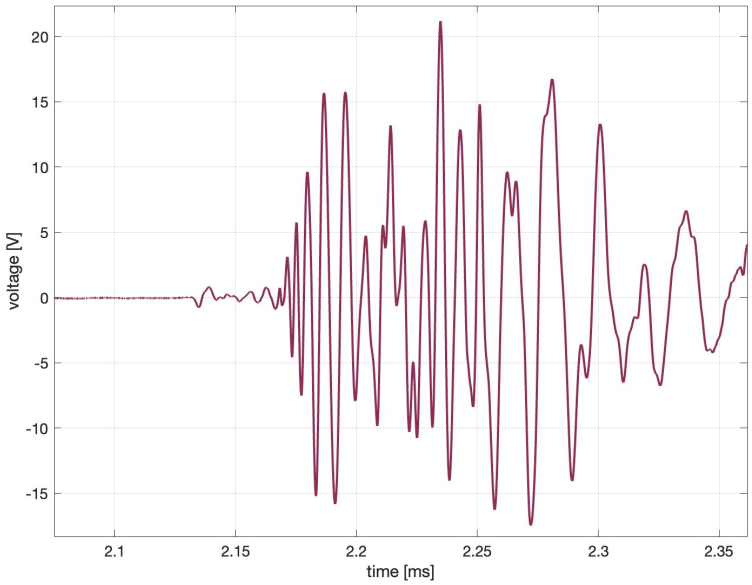

Figure 4.10: Raw data picked up by sensor A during experiment 33. Zoomed in version of Figure 4.8.

Each of the sensors placed on the target plate registers a time-varying signal. Although the signal depends on the target material, impactor material, mass, speed and impact location some similarities across all the waveforms acquired can be noted this is why the same data processing techniques can be used on all the signals.

4.2.2. Wavelet Trasform

Given the time-varying nature of the signal, a tool such as the Fourier transform is not suitable to analyse the data. Although a Fourier analysis is able to identify the frequencies of a signal it fails to capture the change over time of the frequency content a wavelet transform was deemed more suitable in the given context.
The first formal description and use of wavelets was in France, thanks to the “French school” lead by J.

Morlet, A. Grossmann and Y. Meyer [52]. Initially developed for analysis of seismic data, the success of the tool lead the group of mathematicians to better develop the mathematical background of the wavelet transform.
A wavelet is a function that is local both in time and the frequency domain. A function is said to be local when most of its energy is in a finite interval. A simple sine wave is local in the frequency domain (it has a given frequency) but not in the time domain (it extends over the whole time domain). A Dirac-delta is the opposite: local in time but not in frequency. A wavelet sits somewhere in between these two extremes [52]. This property of wavelets makes them interesting to decompose a signal both in time and frequency, something that a Fourier transform can't do.
Different types of wavelets exist, suitable for different applications. Once a wavelet is chosen for the problem at hand, it is referred to as mother wavelet. The transform consists in convoluting the wavelet with the original signal. This is done by sliding the wavelet over the time domain and at every time-step scaling it in the frequency domain too. The result of this is, for every time-step of the signal, a decomposition showing the frequency content of that signal at that time.
Matlab offers a continuous wavelet transform implementation via a tool-box. Table 4.4 lists the parameters and settings used for the wavelet transform in Matlab.

Parameter	Value - type
Wavelet	"Bump"
Bandpass filter	1 to 250 kHz
Voices per Octave	32

Table 4.4: Parameters used in the Matlab implementation of the continuos wavelet transform

The output of the transform is a $n \cdot m$ matrix with n being the number of frequency bins (related to the voices per octave parameter) and m being the number of time steps in the signal (i.e. the product of the sampling frequency and the duration of the acquisition window). Each cell contains a complex value that has information on the amplitude and phase of the wavelet. Plotting the absolute value of this matrix generates a so called scalogram. A scalogram is a plot with time on the x-axis and frequency on the y-axis that shows the evolution of the frequency content over time. Figure 4.11 shows what the scalogram looks like.

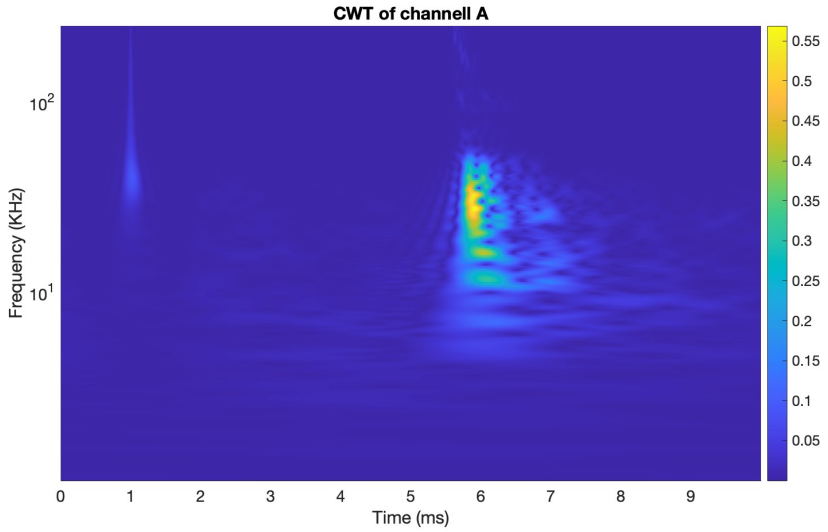

Figure 4.11: Continuous wavelet transform of the signal of sensor A during experiment 102.

4.2.3. Further processing with the wavelet transform

4.2.4. Total vibrational energy

Once the matrix with the complex coefficients of the wavelet transform has been obtained, it can be further processed. If the absolute value of each value in the matrix is taken, the real number obtained

gives information on the amplitude of the specific wavelet, eliminating the phase shift. Summing the values in each column outputs a vector that contains, for every time-step, the sum of all the wavelet amplitudes. Figure 4.12 shows what such a plot looks like. Figure 4.11.

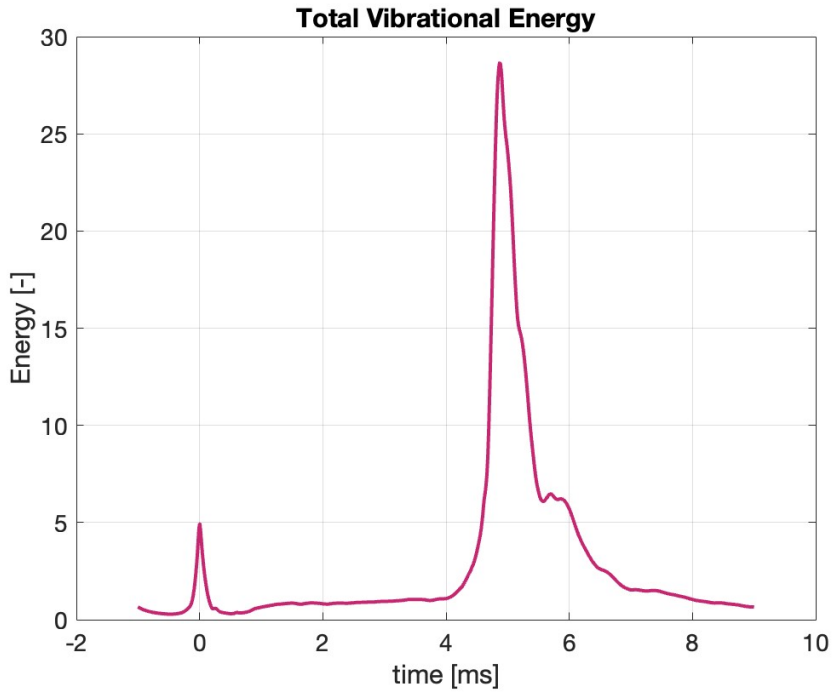

Figure 4.12: Continuous wavelet transform of the signal of sensor A during experiment 102.

It is expected that increasing the impact speed of the projectile would lead to higher voltage generated by the sensors. It was speculated that the vibration modes being excited upon impact, i.e. the combination of frequencies and respective amplitudes depend on the speed of impact, the size and material of the projectile and the impact location on the plate. If the total energy transferred from the projectile to the plate in the form of vibrational energy is the same , then the energy of the signal should also stay constant. The energy per unit time (so for every time-step given the discrete nature of the problem at hand) can be found by simply squaring every value in the matrix outputted by the wavelet transform and performing a column-wise summation. Why this is the case is explained in subsection 4.2.5.

4.2.5. Frequency distribution

Taking inspiration from what was done to obtain the total energy, the cells of the matrix can also be summed horizontally. The result of this operation is the sum of all the amplitudes that a wavelet of a given frequency takes over time.
This sum was done from the time at which the maximum energy is reached and until the total energy (as seen in Figure 4.12) reaches 20% of the maximum. This way signals of different length and amplitude can be compared. The result of the sum per rows is then divided by the total energy for every frequency and every time step in order to obtain a normalised version of the data that makes it easier to compare different experiments. Figure 4.13 shows what such a plot looks like, once again done for experiment 102.

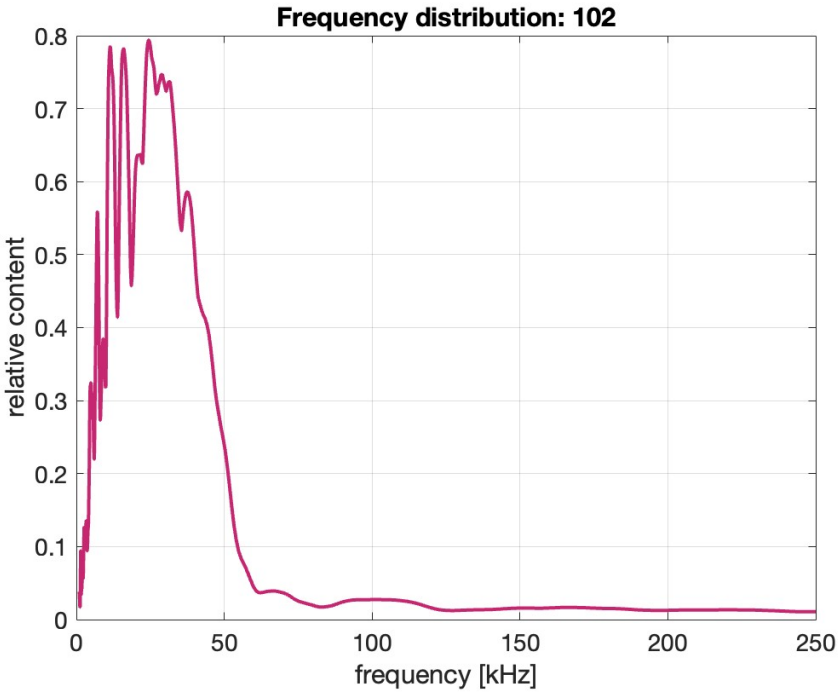

Figure 4.13: Frequency distribution for the experiment 102.

Despite the plots generated by processing the data in this way giving insight into the main frequencies of the acquired signal, they do not bear any direct physical meaning. This is why it was decided to consider the energy of the signal, as defined in Equation 4.3, for a time-varying signal $x(t)$.

$$E = \int_{t_0}^{t_f} x(t)^2 dt \tag{4.3}$$

The signal acquired is a discrete signal, this means that the energy of the signal (sampled at a constant frequency f) is given by Equation 4.4, where $\Delta t = f^{-1}$. This definition gives the total energy of a sampled signal but it can be adapted to obtain the distribution of energy as a function of the frequency of the signal, Equation 4.5. E_{f_k} refers to the total energy of the wavelets of frequency f_k of the wavelet decomposition of the signal (with $k = 1...N_f$, where N_f is the number of frequency bins of the decomposition). $A_{k,i}$ is the amplitude of the mother wavelet scaled to frequency f_k at i-th time step of the signal, which is obtained by taking the norm of the complex value in the k-th row and i-th cell of the matrix output of the wavelet transform.

$$E = \sum_{i=1}^{n} x_n^2 \cdot \Delta t = (t_f - t_0) \sum_{i=1}^{n} x_i^2 \tag{4.4}$$

$$E_{f_k} = (t_f - t_0) \sum_{i=1}^{n} A_{k,i}^2 \tag{4.5}$$

In order to compare different experiments the total energy per frequency of the wavelet decomposition was divided by the overall total energy, giving thus a normalised result (Equation 4.6). Equation 4.6 shows that for a signal sampled at a constant frequency the normalised energy for a given frequency can be simply obtained by summing all the squared values of a single row of the matrix generated via the wavelet transform of the signal, an then dividing that number by the sum of the all the values of all the cells in the matrix.

$$\overline{E}_{f_k} = \frac{E f_k}{\sum_{k=1}^{N_k} E_{f_k}} = \frac{(t_f - t_0) \sum_{i=1}^{n} A_{k,i}^2}{\sum_{k=1}^{N_f} (t_f - t_0) \sum_{i=1}^{n} A_{k,i}^2} = \frac{\sum_{i=1}^{n} A_{k,i}^2}{\sum_{k=1}^{N_f} \sum_{i=1}^{n} A_{k,i}^2} \tag{4.6}$$

4.3. Calibration and verification of the measurements

Given the objective of characterising debris and micrometeoroids based on the acoustic emissions upon impact, all the features of the laboratory simulated impact must be known. For the size and mass of the projectiles the data of the manufacturer was confirmed with the use of a scale and caliber. The impact speed was obtained from the signal of two piezo-sensors: one on the stopper plate and the other on the target plate. The dynamical model used to determine the speed of the projectile was verified with the use of a high speed camera. For the actual data acquisition (sensors and data acquisition system) the calibration of the manufacturer was considered as both the sensors and the data acquisition system were bought for this research.

5

Measuring the Impact Speed of the Projectiles

One of the parameters of interest when it comes to debris and micrometeoroids is their speed and the detection method under investigation and development should be able to estimate the speed/momentum/kinetic energy of the projectiles. This is why it is important to determine with precision the impact speed of the projectiles.

5.1. Speed measurements

In order to measure the speed of the particles a simple time-of-flight strategy was used, as already done with the same accelerator by the research group that developed it [49]. A sensor placed on the stopper plate is used to detect when the projectile leaves the acceleration section of the device (t_0). Another sensor, on the target plate, is used to detect when the projectile impacts the plate(t_f). Using Equation 5.1 it is possible to estimate the speed knowing the distance of the stopper plate to the target plate (Δh in the equation).

$$v = \frac{\Delta h}{t_f - t_0} \tag{5.1}$$

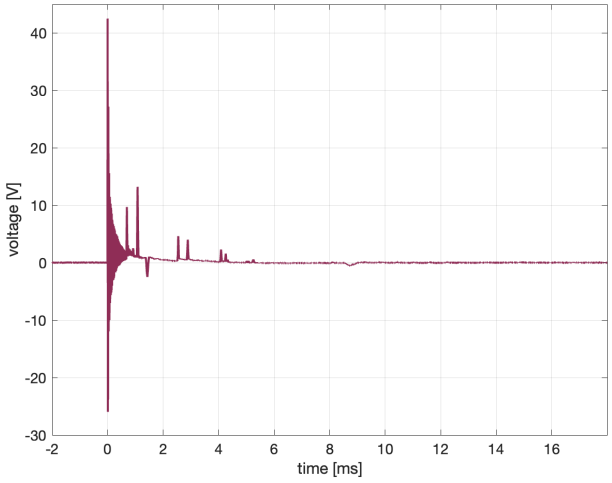

Figure 5.1: Raw data from the sensor on the stopper plate of the accelerator.

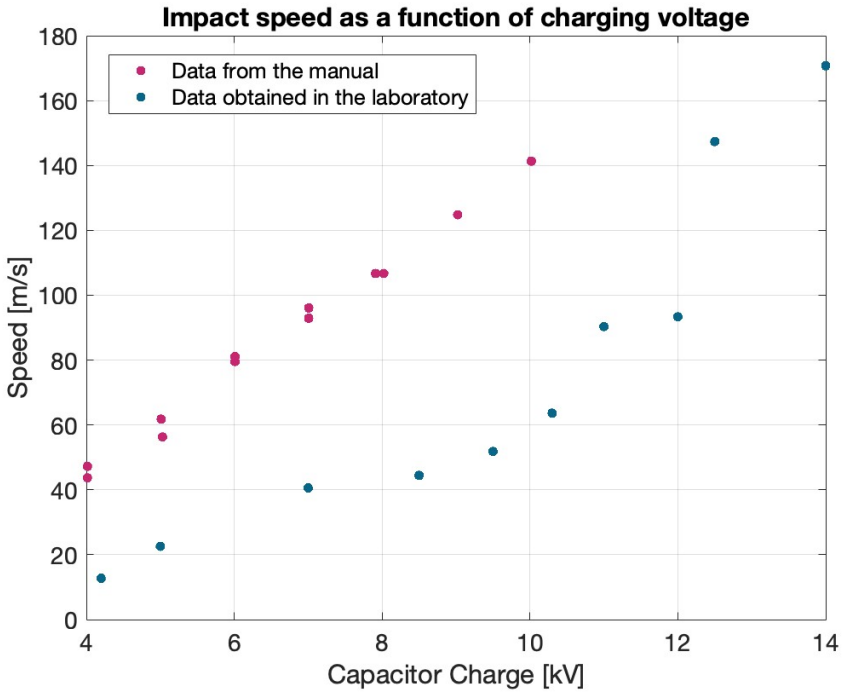

Figure 5.2: Comparison of the speed achieved with the accelerator when it was developed and when it was used for the MSc thesis research.

Figure 5.3 shows what a typical signal from the piezo-sensor on the stopper plate looks like. This sensor is used to trigger the acquisition of data with the Picoscope, this is why the start of the signal is at exactly 0 s. After the first peak some other peaks can be seen, these are probably due to the flyer plate bouncing inside the acceleration cavity. With respect to the second sensor used for speed measurement, Figure 5.3 shows how such a signal looks like. At 0 ms it is possible to see a strong signal: this was at first assumed to be due to the flyer plate impacting the stopper plate and the vibrations travelling in the setup but it was later discovered to be due to the strong electromagnetic field generated by the coil. At around 7 ms it is possible to see high-amplitude vibrations: these are the vibrations on the target due to the impact.

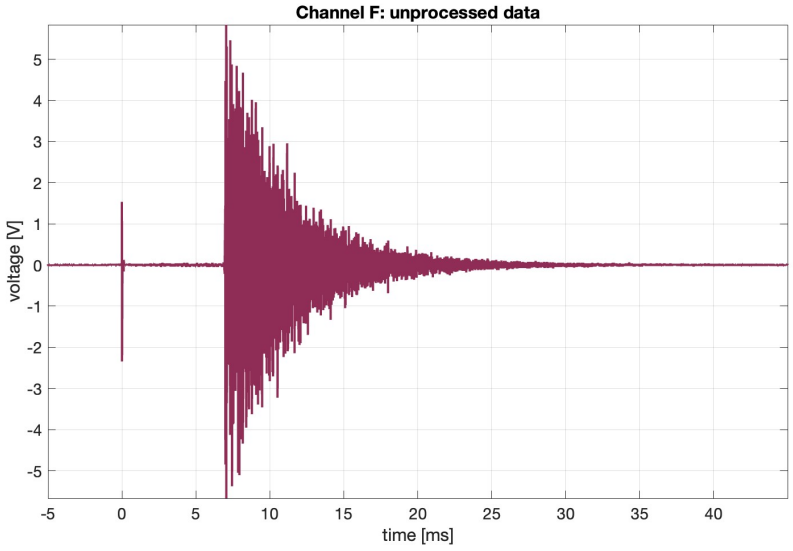

Figure 5.3: Raw data from one of the sensor on the aluminium stopper plate

Using glass projectiles and an aluminium target, a number of shots at different charging voltage were performed. These shots were then used to calculate the speed of impact and compare it with the speed given in the manual. Figure 5.2 shows the impact speeds obtained and how they compare with the calibration curves in the manual. Although the two sets of data follow a similar trend, there is a noticeable difference between the two. Possible reasons for this difference are due to loss of performance of the accelerator and compensation for travel time of the vibrations in the metal. The second option was ruled out as even including corrections keeps the two sets of data quite separate.
Despite the difference, speeds of almost 200 m/s were reached meaning that loss of performance was only present at lower voltages. As for every experiment performed during the thesis, the speed was measured, knowing the relation between voltage and speed serves only the purpose of helping choose the charging voltage.

5.1.1. Verification of results with a high speed camera

Due to the strong electromagnetic fields generated in the coil, it is possible that a voltage is picked up by the data acquisition system without any actual vibration of the sensor. This could lead to errors in the speed measurement. To make sure that the speed obtained with the method described so far is correct, it was decided to use a high speed camera to check the results.
Two strategies can be used to measure the speed of an object using a high speed camera, for every impact performed during the verification test, if possible, both methods were used. Before any method was used the camera was calibrated: this was achieved by placing a custom ruler where the camera focus distance was set to. Knowing the distance between two points on that ruler allows to convert from number of pixels on the image to real life lengths.

If the frame rate of the camera is high enough, an object will occupy the camera's field of view for more than a single frame. Calling k the number of frames that capture the moving object, it is possible to calculate the distance travelled in those k frames via the camera software (thanks to calibration). The frame rate allows to find out the time elapsed between the first and the k-th frame, allowing to find the speed as a simple distance over time calculation.

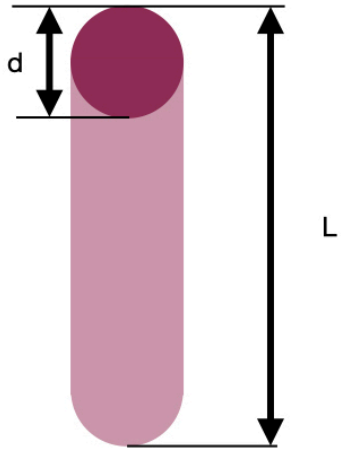

Figure 5.4: Diagram showing the measurement needed to find out the speed of a projectile from a single frame of a video.

At higher projectile speeds it can happen that the the projectile is only captured in one frame: this makes the method described so far unusable. Every frame is taken with a shutter speed Δt_s, during this time, the projectile travels a distance Δs: this results in the spherical projectile not appearing as a circle but having an elongated shape of length L. This length is due to the diameter of the projectile (d) and the distance travelled. The speed of the projectile can then be found as $c = (L - d)/\Delta t_s$.
Figure 5.5 shows, for a set of 5 experiments, the speed estimated using the piezo-sensors and the two methods with the high speed camera. Using the piezo-sensors underestimates the speed when compared to thw camera. The two methods based on high speed imagery produce very similar results. The difference with respect to method 1 is on average 32% and with respect to method 2 it is 33%.

5.1.2. Comparison of speed measurements

Figure 5.5 shows that the speed measured by the camera is always higher than what is picked up by the piezos. Some hypothesis were made to try and explain the observed difference.

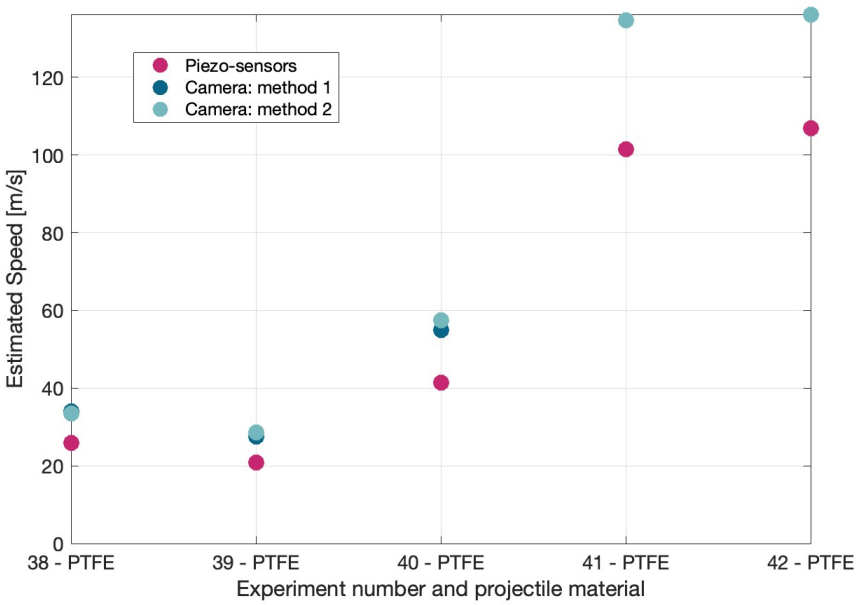

Figure 5.5: Estimated speed of the projectile based on data from the piezo-sensors and from the high-speed camera

- travel time of the vibrations from the impact point on the target plate to the sensor;
- parallax error between the camera's focal plane and the trajectory of the projectile;
- average speed calculation: the camera captures a very small part of the initial trajectory while piezos are used over the whole trajectory. Deceleration due to drag and gravity can play a role in the mismatch.

Figure 5.6 shows how the piezo-sensor is fixed on the stopper plate. The distance from the centre of the plate (measured from the centre of the hole) to the sensor is less than 10 cm. Considering the speed of sound in aluminium to be higher than 3000 m/s, the time delay that this would cause is of a couple of percent points of the time used for the calculations.

During the experiments it sometimes happened that when the capacitor stopped charging, the data acquisition system got triggered. It was then speculated that the discharge of the energy into the coil could also trigger the system: this would mean that the measurements start before the flyer plate even hits the stopper plate. To test the hypothesis a blank shot was performed. The flyer plate was not used so the test consisted in simply discharging the stored energy of the capacitor in the coil. Figure 5.7 shows the signal generated by sensor F[1]. The results were surprising as, first of all, registration of the data was triggered despite the data acquisition settings being the same as for normal experiments. The other surprising thing is the very close similarity with data from the same shot during any other experiment, like shown in Figure 5.8.

What this shows is that it is not the flyer plate hitting the stopper plate that triggers data recording but the electromagnetic field. This means that when data is recorded, the projectile is not yet moving and the total distance is travelled during data recording is longer than what was considered earlier as not it includes the part of the trajectory under the stopper plate. As a result, the distance of the sensor from the impact location has no effect on the speed measurement.

If the total travel distance is measured from the top of the coil instead of the stopper plate the difference between the speed measured with the camera and with sensor data is reduced to 14%. Despite the improvement it was deemed necessary to improve even more the accuracy.

While experiments for the thesis were performed, some support was given to the researchers that would use the accelerator setup in the upcoming years. This consisted in taking high speed footage of materials for space use and their interaction with lunar regolith. During one of these shots it was

[1] Sensor F, is used to start the data recording in every experiment as it is the first one to measure any signal.

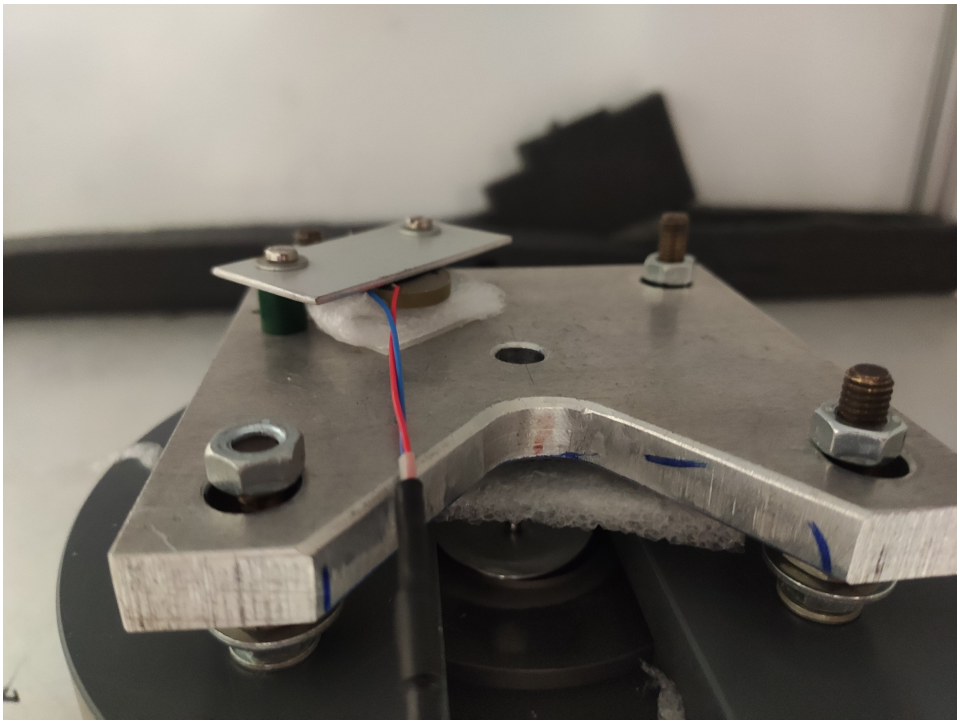

Figure 5.6: Close up picture of the coil of the accelerator and the stopper plate. The piezo-sensor is also clearly visible.

observed that the regolith (replacing the projectile of the previous experiments) would separate from the flyer plate before impacting the target plate.

Additional footage was taken of the flyer to observe whether this was happening during other experiments and it was observed that indeed, before the plate would reach the stopper plate, the projectile was already separated. The explanation for this was thought to be due to air drag: the plate has a much higher area to mass ratio as compared to the projectile, leading to higher deceleration due to drag. Further inspection of the footage showed that the flyer plate would bend to become concave during acceleration and then, when EM acceleration stopped, elastic forces internal to the plate would bring it back to its original shape: this spring like behaviour would accelerate even more the projectile. What the footage also implies, is that the acceleration of the plate is very short and maximum speed is reached well before impacting the stopper plate. Lastly, another reason for the mismatch of speed between camera and sensors is due to camera capturing images at the start of the trajectory while the sensors measure the average speed over the whole trajectory.

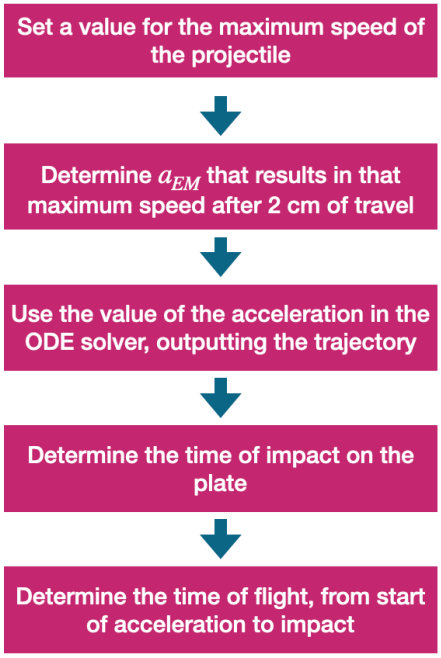

Figure 5.9: Algorithm used to determine the acceleration of the particles and the time of flight, from start of the acceleration to impact.

It was thus decided to model more accurately the trajectory of the projectile by taking into account everything that was listed so far: short acceleration, start of the data recording due to induction and effect of drag and gravity on the trajectory. From the camera footage it was observed that

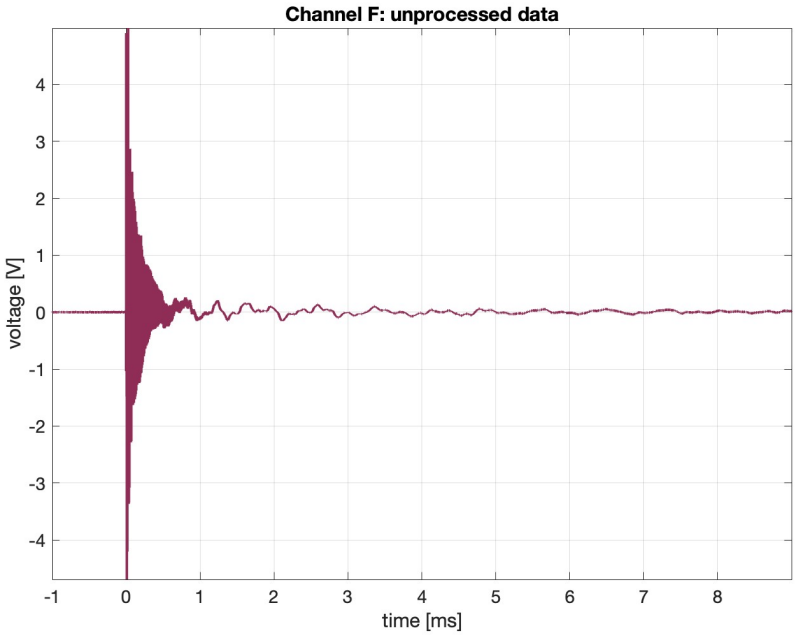

Figure 5.7: Data picked up by the piezo-sensor F (on the stopper plate) during a blank shot).

Parameter	ρ_{air} kg/m^3	g $[m/s^2]$	Projectile Diameter [mm]	Projectile Mass [mg]	C_d
Value	1.225	9.81	3	40	0.5

Table 5.1: Parameters used to model the trajectory of the projectile

the separation of the projectile from the flyer plate happens
after 2 centimetres, thus the projectile is accelerating only in those 2 centimetres. The acceleration of the projectile was modelled as a triangle wave as that was deemed as the most representative of the electromagnetic field variations. Deceleration due to air resistance and gravity were added to the model, using the values in Table 5.1 for the parameters. The table include the air density ρ_{air}, the gravity acceleration g, the diameter and mass of the projectile, and the drag coefficient of a sphere. Figure 5.9 shows how all these parameters were used to determine the time of flight of the particle, which is what can be determined from the piezo-sensors on the stopper plate of the accelerator and the target plate. Looping the algorithm for a set of maximum speeds achieved by the projectile outputs, for each value, the corresponding time of flight and speed when impact happens. This allows to determine in a table-look-up manner the impact speed from the time-of-flight calculated from the sensor measurements.

The following differential equation was set up:

$$\ddot{y}(t) = -g - \frac{1}{2}\rho\dot{y}^2(t)\frac{S}{m}C_d - a_{EM} \tag{5.2}$$

Where y is the vertical position of the projectile over time, S is the cross section of the projectile , C_d is the drag coefficient of a sphere, m is the mass of the projectile , g is the gravity acceleration of the Earth and a_{EM} is the acceleration due to the electromagnetic field. This latter term increases linearly until the maximum acceleration is reached at $y = 1.5cm$ and then decreases again linearly until $a_{EM} = 0$ when $y = 2cm$. The differential equation was solved using the ODE45 solver on Matlab, with initial speed and vertical position set to 0.
Figure 5.10 shows the speed as measured with piezo-sensor data and the high speed camera footage. ”Piezo method 1” refers to the initial method used, i.e. considering the average speed from the stopper plate to the target plate. ”Piezo method 2” accounts for the fact that the initial trigger signal is given when the projectile is still stationary, and thus the total travel distance was increased to include the part from the coil to the stopper plate. ”Piezo method 3” considers the simplified dynamical model

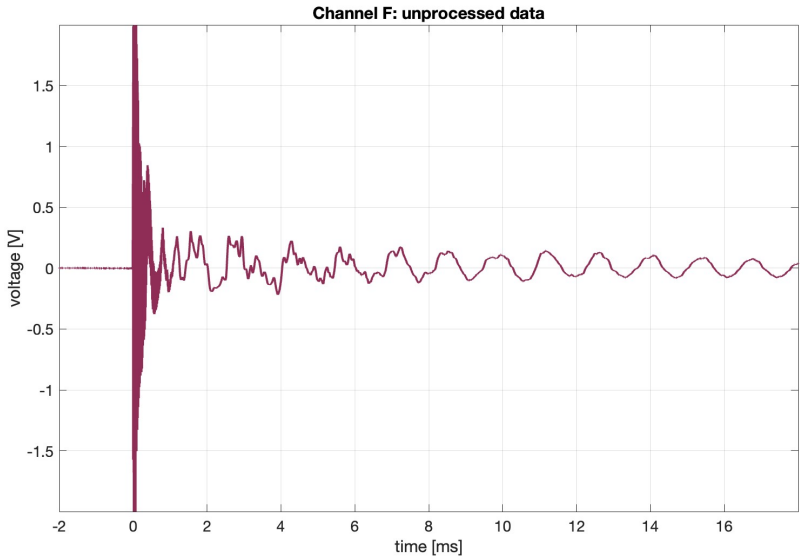

Figure 5.8: Data picked up by the piezo-sensor F (on the stopper plate) during experiment 88.

described previously accounting for air drag and acceleration of the particle. The figure clearly shows how accounting for the acceleration phase and the deceleration due to drag and gravity leads to the speed estimated from sensor data to approach the speed measured from the high speed footage. What has been plotted is the final impact velocity as a function of the time of flight as determined from the signal acquired by the piezo-sensors.

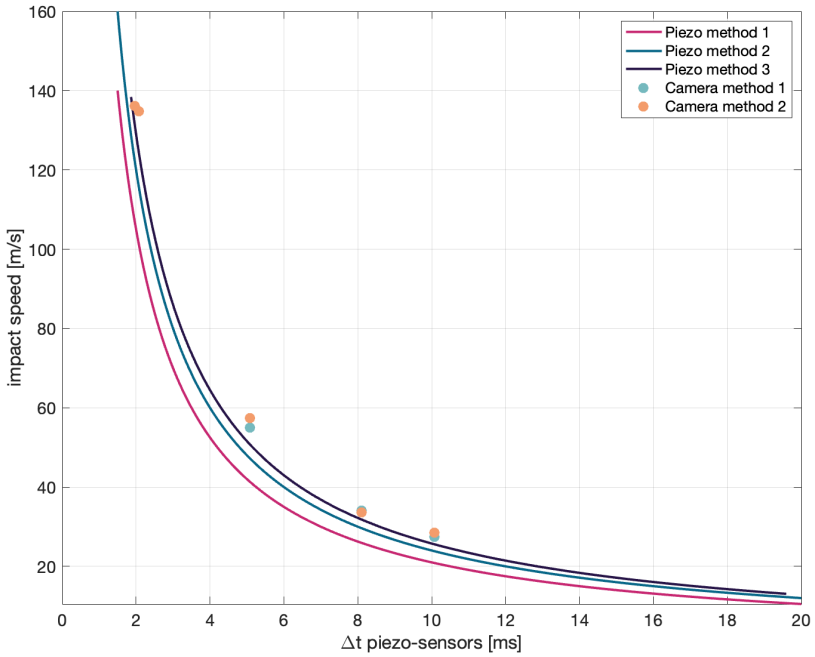

Figure 5.10: Speed of the projectile as measured using data from the piezo-sensors and the high speed camera.

6

Impact location estimation

Being able to identify the impact location of a piece of debris or a micrometeorite can be useful for a number of reasons. From assessing potential damage to the satellite to derive the material impacted for further processing of the data[1].

6.1. Description of the algorithm

Looking at literature, a number of localisation algorithms have been developed. From analytical solutions [53] to least squares algorithms [41] and neural networks [43]. These methods try to estimate the coordinates (x, y) of impact on the plate and the time of impact. The assumption of known speed of sound is made for these methods.
The main idea behind all of the algorithms is that the time of arrival of the vibrations to a sensor depends on the distance to the impact point, so having at least three sensors allows for the implementation of a triangulation algorithm.
The algorithm that was developed is a least-squares algorithm due to the success of such an algorithm shown in literature. Instead of only estimating the impact time and location, the wave speed was also estimated. This was inspired by algorithms used in satellite based navigation. When estimating the location of a GPS receiver on Earth, it can be beneficial to estimate, in addition to the coordinates of the receiver, the speed of light. The second reason to estimate the wave speed is due to the peculiar shape of the waveforms detected, as described in **??**. For every sensor, the arrival time of the wave must be found. There are many ways in which this can be accomplished, from setting a voltage threshold to the first peak in amplitude above the average noise. As long as the time of arrival of the wave is consistently derived for all the sensors in the setup, a successful impact location identification can be performed. Given an impact time of the debris on the target, using two different thresholds or methods for extracting the arrival time from the waveform would lead to two different travel times, and, as a result two different wave speeds. This is another reason why estimating the speed of sound was considered beneficial: what is being estimated is not the real speed of sound but an ”artificial” speed that depends on how the waves are timed.
The algorithm will now be described using the following symbols:

- (x_i, y_i) are the coordinates of the i-th sensor
- t_i is the time of arrival of the vibration at the i-th sensor
- c is the speed of sound
- t_0 is the impact time
- (x, y) is the impact location

Given the number of unknowns (impact coordinates, time and wave speed) the number k of sensors used must be greater than 4. The observations, Y, are given by the times t_i, which is the time of arrival

[1] The waveform generated on impact depends, among other things, on the material being impacted. This is why knowing which part of the satellite got hit, and thus which material got hit, can be useful

at the i-th sensor:

$$Y = \begin{bmatrix} t_1 \\ t_2 \\ \vdots \\ t_k \end{bmatrix} \tag{6.1}$$

While the unknowns X are:

$$X = \begin{bmatrix} x \\ y \\ t_0 \\ c \end{bmatrix} \tag{6.2}$$

The time t_i as a function of the unkwowns is given by:

$$t_i = t_0 + \frac{\sqrt{(x - x_i)^2 + (y - y_i)^2}}{c} \tag{6.3}$$

In order to construct the observation matrix A of a least square method, Equation 6.3 should be derived with respect to vector X.

$$\frac{\partial t_i}{\partial x} = -\frac{x - x_i}{c\sqrt{(x - x_i)^2 + (y - y_i)^2}} \tag{6.4}$$

$$\frac{\partial t_i}{\partial y} = -\frac{y - y_i}{c\sqrt{(x - x_i)^2 + (y - y_i)^2}} \tag{6.5}$$

$$\frac{\partial t_i}{\partial t_0} = 1 \tag{6.6}$$

$$\frac{\partial t_i}{\partial c} = -\frac{\sqrt{(x - x_i)^2 + (y - y_i)^2}}{c^2} \tag{6.7}$$

The observation matrix is then:

$$A = \begin{bmatrix} \frac{\partial t_1}{\partial x} & \frac{\partial t_1}{\partial y} & \frac{\partial t_1}{\partial t_0} & \frac{\partial t_1}{\partial c} \\ \frac{\partial t_2}{\partial x} & \frac{\partial t_2}{\partial y} & \frac{\partial t_2}{\partial t_0} & \frac{\partial t_2}{\partial c} \\ \vdots & \vdots & \vdots & \vdots \\ \frac{\partial t_k}{\partial x} & \frac{\partial t_k}{\partial y} & \frac{\partial t_k}{\partial t_0} & \frac{\partial t_k}{\partial c} \end{bmatrix} \tag{6.8}$$

Now that all the elements needed in the algorithm have been introduced they can be used in the algorithm as shown in the diagram in Figure 6.1. The initial guess for the algorithm uses the centre of the plate for the first two unknowns, the time of arrival of the vibrations to the first sensor and the typical speed of sound in the solid being investigated. In case more than 4 sensors are available the data of only 4 can be used to solve the system of 4 equations. This was tried but was later abandoned as the initial guess being too close to the real solutions led the least-squares algorithm to diverge in many cases.

The stopping criteria is based on the magnitude of the correction ΔX. The algorithm stops when wither the error as defined in Equation 6.9 is below the threshold or when the number of correction reaches 20 iterations.

$$err = \sqrt{x_{est}^2 + y_{est}^2 + t_{est}^2 + \left(\frac{c_{est}}{10^5}\right)^2} < 10^{-15} \tag{6.9}$$

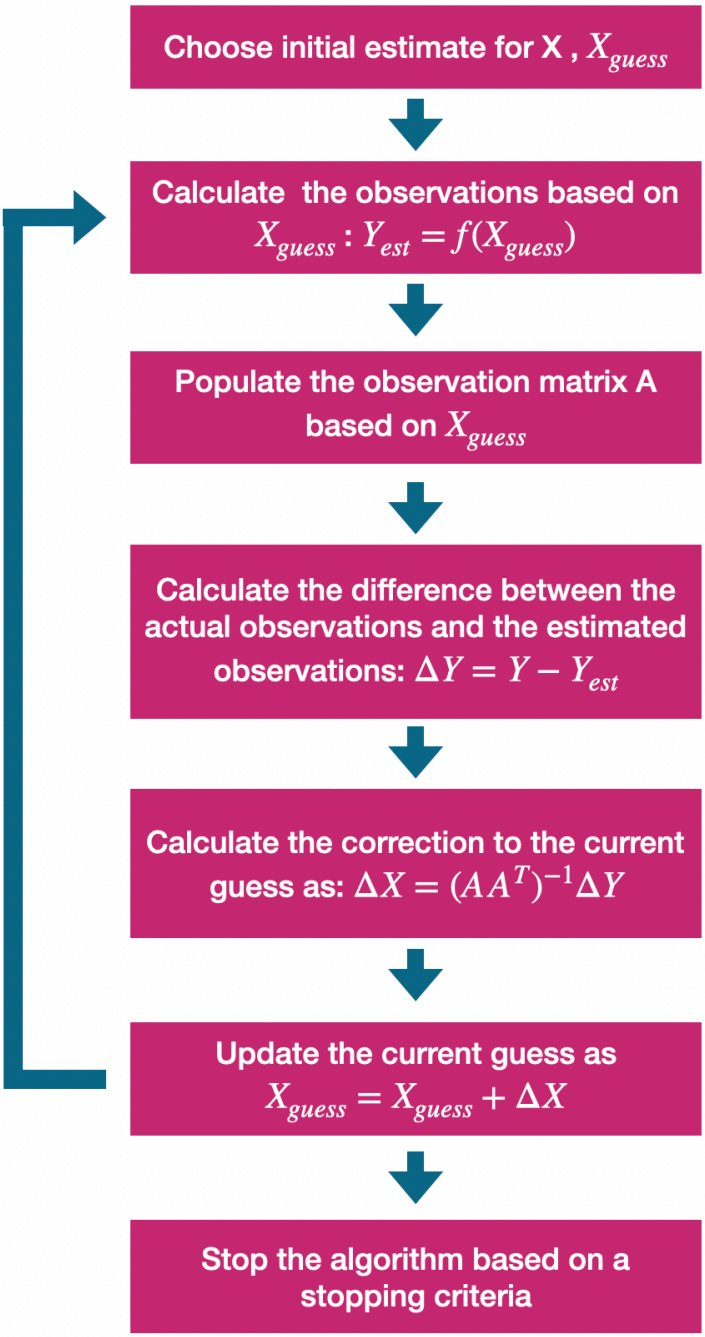

Figure 6.1: Impact detection algorithm

6.2. Determination of the time of arrival of the vibrations

The observations Y in the algorithm described in section 6.1 are the time of arrival of the vibrations. These have to be extracted from a signal that looks like what is shown in Figure 6.2. Although the very high vibration frequency results in a very dense plot, what is being analysed now is only the time of arrival.

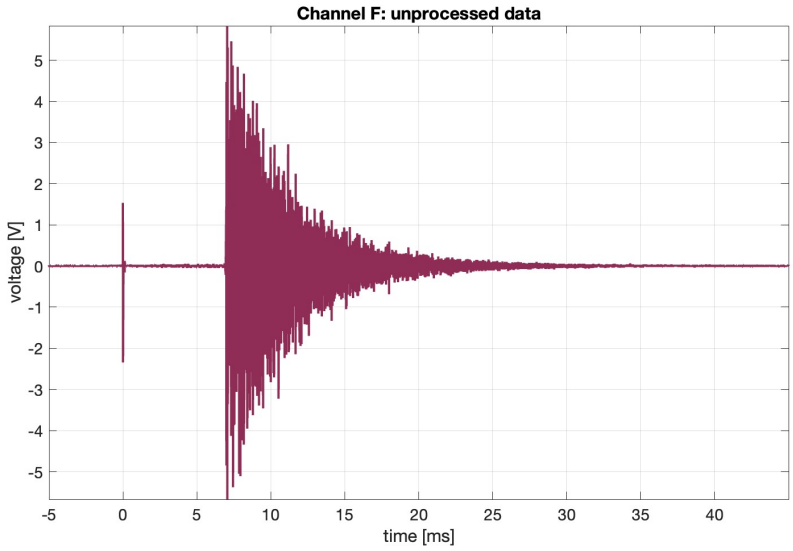

Figure 6.2: Raw data detected by sensor A during experiment 29

Many options exist, like setting a voltage threshold and, when the signal exceeds this level, the time is recorded. Although simple, different impact speeds will require different thresholds. Additionally, there is no clear structure in the data that indicates how to chose the threshold level.
When an impact occurs, both flexural and extensional vibration modes are generated. This happens at any impact speed until penetration happens. A penetrating impact leads to lower amplitudes of the flexural mode (can be as low as at the noise level). This is why it was decided to use the extensional mode to obtain timing information. The extensional mode has a smaller amplitude w.r.t the flexural mode in all the experiments considered. In particular impact on aluminium, given the small deformation of the plate, lead to amplitudes of this mode one or two orders of magnitudes smaller than the flexural mode. In Figure 6.2 the extensional mode can't be seen, the plot has to be enlarged like in Figure 6.3. The extensional mode is the small packet of waves right before high amplitudes oscillations at 7 ms in the plot.

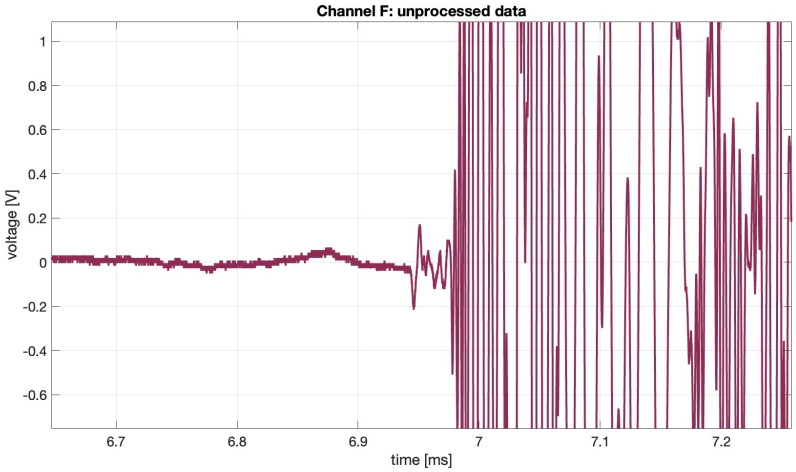

Figure 6.3: Raw data detected by sensor A during experiment 29: focus on the extensional mode

The first idea that was tried consisted analysing when the signal exceeded twice the level of noise. Although this worked well with aluminium panels it couldn't be translated to aluminium sandwich panels. Despite these panels generating extensional vibrations with bigger amplitudes as compared to aluminium, a high level of noise was observed. This was due to sound waves propagating from the

stopper plate after impact of the flyer plate. The effect was partly mitigated by adding a layer of foam to the stopper plate. This can be seen clearly in Figure 6.4 where the level of noise before the arrival of the vibrations is much higher than what was observed in Figure 6.3. The extensional wave can be seen in the subplot on the right, but the idea of using the signal exceeding the noise level as a timing criteria can't be used.

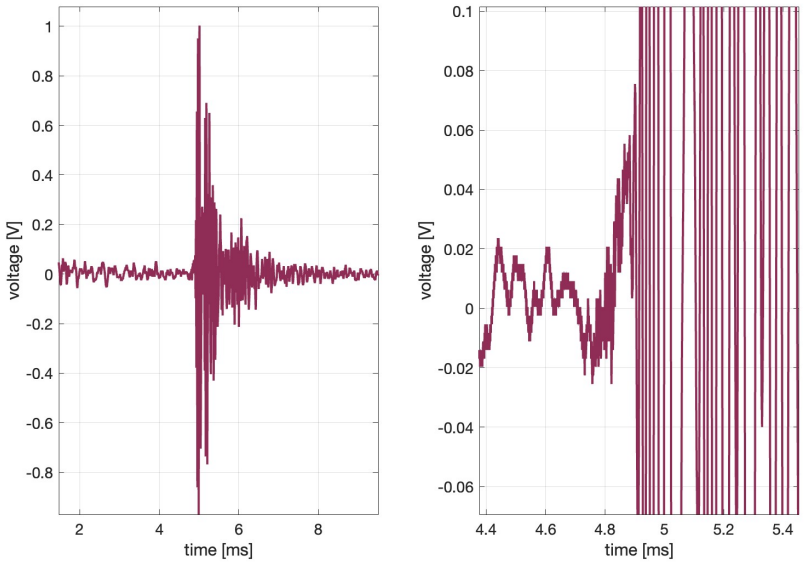

Figure 6.4: Raw data detected by sensor A during experiment 92.

6.3. Sensor Positioning

As the algorithm was designed to estimate 4 parameters, 4 measurements (i.e. 4 sensors) are needed. A way to choose the sensor placement on the 60 by 60 centimetres plate had to be thought of. One one hand, keeping the sensors away from the edges allows to reduce the boundary effects due to reflection and refraction of the vibrations, on the other it reduces the usable space for impact (i.e. the polygon obtained by connecting the sensors). Additionally,having the sensors spread should allow for a more precise determination of the impact location the same way as for GNSS applications (the phenomenon is known as dilution of precision [54]). To help in this problem a code was developed that takes as input the location of the sensors and produces as output the mean error across the plate.
The plate is divided in a number of squares, and an impact is simulated on each corner of the squares. Figure 6.5 shows the grid points used in the code. The simulation consists in calculating the time needed to reach each of the sensors and adding noise to that measurement. The noise is obtained from a random normal distribution with zero mean. Once the noise has been added, the resulting times are used as input in the multilateration algorithm.

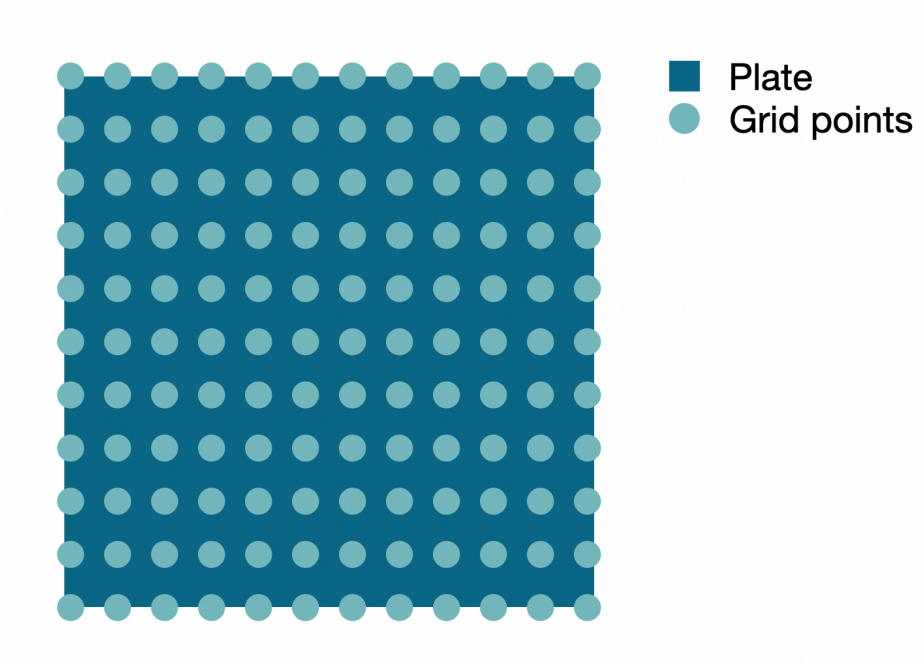

Figure 6.5: Plate and grid points used in the code for the determination of the precision of the location estimation based on the position of the sensors on the plate.

The algorithm can be then used to study how different sensors' layouts perform in terms of precision of the impact estimation process.
It was observed that the area contained in the polygon obtained by connecting the sensors offers higher precision than the area outside of it. This is expected as on the inside of the polygon, the sensors are spread around the location impact, while outside of it all the sensors are on one side of the impact. This is the same as the dilution of precision observed with GNSS.
The code was used to guide the choice for the placement of the sensors, although constraints due to the conditions of the setup were also considered. The final choice consisted in having the sensors at the edges of a square of side 40 centimetres, aligned with the square plate.

6.4. Accuracy of the estimation

Once the location algorithm was developed it was tested using data from impacts. Despite all the impacts being done with data acquisition on, not all of the impacts were used to test the precision of the location estimation algorithm.
When an impact was performed, the impact crater was identified and its coordinates measured with a ruler. This was used as the real impact location to use as a reference to study the precision of the estimate. After an impact coordinates were measured, the crater was marked with a permanent marker to allow the crater of the new experiment to be identified. The results were summarised in a table to make it easier for the reader to see the results.
It was observed that using 5 sensors as opposed to 4 is beneficial to the algorithm, not in terms of accuracy but in terms of convergence. The accuracy with 4 or 5 sensors is comparable, but for shots close to the centre of the plate, in many instances using only 4 sensors didn't allow the algorithm to converge, despite an accurate first guess.

Experiment	x estimated	y estimated [cm]	x true [cm]	y true [cm]
62	26.5	38.2	26	39
76	29.81	29.1	29	30
49	28.63	30.43	29	30

6.5. Estimation of the speed of sound

As previously discussed, it was decided to include the speed of sound in the material as one of the estimated parameters in the algorithm in order to increase the accuracy of the estimation process.

Material	Speed Estimated [m/s]	Speed in Literature [41]
Aluminium	5450	5650
Honeycomb	5040	5010

6.6. Automation of the impact location estimation process

The strategy described so far to identify the impact location, although precise in many circumstances, has the drawback of requiring manual identification of the time of arrival of the extensional mode of the wave. Different options were considered to automate the detection of the arrival of the vibrations, as that is the only missing element to achieve a method that only requires as input the raw data collected from the sensors and can output the location of impact of the projectile.

Many options (and their combinations) were considered, developed and tested but they were discarded due to the inaccuracies in detecting the arrival time of the waves or due to the method not working for all the cases it was tested on. If full automation is to be developed, the method should work with whatever waveform as input.

As the extensional mode has very small amplitude but high frequency, the first approach consisted in simply using a band-pass filter to remove the frequencies outside the characteristic frequencies of the extensional mode. The arrival time was defined as the time when the filtered signal exceeded the noise level by a factor of two. The noise level was obtained by finding the average amplitude of the first part of the signal. In order to filter out every frequency that wasn't part of the extensional mode a narrow-band filter had to be used, this introduced a time-delay (phase distortion) that wasn't constant making it hard to compensate. For this reason, time-estimates were not accurate enough for the algorithm to converge and the method was discarded.

If acoustical noise due to impact of the flyer plate impacting the stopper plate can be limited (as was done by adding a layer of foam to the stopper plate), the extensional mode could be identified by calculating a rolling window average of the signal and detecting when this average exceeds a threshold. The threshold can be taken as double the value of the average in the first 10% of the signal, which is before any acceleration takes place so that only noise is present. This method, reasonably simple and computationally efficient, was discarded because the time of arrival of the waves not always allowed for the algorithm to converge. In particular, for low velocity impacts, the extensional mode was very close in amplitude to the noise level so either the threshold was not reached and lowering it lead to the noise level exceeding the threshold. Increasing the size of the window, despite reducing the effect of locally high values of the noise, also reduced the time resolution of the method.

While researching time-frequency methods for data analysis, the Wigner-Ville transform was found. This method gives as output the same information as a Wavelet transform. The advantage of this method is an increased resolution of the output. This increased resolution could be used to detect at which time the extensional mode arrives, in particular observe the energy content of the frequencies of the extensional mode and detect when it goes above the noise-level (multiplied by a factor). Performing a Wigner-Ville transform of the whole signal is computationally expensive (MATLAB estimated 700 GB of RAM needed), but this is not necessary. Despite the band-pass filter not performing well in terms of time identification it can still be used to select a small time-window in which the extensional mode is contained. The Wigner-Ville transform can then be performed on this small section of the whole signal acquired. This strategy gave good results and is thus a good candidate for an automated method for the detection of the impact location of debris or micrometeoroids. Given the good performance of this method more information will be given. A Butterworth filter was used thanks to its flat response in the band of interest.

```
1
2  fs = Fs;            % Sampling frequency
3 Wp = [10, 300*1e3]/(fs/2); % Pass band frequencies (normalized)
4 Ws = [5, 500*1e3]/(fs/2); % Stop band frequencies
5 Rp = 3;                % Ripple at pass band
6 Rs = 50;               % Ripple at stop band
```

```
7
8  [n, Wn] = buttord(Wp, Ws, Rp, Rs);
9  [z, p, k] = butter(n, Wn, 'bandpass');
10 [sos, g] = zp2sos(z, p, k);
11 Hd = dfilt.df2sos(sos, g);              % Create the filter
```

Once the filter has been created and the raw signal filtered, the time interval on which the Wigner-Villte trasnform should be performed can be identified. Figure 6.6 shows the effect of filtering the data. It can be seen how the amplitude of the extensional mode is greatly reduced after filtering but, at the same time, the noise in the first part of the signal is also greatly reduced. This is the advantage and disadvantage of using such a narrow-band filter. Looking at the peaks of the filtered data and comparing them with the raw signal, the phase distortion of the filter can be observed. The time when the filtered data exceeds a threshold, set by the user, can thus be identified. Using 5 times the average noise gives a time between 2.13 and 2.14 ms in the example in Figure 6.6. Calling this time t_{wv}, the time interval on which the Wagner-Ville trasnform should be performed is $[t_{wv} - 3 \cdot 10^{-5}\text{s}, t_{wv} + 2 \cdot 10^{-5}\text{s}]$. This allows for an interval that is big enough to contain the arrival of the vibrations despite the error introduced by the filtering process, but small enough that the transform is computationally accessible. Looking at Figure 6.6 it could be argued that a threshold to determine the time of arrival of the vibrations could be set directly on the original signal. This is true for many of the experiments but, in the case of experiments with the sandwich panel, oftentimes the noise in the setup had a bigger amplitude than the extensional mode making the use of a threshold not-effective and resulting in the need for more complex processing.

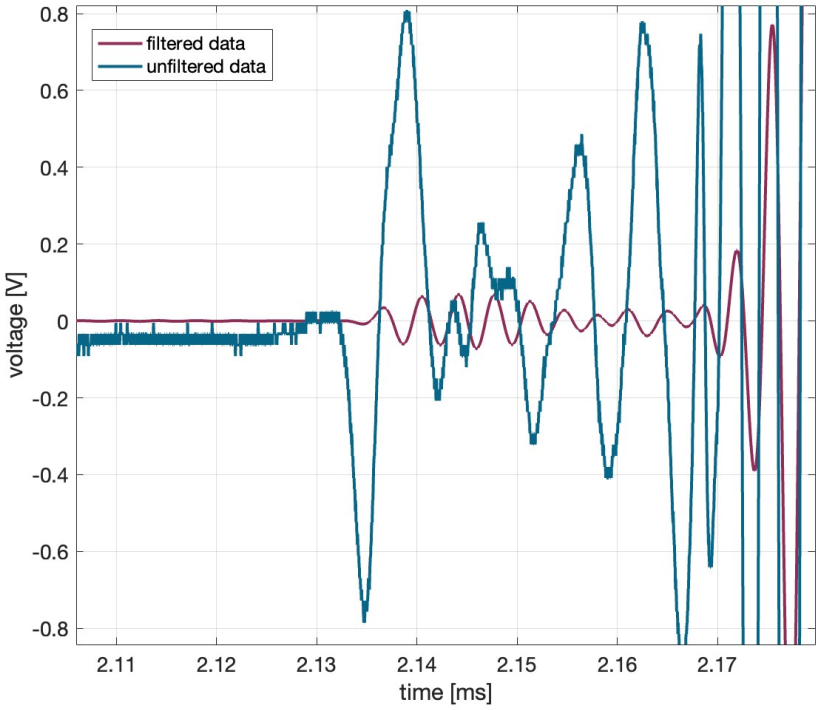

Figure 6.6: Comparison of raw data and data filtered with the Butterword filter described in this section.

Figure 6.7 shows a plot of the Wigner-Ville transform of the part of raw data of channel A during experiment 33. Comparing this with, for example Figure 7.1 shows the increase in resolution of the transform. Between 2.12 and 2.14 ms it is possible to see a dark orange vertical stripe: this shows the arrival of the first vibrations.

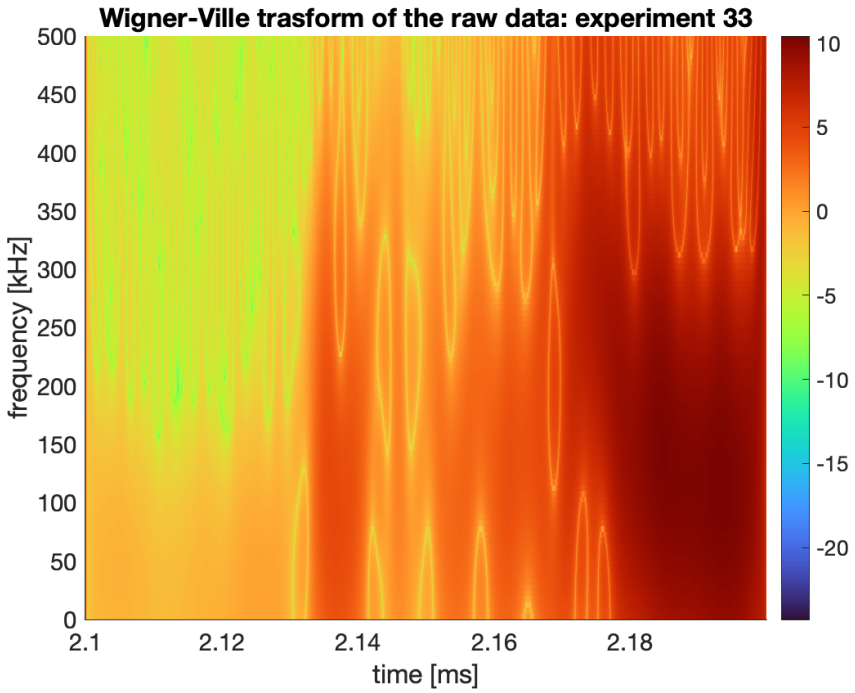

Figure 6.7: Wigner-Ville transform of (a section) of the raw data acquired during experiment 33.

With the matrix output of the Wagner-Ville transform it is possible to plot the energy per unit time contained in the signal, by performing a column-wise addition of the squared value of each cell of the matrix[2]. This gives the total energy per unit time but the algorithm was observed to perform better if only frequencies from 100 kHz to 200 kHz are considered. A threshold can then be set, as Figure 6.8 shows, based on the energy content in the first part of the signal. The time at which the energy level crosses the threshold can be used as the time of arrival of the extensional mode.

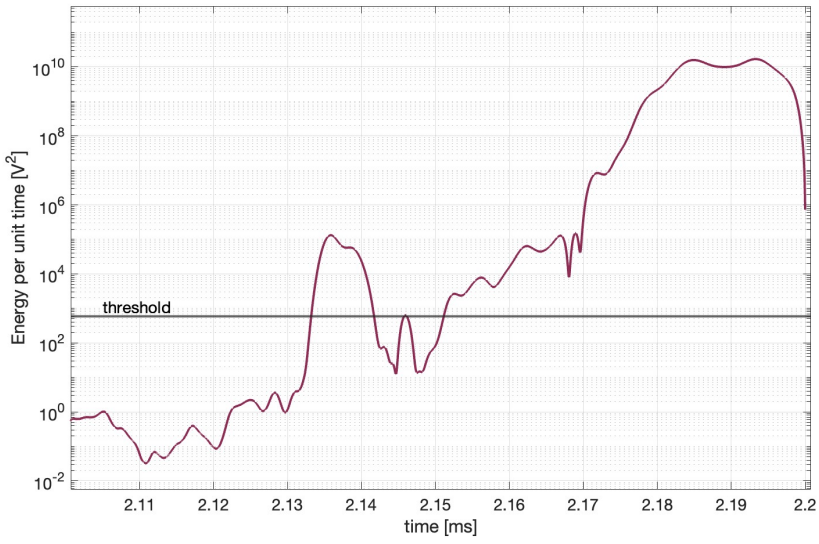

Figure 6.8: Energy content of the signal in the 100kHz to 200kHz band retrieved from the Wigner-Ville transform for experiment 33.

[2]This does not really output the energy as the result should be multiplied by the time-step. Being the time-step of the acquisition constant this would simply result in a re-scaling of the plot.

The time of arrival of the extensional mode estimated with this process is very close to what was obtained by visual inspection of the data, as Figure 6.9 shows. The time estimated this way differs from the time selected manually by a very small amount (in the order of 10^{-6}s, and is accurate enough for the algorithm to converge to a solution.

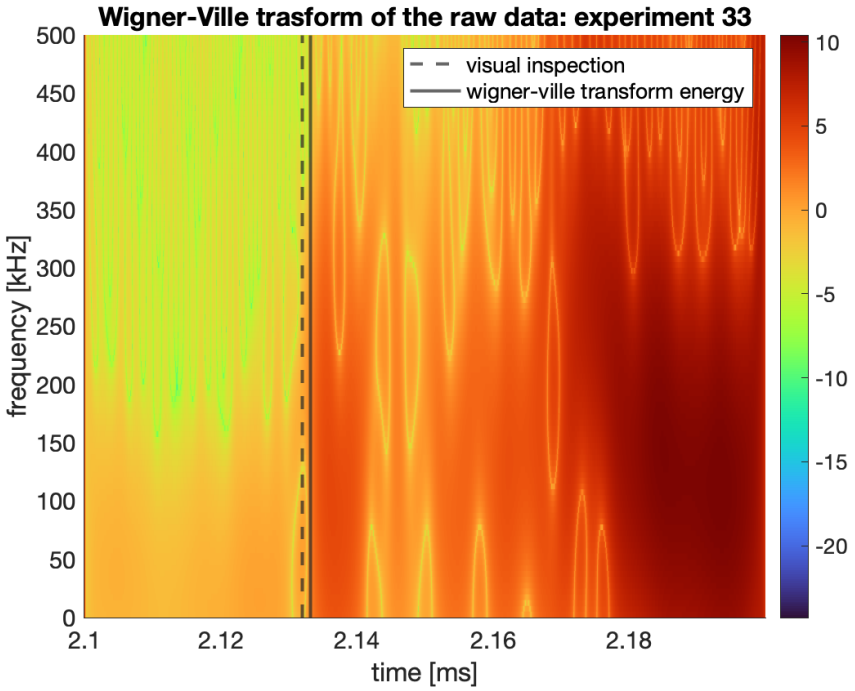

Figure 6.9: Wigner-Ville transform of the data in experiment 33 with overlapped the time of arrival of the extensional mode as obtained from visual inspection and study of the energy content of the signal.

The method here describes shows a promising way to automate the identification of the point of impact of the projectile on a spacecraft. Given the potentially large amount of data points that can be generated by equipping spacecraft with an AE debris and micrometeoroid detection system, the processing of the raw data must be as autonomous as possible as relying on human input for the identification of the time of arrival of the extensional wave would require a non-negligible amout of man power that could be avoided.

7

Frequency Content of the Vibrational Signal

The wavelet transform of the raw signal is a powerful tool that allows for a better understanding of the behaviour of the signal, even in cases when no actual data is extracted from the transform: just a qualitative analysis of the scalogram can help in understanding the behaviour of the vibrations picked up by the sensors. While processing impact data from projectiles hitting the aluminium plate it was observed that the amplitude peaks of impacts from steel (Figure 7.1) and glass projectiles were at higher frequencies than impacts from PTFE (Figure 7.2). A difference in frequency content was also observed when comparing impacts on aluminium (Figure 7.2) and impacts on the sandwich panel (Figure 7.3) performed with the same projectile type. Changing the impact speed and location of impact doesn't seem to have such a big effect on the frequency content of the signal. The change in frequency

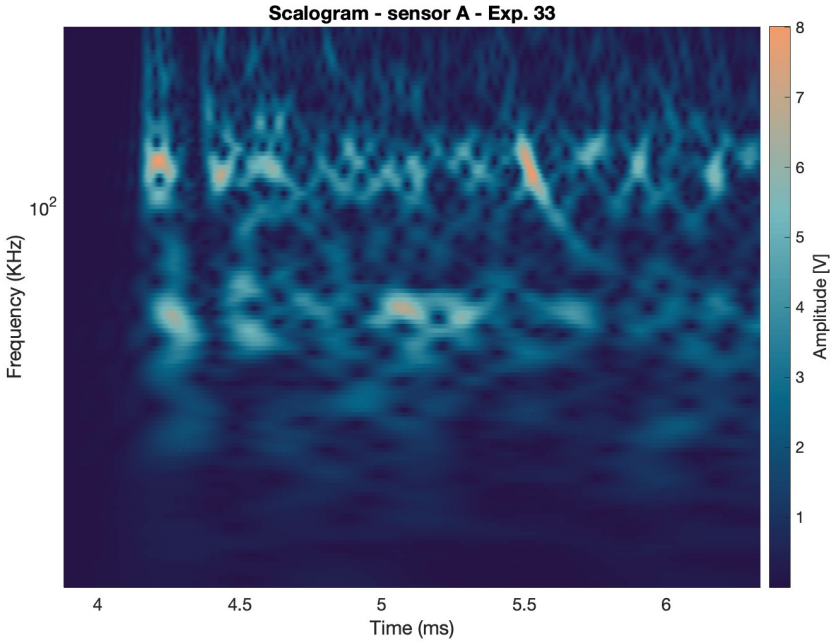

Figure 7.1: Scalogram of the data obtained from sensor A during experiment 33. Target: aluminium. Projectile: steel.

content of the signal measured changes with changes in the material of the projectile (or target) seems to indicate that contact mechanics phenomena are at least partly responsible for the vibration modes generated and the amplitude of each mode. This seems to indicate the possibility of characterising

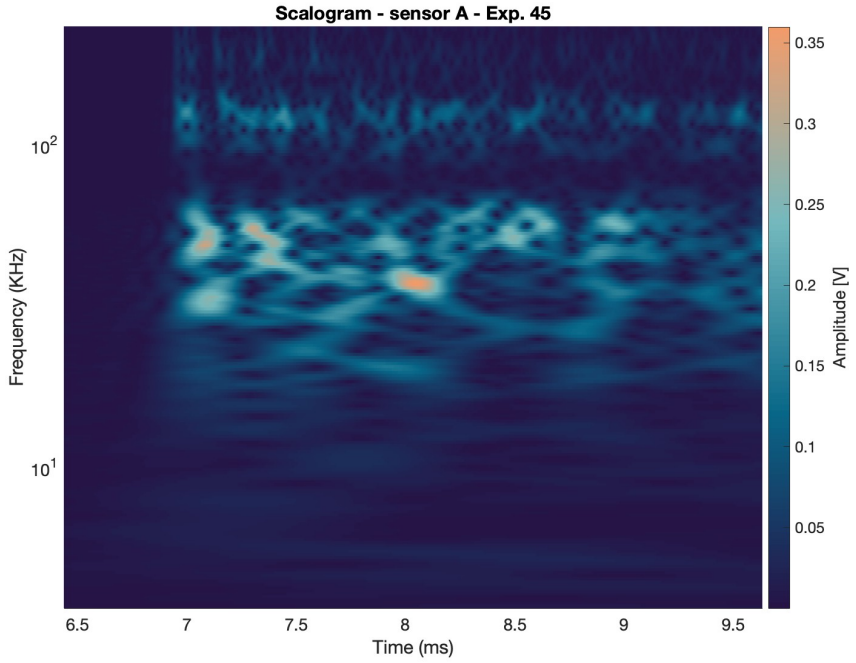

Figure 7.2: Scalogram of the data obtained from sensor A during experiment 45. Target: aluminium. Projectile: steel.

the material class of the projectile based on the frequency content of the signal. The steps taken to achieve this are described in this chapter, with strategies and results.

7.1. Data Processing

A way to systematically analyse the data had to be developed to go beyond what can be seen by simple visual inspection. The processing algorithm has been described in subsection 4.2.5, here the explanation of how the algorithm came to be and why will be described.

As discussed in subsection 4.2.2, the output of the wavelet transform is a matrix of size n by m. The number of rows n depends on the frequency resolution chosen and is equal to the number of frequency slots (i.e. the number of frequency scaling of the mother wavelet) performed during the transform. The number of columns m is equal to the number of data-points in the signal. Each cell contains a complex number that gives information on the amplitude and phase of the wavelet with the frequency associated to the given cell at the given time stamp. Taking the absolute value of each cell of the matrix gives information on the amplitude at each time step. If then a summation, row by row, is performed, the output is the sum of all the amplitudes that the wavelet of a given frequency assumes during the signal. This means that if a frequency is more present or is present with bigger amplitudes then the summation will be bigger. The result can then be normalised to obtain data in a percentage form that can be more intuitive to understand.

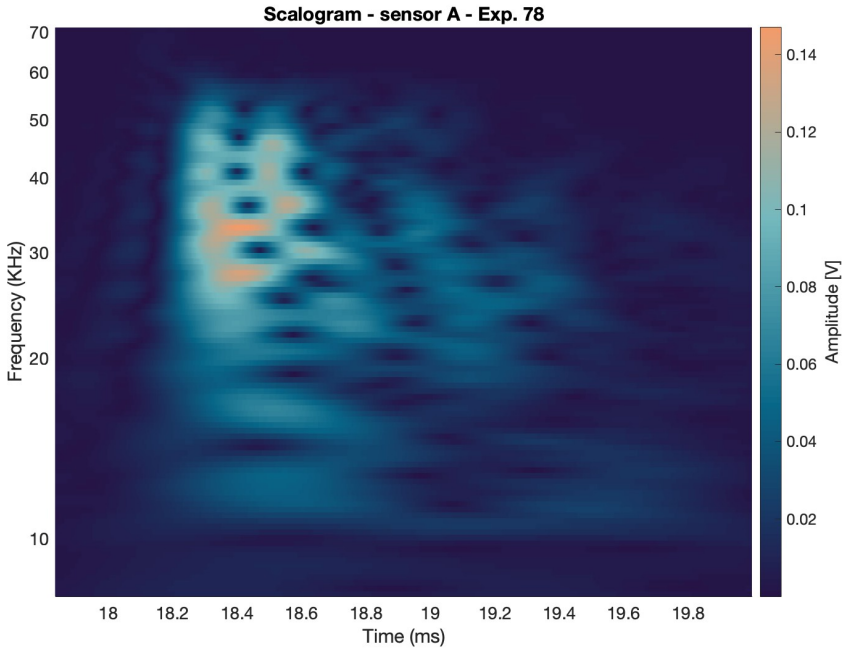

Figure 7.3: Scalogram of the data obtained from sensor A during experiment 78. Target: sandwich panel. Projectile: steel.

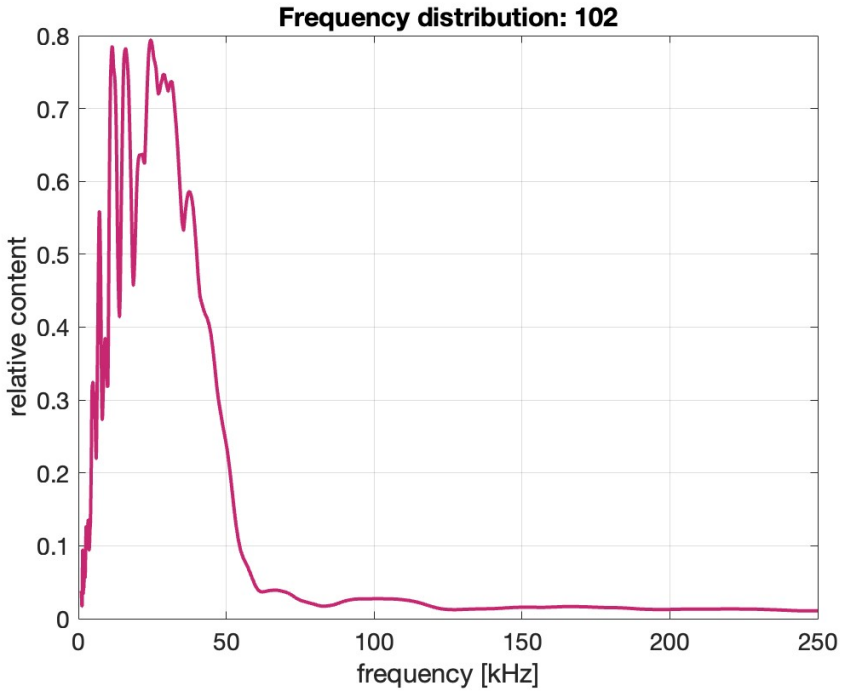

Figure 7.4: Amplitude content per frequency

Adding the amplitudes of the decomposing wavelet of a given frequency over time doesn't really bear any physical meaning, although it provides information on the frequency content of the signal. It was thus decided to consider the energy of the signal, defined in Equation 4.3. As shown in subsection 4.2.5 if the results are normalised with respect to the total energy content it is sufficient to perform the summation row by row of the squared value in the cells of the wavelet transform. Although the plots obtained are very similar to the previous ones, these have a more concrete physical interpretation. The

plots show the percentage of the signal energy carried at each frequency over the whole analysis time.

7.2. Analysis

In this section first the results of impacts on the aluminium plate will be analysed, focusing on the influence of the projectile material on the frequency content of the signal. The analysis of the effect of projectile material will then be done for impact data on the honeycomb plate. After that is done the results for the two plates will be compared.

7.2.1. Aluminium plate

After determining the frequency distribution as described in the previous section, plots for different projectiles where made on the same figure. The number of lines per projectile material was limited in order to keep the figure understandable. Figure 7.5 shows how the frequency content for different projectile materials compare.

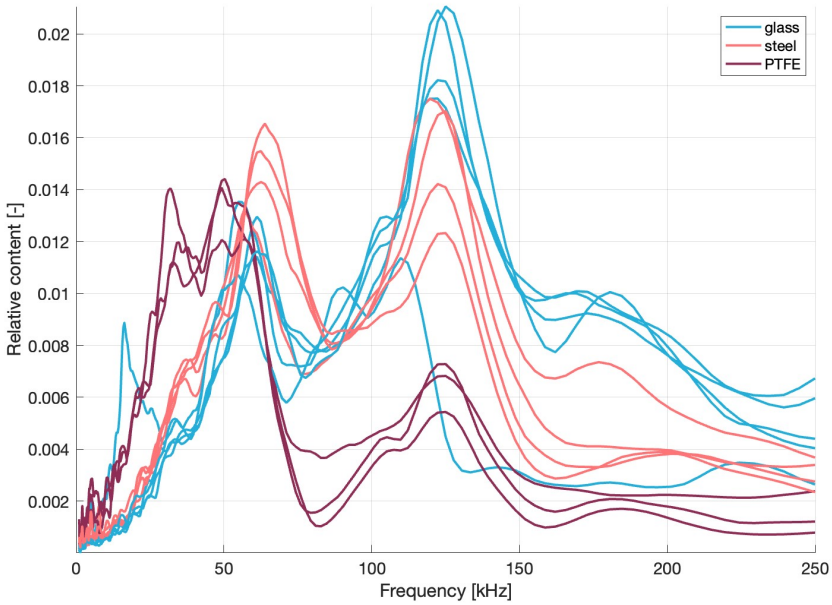

Figure 7.5: Amplitude-normalised frequency content for the aluminium plate

Looking at Figure 7.5 it can be seen how lines for the same material tend to group together and have similar behaviour. Glass and steel projectiles generate higher amplitude motion at higher frequencies when compared with PTFE: what was expected by simple visual inspection of the scalograms is now confirmed and the quantitative difference of the two material classes can be studied.
The vibrations generated upon impact are expected to depend both on the impactor (size, material, shape, etc.) and on the impacted structure, i.e. the target plate. Considering the objective of this research, any dependency of the signal on the impactor and not the structure is beneficial in characterising the debris or micrometeoroid that struck the satellite.
Glass and steel projectiles show two similar peaks at 65 kHz and 120 kHz. The peak at 120 kHz can also be observed in the curves for PTFE. These are expected to be natural vibration frequencies of the metal plate. The relative energy content at 120 Khz (chosen as all three projectile types have a local maxima at this frequency) is different for the different projectiles, implying that the material of the projectiles has an effect on the amplitude of the vibrations.
The interaction of the projectile and the plate happens over a small (but non-zero) time interval. During this interval the plate starts vibrating and the projectile is still transferring part of its energy to the plate. During this contact time, it is hypothesised that the projectile can act as a dynamical dampener [55]. The three projectiles, being of different material, also have different Young modulus and thus acoustic and mechanical impedance. These properties describe the materials' ability to transmit vibrations at

a given frequency. Teflon's ease of deformation could make it especially good at dampening higher frequencies of vibrations.
Despite the various lines in the plot being grouped, the effect is emphasised by the different colours used for the plot. In a real application of the debris and micrometeoroid detector being investigated in this thesis, it should be possible to classify the material of the projectile solely based on the frequency distribution. This means finding in Figure 7.5 features that are only possessed by one type of projectiles. For example, the peak at 60 KHz might not be a good idea due to glass and steel having similar amplitudes in some cases, making it hard to identify a cutoff level to separate glass and steel.
Looking at Figure 7.6, which shows the frequency distribution at lower frequencies, it can be noted that PTFE has a much higher relative energy content when compared to both glass and steel, in particular the local maxima at around 32 kHz can be used as an indicator for this material. Another feature the only the frequency distribution for PTFE displays is the local minimum between 80 and 85 kHz. Both glass and steel display minima around 80 kHz but for teflon the energy content at this frequency is much lower, making it easy to separate it from the other two materials. Lastly, the peak at 120 kHz for teflon is at a much lower level than for either glass or steel, making this another potential marker for materials with properties similar to teflon.
When it comes to glass and steel finding characteristics possessed by one material and not the other is much harder, probably due to their similar hardness and elasticity that result in similar contact mechanics phenmena taking place during impact. Nonetheless some potential markers have been identified. Between 35 and 40 kHz the energy content for the two materials shows a different behaviour: for glass the energy content keeps growing until a local maxima or a plateau while for steel it decreases to a local minimum, as Figure 7.8 shows.

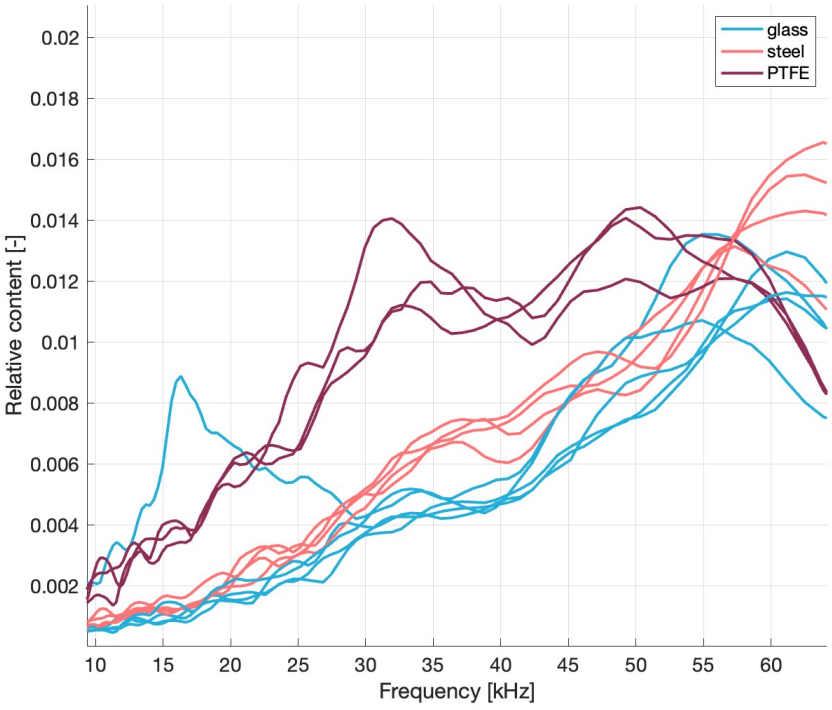

Figure 7.6: Amplitude-normalised frequency content for the aluminium plate from 10 to 60 kHz.

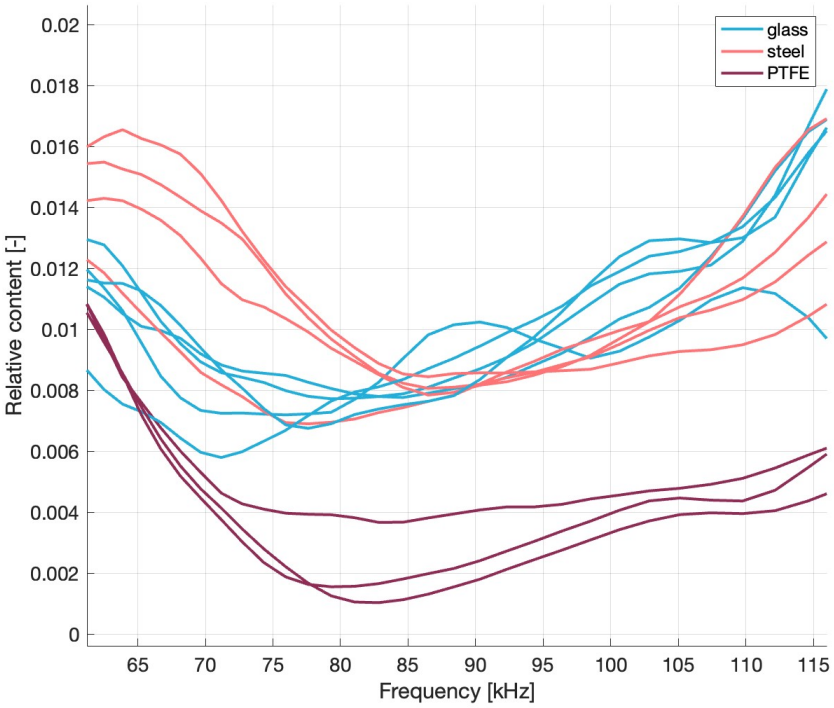

Figure 7.7: Amplitude-normalised frequency content for the aluminium plate from 10 to 60 kHz.

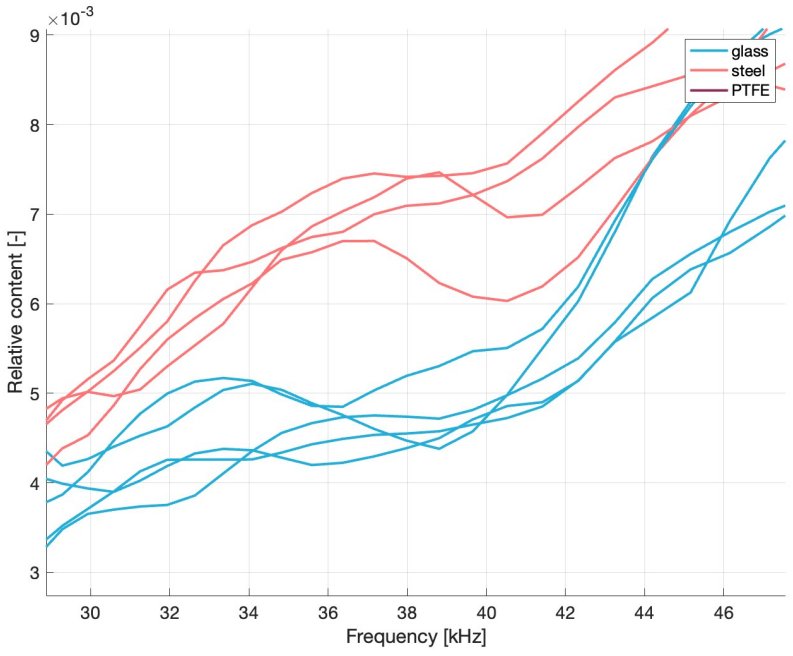

Figure 7.8: Amplitude-normalised frequency content for the aluminium plate from 30 to 45 kHz.

7.2.2. Sandwich panel

As with the aluminium panel, a plot with the frequency distribution of the vibrations generated by impacts of different materials was generated. The first observation that can be made, for the plot as a

whole, is that low frequencies have much bigger amplitudes when compared to the frequencies of the aluminium plate, as Figure 7.9 shows. This seems to confirm that when plasticity occurs, the frequency of oscillation of the plate are lower. To generate a clearer plot a limited number of lines were displayed. It can be seen how no clear difference between projectile material exists, as in the case of impacts on aluminium. This lead to a more detailed analysis of the frequency distribution.

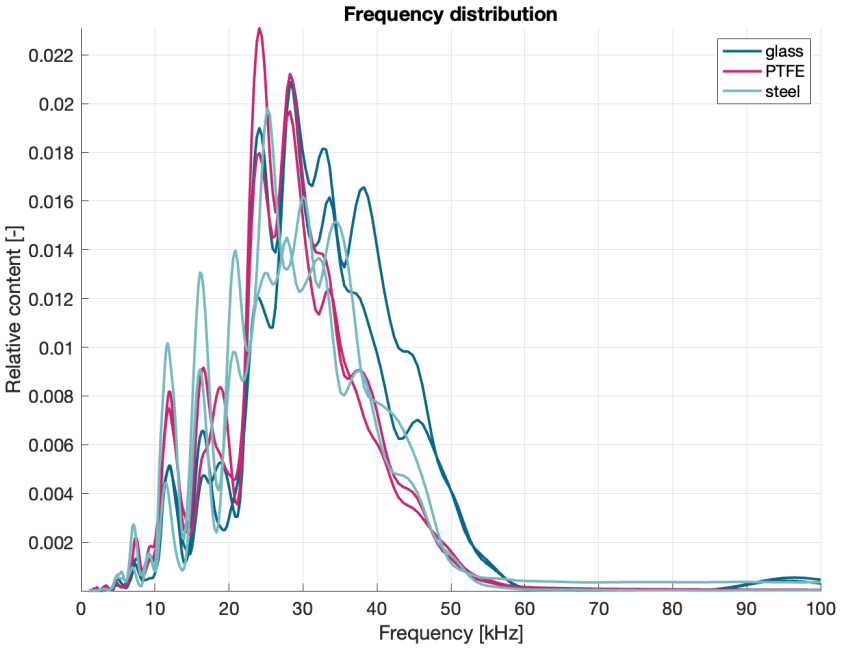

Figure 7.9: Amplitude-normalised frequency content for the sandwich panel.

Impacts with PTFE

A number of shot with PTFE projectiles were performed, at different speeds, and the results plotted on the same plot to compare how different impact speeds affect the frequency distribution. Despite all the lines in the plot showing similar characteristics, like the minima at 15 and 22 kHz, a lot of variability is seen and no clear dependence on speed can be observed, as Figure 7.10 shows. To better understand this an analysis of impacts at low, medium and high speed was performed

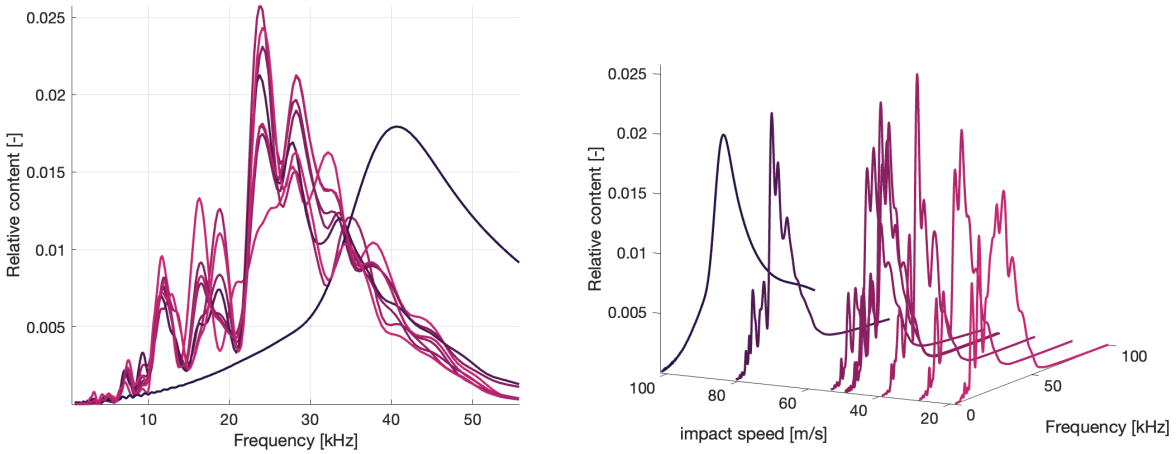

Figure 7.10: Energy content per frequency with respect to the total energy of the signal, for PTFE projectiles impacting an aluminium sandwich panel and plot showing the frequency distribution at the impact speed that generated it.

At the lower end of the speed spectrum, at around 20 m/s, it seems like no similarities in the frequency distribution can be seen. Figure 7.11 shows how only some of the peaks in the data are common between the two curves: the peaks below 10 kHz and the peak at 26 kHz, in addition to the behaviour between 10 and 15 kHz. These are the experiments with the lowest amount of plasticity of the projectile due to the very low speeds upon impact meaning that the effect of the projectile material is expected to be small.

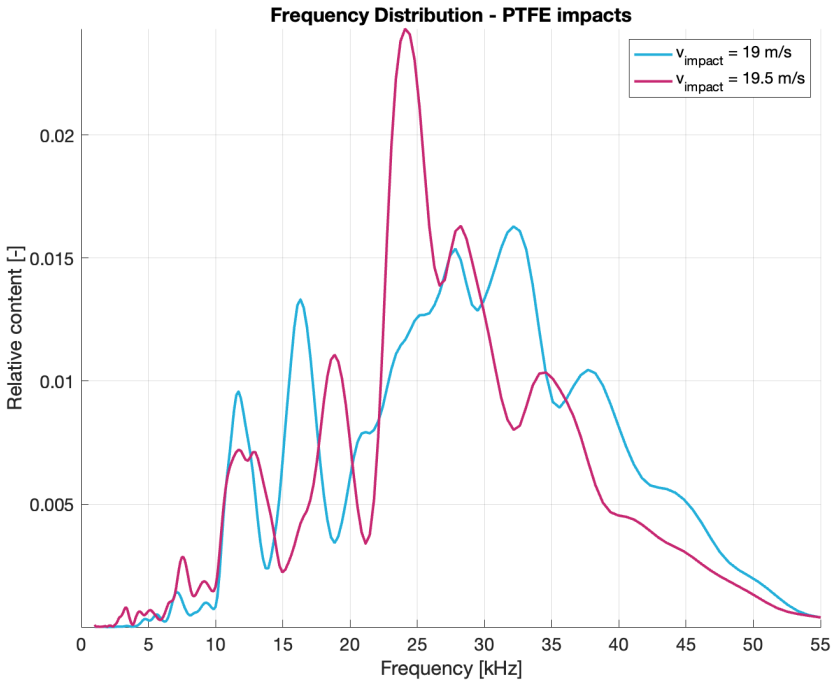

Figure 7.11: Frequency distribution of impacts at low speed

Increasing the speed in the range of 30 to 50 m/s gives the frequency distribution shown in Figure 7.12. The curves of different experiments display a higher grade of similarity when compared to those of lower speeds. In particular the peaks at 12, 23 and 27 kHz are common to all the curves. In the range of 15 to 20 kHz it can be seen how the curves have similar minima at 15 and 20 kHz, but different behaviour between these two, although two families of curves can be observed. As the speeds are higher than the ones in Figure 7.11, the projectiles experience a higher degree of deformation, resulting in a bigger influence of the chip material on the waveform and, as a consequence, its frequency content.

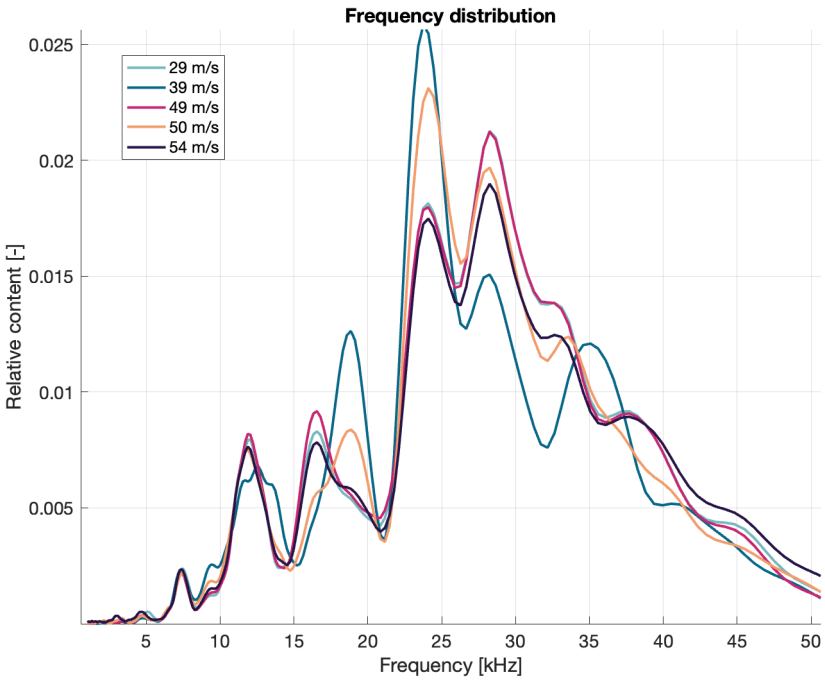

Figure 7.12: Frequency distribution of impacts at low speed

Lastly, the high speed regime will be analysed. The three shots with the highest speed were considered, excluding the one that was already identified as an outlier. The result of the determination of the frequency distribution is given in Figure 7.13. Although, given the increased speed it would be expected to have curves with more similarities than those in Figure 7.12, this is not the case.

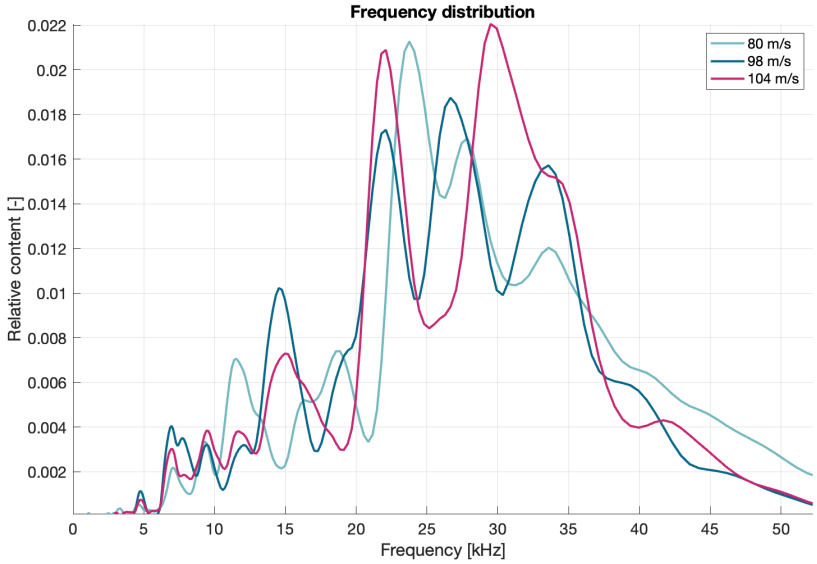

Figure 7.13: Frequency distribution of impacts at low speed

When it comes to PTFE it seems that speed has no clear effect, with only shots in the mid range having similar behaviour.

Impacts with glass

A similar analysis to the one carried out in the previous section has been performed for glass projectiles. Looking at the first plot in Figure 7.14 no general trend can be seen with every line having slightly different frequencies for the maxima and minima. Only one feature can be seen: the shots at the highest speed (above 120 m/s) have a very distinct peak between 30 and 40 kHz that others curve don't seem to have. As no other commonalities can be found in this plot the curves will be analysed by speed level, from low to high speeds, while looking for structure in the frequency distribution.

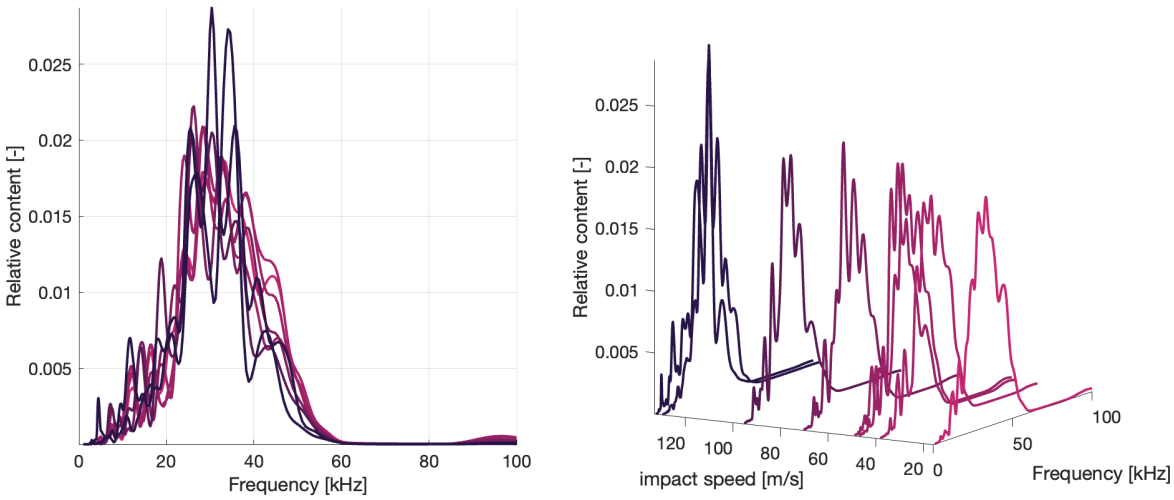

Figure 7.14: Frequency distribution of impacts at low speed. Target: sandwich panel. Projectile: glass beads.

At lower speeds there doesn't seem to be a trend, except for very low frequencies (below 20 kHz), where both curves in Figure 7.15 have maxima and minima at the same frequencies. This is the same behaviour observed for low speed impacts with teflon.

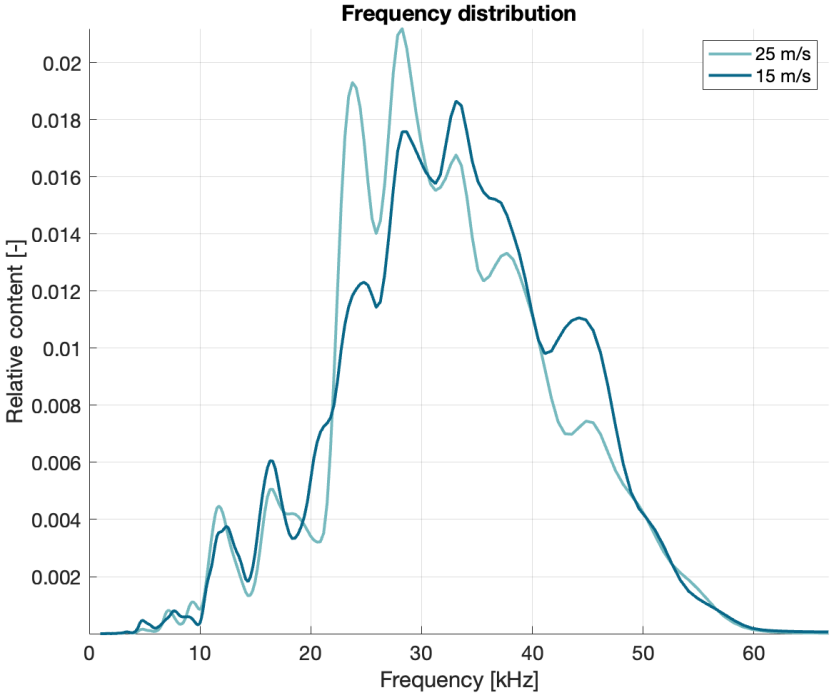

Figure 7.15: Frequency distribution of impacts at low speed. Target: sandwich panel. Projectile: glass beads.

At slightly higher speeds the frequency distribution doesn't show any structure, as confirmed by Figure 7.16 where commonalities can be seen only for very specific peaks. An example of this is the peak at 32 kHz that three curves possess, despite having no other common patterns at the other frequencies.

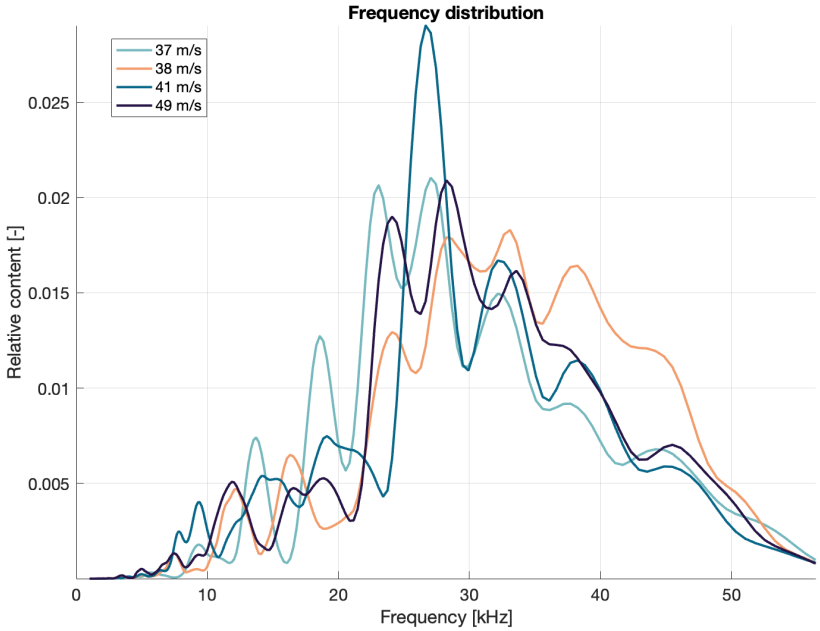

Figure 7.16: Frequency distribution of impacts at low speed. Target: sandwich panel. Projectile: glass beads.

Looking at Figure 7.17 the peaks discussed in the beginning of the section become more clear. What can be seen in the figure now that only three curves are present is that in the range from 23 to 38 kHz the three curves have peaks at the same frequencies, what changes is the magnitude of the peaks. Outside of this frequency band no patters can be seen.

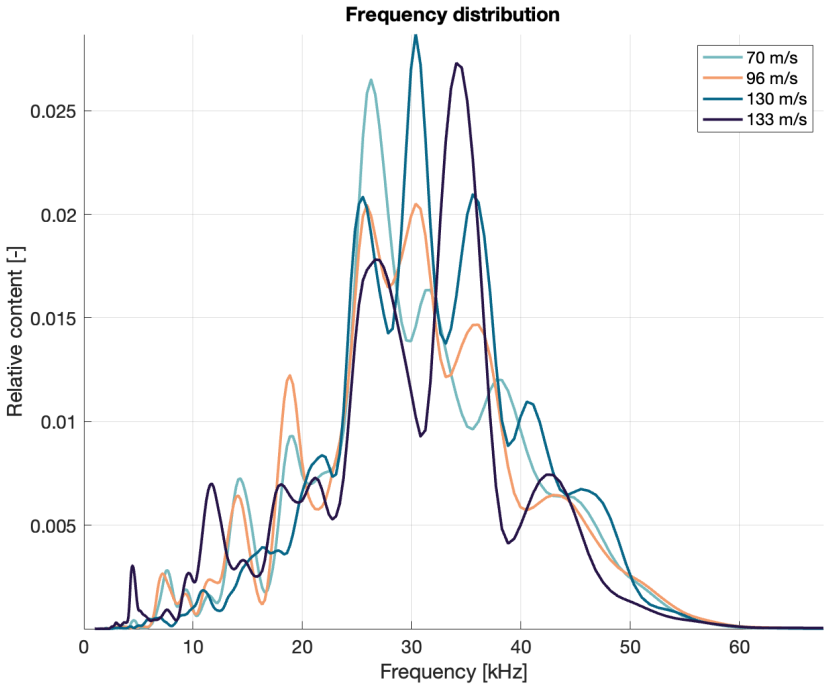

Figure 7.17: Frequency distribution of impacts at high speed. Target: sandwich panel. Projectile: glass beads.

Impacts with Steel

Lastly the impacts with steel beads will be analysed. Figure 7.18 shows all the curves with the frequency distribution due to impacts with steel beads: once again, as for glass and PTFE bead impacts on the sandwich panel, no clear structure in the data can be seen. When it comes to impacts at low speed, the features present in the case of teflon and glass can't be seen, in particular even looking at the part of the plot relative to low frequencies maxima and minima show no pattern whatsoever.

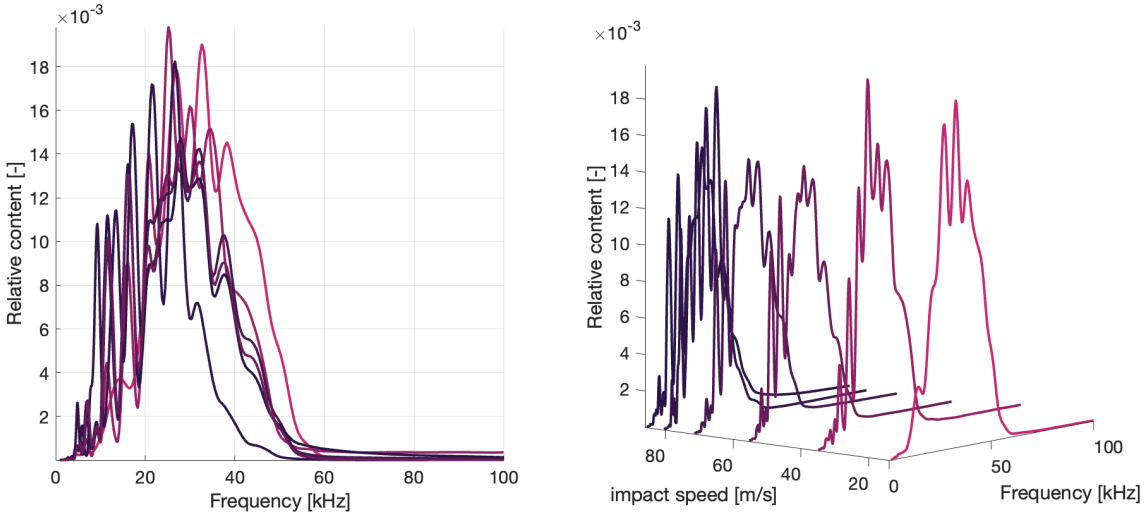

Figure 7.18: Frequency distribution of impacts at high speed. Target: sandwich panel. Projectile: glass beads.

At slightly higher speeds the curves show a very similar behaviour, as seen in Figure 7.20. Maxima and minima can be seen at the same frequencies and with very similar magnitude. The same behaviour was observed in the case of PTFE beads.

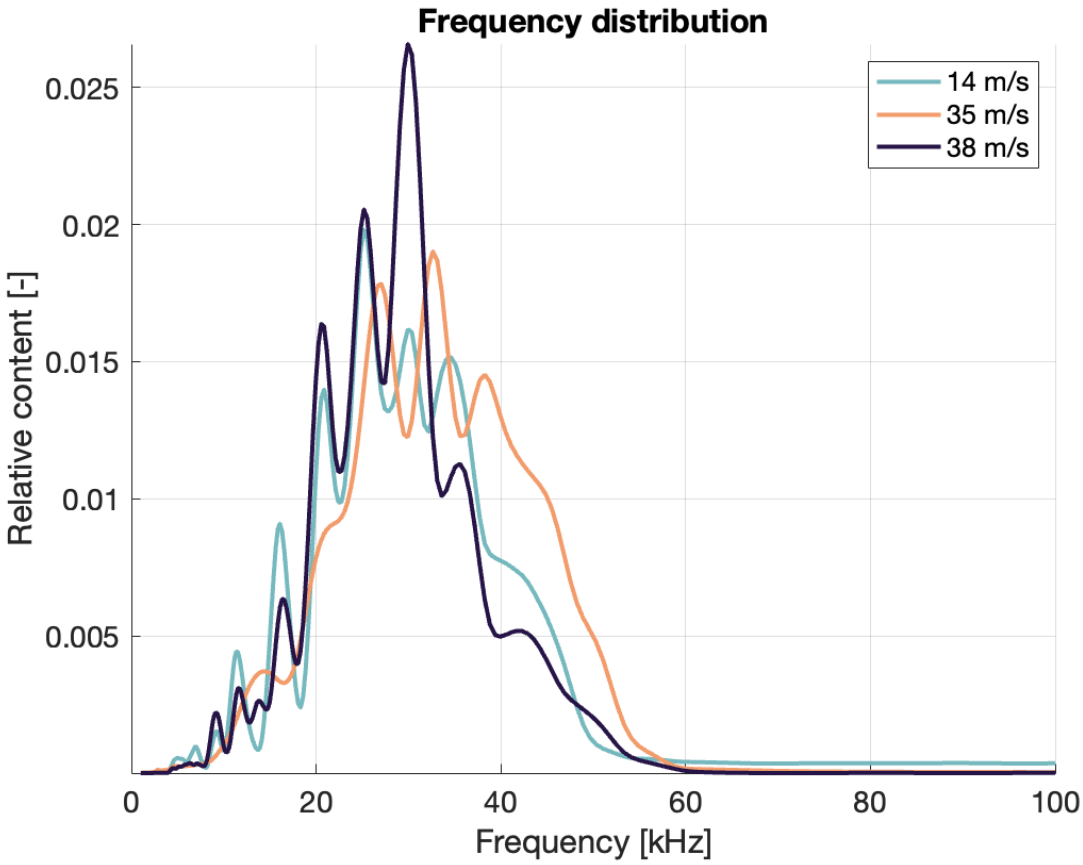

Figure 7.19: Frequency distribution of impacts at high speed. Target: sandwich panel. Projectile: steel beads.

The frequency distribution of the data obtained at higher speeds can be seen in Figure 7.21. Despite peaks and valleys happening at different frequencies for the two curves, it is interesting to note that the two curves seem to have the same shape, just horizontally shifted. The reason for this behaviour is not known.

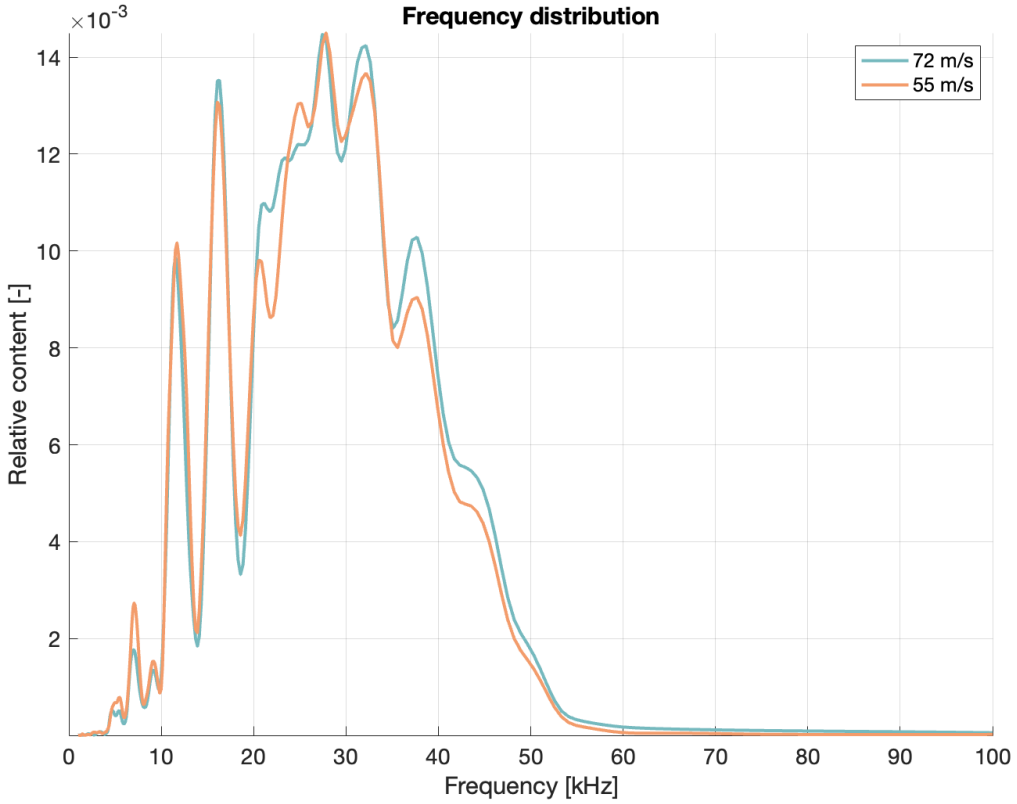

Figure 7.20: Frequency distribution of impacts at high speed. Target: sandwich panel. Projectile: steel beads.

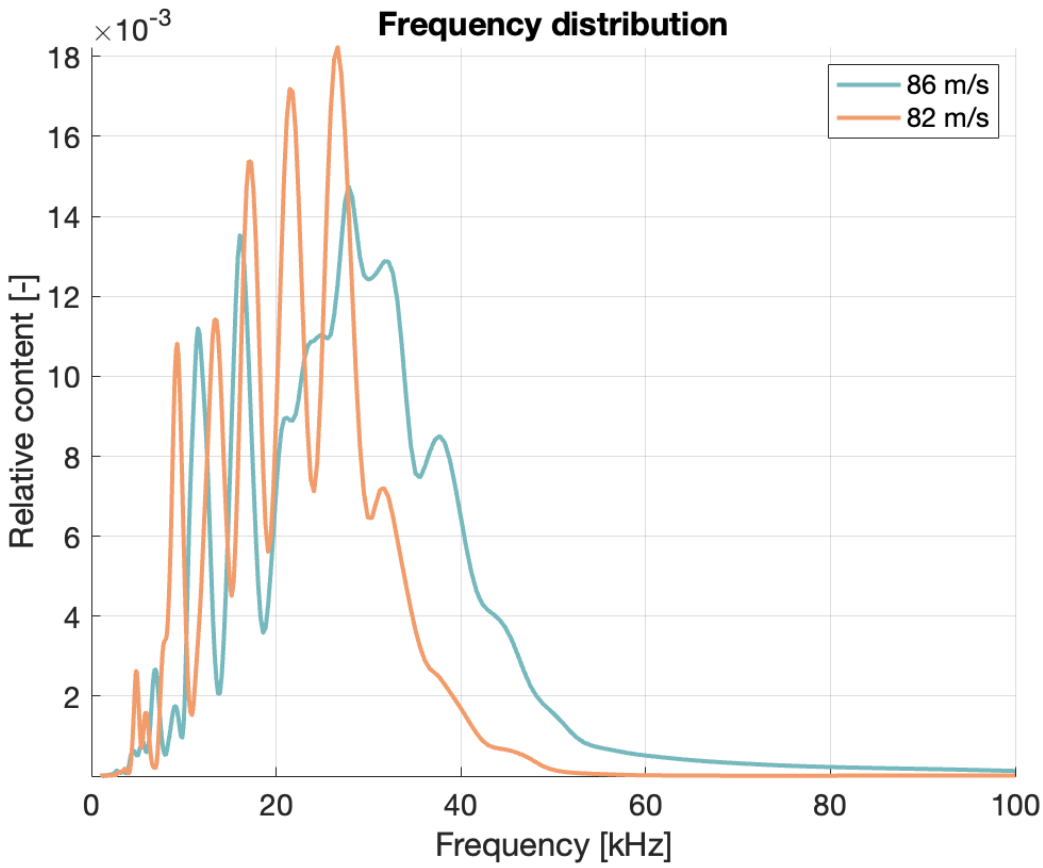

Figure 7.21: Frequency distribution of impacts at high speed. Target: sandwich panel. Projectile: steel beads.

Conclusions on the frequency distribution of the vibration signal

Now that the frequency content of the signal has been analysed for the two plates and the different projectiles used, some patterns in the data and common behaviours can be found.

In general, it was observed how plastic phenomena (permanent deformation) lead to lower frequencies in the signal, both in case of deformation of the projectile or the plate. This was seen in the case of the aluminium plate, with teflon projectiles (deformed after impact) generating much lower frequencies than projectiles made of glass or steel. When comparing impacts with the same projectile on the two plates, the frequencies in the aluminium plate are much higher than those of the sandwich panel. Once again, the sandwich panel exhibits much bigger deformation due to impact. Considering the objective of this study, which is to investigate the possibility of using vibrations to characterise the debris and micrometeoroids that generated them, having a rigid structure seems to be the best choice. This would lead to most of the plasticity happening on the impactor side, as opposed to the plate side, generating different vibrations based on the material and structure of the debris and micrometeoroid. Although this won't allow for material identification, it can aid researchers in classifying the material based on its rigidity.

The sandwich panel showed less structure in the data and the families of curves seen in Figure 7.5 can't be seen. One one hand this is probably due to the narrower band of frequencies present in the data: a lot of the differences in the frequency distribution of shots on aluminium were seen at frequencies higher than 50 kHz, completely absent in the case of the sandwich panel. Additionally, the sandwich panel is non-homogeneous and impacting in the centre of an octagonal face, on one of the sides or at an intersection will result in a different amount of energy transferred to the other side of the panel (where the sensors are) and possibly to different frequencies of vibration. Additionally, the honeycomb cells generate a high amount of reflection and refraction leading to the so-called vibration coupling effect [56], that will lead to a higher degree of distortion of the signal generated upon impact.

For steel and PTFE projectiles it was observed how at medium speed the frequency distribution for

different shots has the same set of maxima and minima while at low and high speeds this was not observed. It is interesting to note how in the case of impacts on the aluminium panel glass and steel beads showed a similar behaviour while in the case of impacts on the sandwich panel it does not happen.

8

Effect of impact speed of the signal

One of the parameters of interest when detecting debris and micrometeoroids is their speed. In the case of the detection method investigated in this research, means the speed of the impactor relative to the detector and thus the satellite.
Experiments performed by other research groups showed that only the component of the velocity orthogonal to the target plane has an effect of the signal [40]. This led to the decision of not investigating the effect of the impact angle. The fact that only the component of velocity orthogonal to the plate impacted affects the signal limits the information on the impactor that can be retrieved: two impacts with very different velocity but similar (or identical) normal velocity would generate a very similar signal.
Initial tests showed that impacts performed with projectiles of the same material and size, travelling at the same speed and impacting at different distances from a given sensors resulted in signals with different amplitude and feature: this means that for an effective comparison of different experiments a correction to the signal must be introduced that takes into account dissipation of vibrational energy.
A number of impacts with projectiles of the same type were performed across all the speed spectrum of the accelerator[1]. In order to reduce external influences on the data being recorded the shots were aimed at the central part of the plate, away from the edges.
Initial processing of the data was focused on finding which feature of the signal should be correlated with the impact characteristics. The maximum voltage recorded by the sensors was used. The maximum signal energy and total signal energy were also considered but were discarded due to the big effect that vibration reflection and refraction has on their magnitude. In terms of features of the impactor related to speed, in addition to the speed itself, momentum and energy were considered and compared to the maximum voltage generated. No connection was observed between impact speed and maximum voltage as mass of the projectile also plays a role in the contact phenomena during impact. It was thus decided to use the projectile momentum and compare it with the maximum voltage generated upon impact.

8.1. Effect of momentum on the signal

It can be expected that an increase of momentum of the impacting projectile results in higher amplitude of the vibrations and, as a consequence of the voltage picked up by the piezo-sensors. To study the effect of momentum on the vibrations the momentum of the projectile was plotted with the equivalent maximum voltage measured. This was done separately for the different projectiles impacting the sandwich panel. It must be noted that all the projectiles of the same material have the same size (and thus mass): this results in different momentum due to only changes in the impact speed of the projectile.
In Figure 8.1 the plot for projectiles made of PTFE impacting the sandwich panel is shown. The data shows a clear linear trend: increasing momentum leads to an increase in the amplitude of the vibrations. This is the data from sensor A, data from all the other sensors shows a very similar behaviour but was not plotted in the same figure for clarity.

[1] During testing the coil of the accelerator broke. Due to excessive shipping times for a new coil it was decided to fix the existing one. Removing the broken section led to the decrease in the number of coil turns and thus a lower top speed achievable

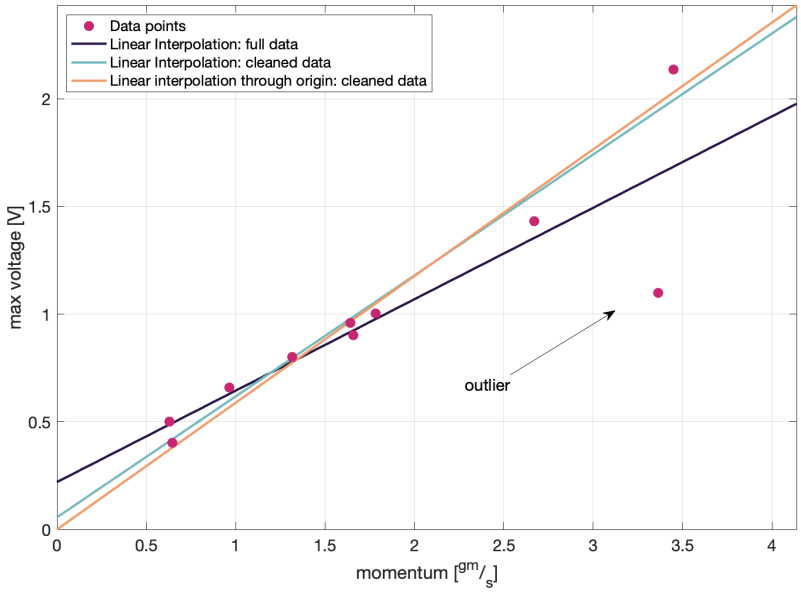

Figure 8.1: Maximum signal voltage as a function of the momentum of the impacting projectiles. Projectile material: PTFE. Target material: sandwich panel.

Although most of the data points follow this linear trend, there seems to be one outlier. This unusual behaviour lead to further investigation of that impact (experiment 94). In particular the scalogram (and the frequency dsitribution derived from it) of the signal provides insight into the assumed reason for this reduction in amplitude of the vibrations despite the high velocity impact. The frequency distribution of the signal generated by this impact, shown in Figure 8.2, looks very different to those that are discussed in chapter 7. There is only a single peak and the curve is overall very smooth. The different behaviour of the curve is even clearer when compared with the frequency distribution of experiment 61, shown in the same figure. The two experiments were performed with very similar parameters: same projectile material and size, same impact location (within a few cm due to dispersion of the shots) and very similar speed (difference of 3 m/s). In chapter 7 it was observed that when deformation phenomena take place, the number of peaks in the frequency distribution plots is lower as compared to experiments with less deformation effects. These phenomena include deformation of the projectile and/or of the target. This suggests thus that in this particular experiment a high degree of plasticity occurred. This could be explained by the impact hitting the centre of one of the hexagons of the honeycomb structure: this leads to a big deformation of the structure and a lower amount of energy transferred to the other side of the panel (where the sensors are)[57] confirmed by the low voltage registered by the data acquisition system. Due to this it was decided to not consider this data point in further processing of the data.
Three linear fits are shown in Figure 8.1, one including the outlier and two with the cleaned data set. Of these last two linear fits one more closely matches the data, as confirmed by Table 8.1. Nonetheless it was decided to use the linear fit passing through the origin as it makes the most physical sense: at zero-momentum the maximum voltage detected should be zero.

	RMS - Root Mean Square
Linear fit	0.0805
Linear fit through origin	0.0848

Table 8.1: RMS of the linear fits for the momentum vs voltage plots for PTFE.

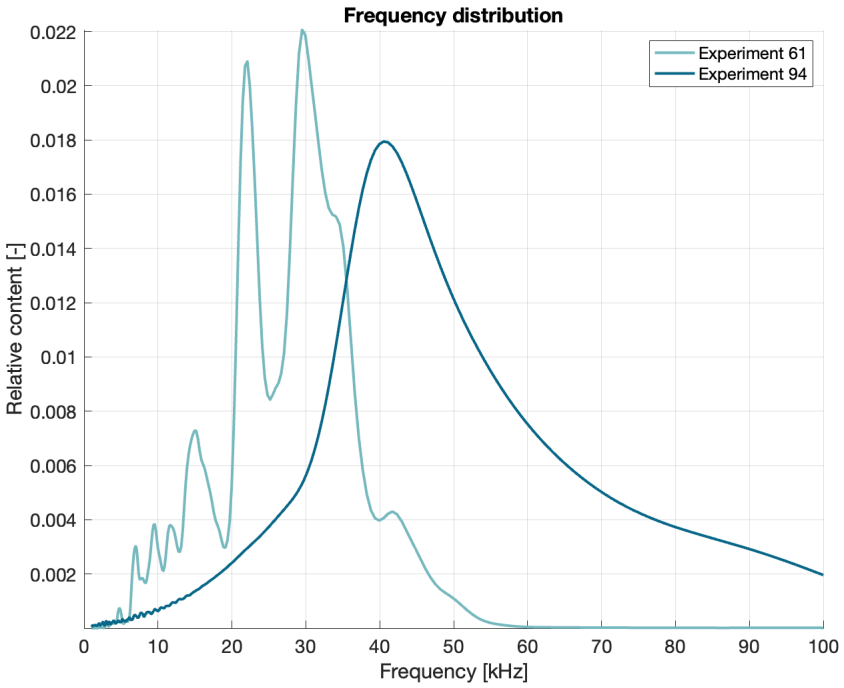

Figure 8.2: Frequency distribution of the experiments 94 and 61, showing the different behaviour of the signal Projectile material: PTFE. Target material: sandwich panel.

A similar set of experiments was performed for glass projectiles leading to the data (including linear fit) shown in Figure 8.3. The range of momentum and voltage registered is very similar to the ones obtained with PTFE projectiles. More dispersion of the data with respect to the fit can be observed. The reason for this is unclear. One hypothesis is due to the dissipation of the vibrational energy from the moment it is generated on impact to the moment it is picked up by the sensors. Higher frequencies have a higher coefficient of dissipation [58] and glass generates vibrations at a frequency that is higher than that of teflon: this means that even small variations in distance of the impact and sensor could influence the maximum voltage measured.
As done for teflon, two linear fits are proposed: one standard and one passing through the origin. In this case, the second fit is the one with the lowest RMS (Table 8.2), being in this way both a better fit and more representative of reality.

	RMS - Root Mean Square
Linear fit	0.504
Linear fit through origin	0.251

Table 8.2: RMS of the linear fits for the momentum vs voltage plots for glass.

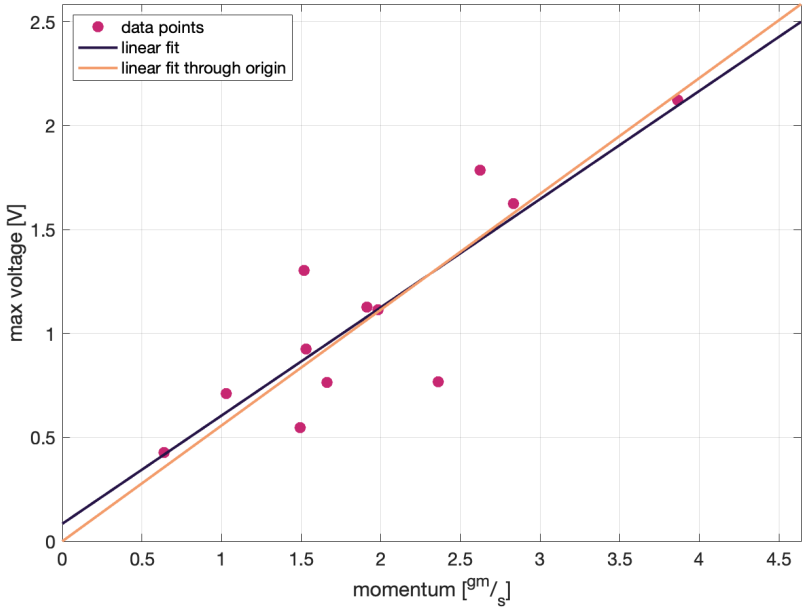

Figure 8.3: Maximum signal voltage as a function of the momentum of the impacting projectiles. Projectile material: glass. Target material: sandwich panel.

Projectile material	Linear fit slope [V s/ g m]
PTFE	0.0848
glass	0.251

Table 8.3: Value of the slope of the linear fit for the maximum voltage measured as a function of the impact momentum for glass and teflon projectiles.

Given the very similar range of momentum obtained with glass and teflon a plot comparing the two sets of data was generated. The two lines showing the linear fit show a very similar slope (as confirmed by Table 8.3). The fact that this happens is of great importance as it seems to indicate that it is possible to estimate the impactor's momentum without knowing its composition. In a real-life application of the detection technique being investigated the material of the piece of debris or micrometeoroid is unknown: being able to identify the (normal) component of the impactor's momentum is still possible.

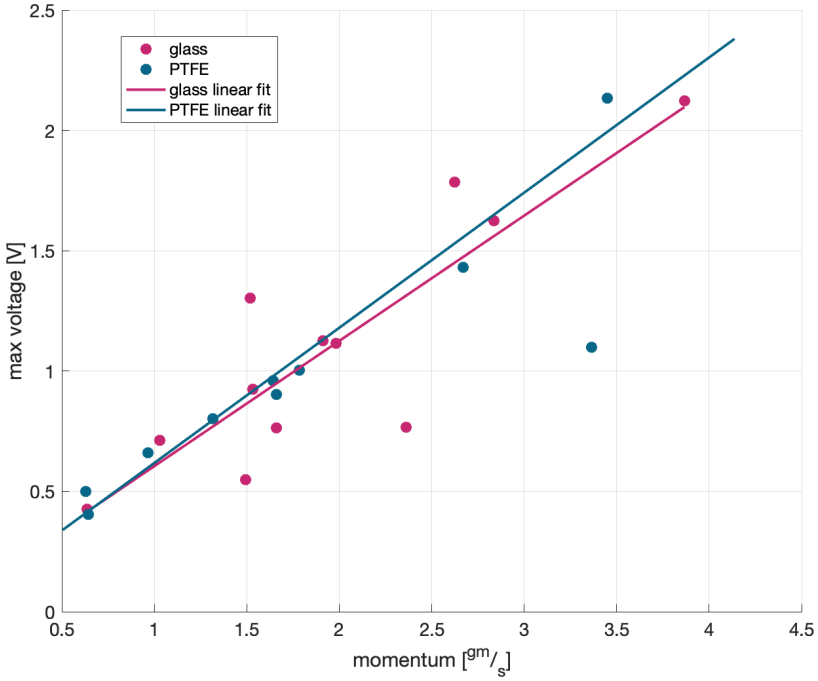

Figure 8.4: Maximum signal voltage as a function of the momentum of the impacting projectiles. Projectile material: glass and teflon. Target material: sandwich panel.

Steel projectiles were omitted so far due to their higher weight, resulting in the minimum momentum achievable being significantly higher than the minimum momentum obtained with glass and teflon. The maximum voltage obtained and the given momentum for steel projectiles have been plotted in Figure 8.5, the linear fit for the teflon and glass data has been included for comparison. The plot shows how the first two data points seem to follow the linear trend of glass and PTFE, while the maximum voltage at higher values of impact momentum doesn't grow as much. This behaviour seems to confirm what was found in previous experiments by other research groups [59] [60]: the maximum amplitude of vibrations increases with increasing momentum of the projectiles, until a plateau is reached. With higher and higher impact speeds, the material deforms more and more, creating bigger amplitude vibrations. At the same time, due to deformation of the material more and more energy is lost in deformation phenomena (as compared to elastic impacts at lower speeds). This explains why the slope of the curve goes flatter and flatter. Additionally, the maximum amplitude of vibrations will be achieved when penetration happens, and the tensile strength of the material is exceeded. This means that a maximum amplitude of the flexural mode exists. Although the speed regime of the experiments is low (being thus far from penetration speeds), the skin of the honeycomb panel was quite thin leading to bigger deformations.
So far the maximum voltage has been used as an estimator for the amplitude of vibration of the panel. Given the complex nature of surface waves and Lamb waves, it may be the case that this is not the best way to assess the displacement of the plate. In chapter 7, the energy content of the signal was calculated to obtain the frequency distribution of the signal. The maximum energy of the signal was thus re-used and plotted as a function of voltage to observe if this changed anything in the analysis. Figure 8.6 shows that using the energy of the signal as an estimator for the momentum leads to glass and teflon having a much more similar slope (Table 8.4 confirms this). The reason for this could be due to the time-varying nature of the signal obtained from the piezo-sensors (and thus of the vibrations). In additions to the signal's features changing over time, at any point in time multiple frequencies are present in the signal. Using the energy of the signal accounts for both the effect of amplitude and frequency.

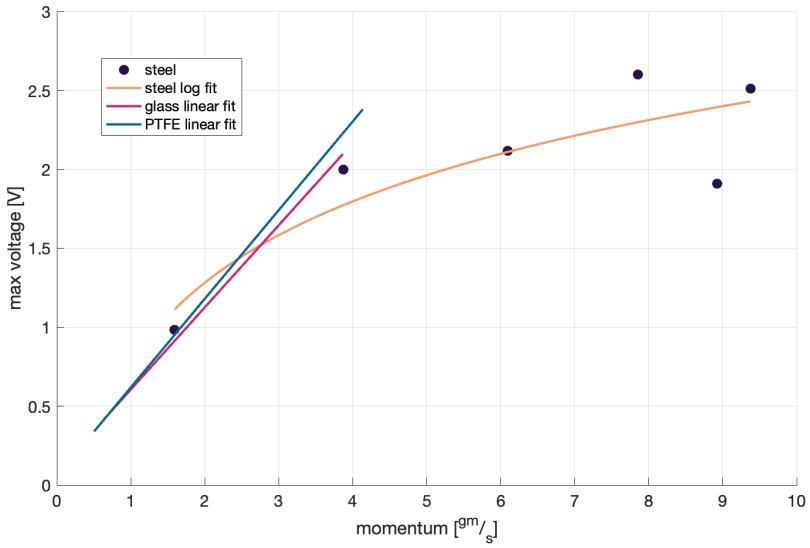

Figure 8.5: Maximum signal voltage as a function of the momentum of the impacting projectiles. Projectile material: glass, teflon and steel. Target material: sandwich panel.

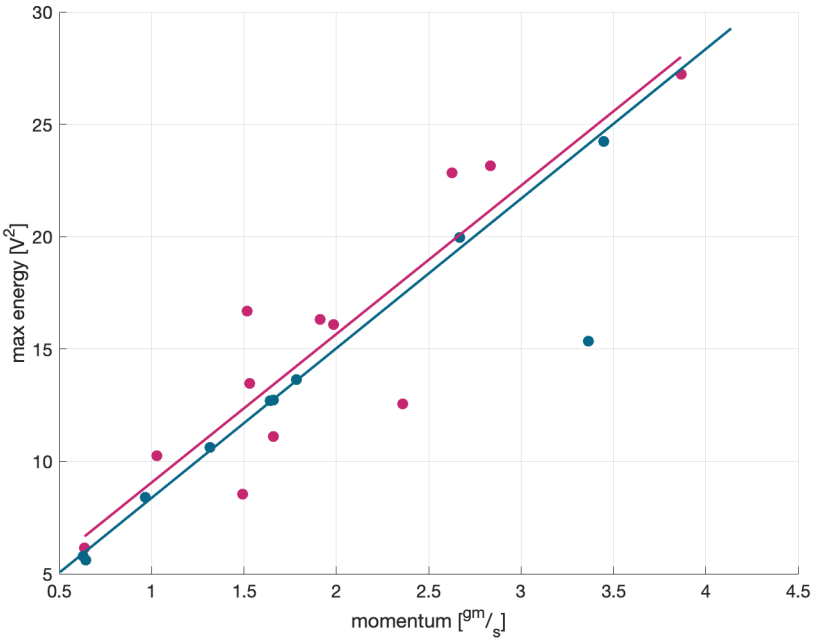

Figure 8.6: Maximum signal energy as a function of the momentum of the impacting projectiles. Projectile material: glass and teflon. Target material: sandwich panel.

Projectile material	Linear fit slope V^2 s/ g m
PTFE	6.6558
glass	6.6045

Table 8.4: Value of the slope of the linear fit for the maximum voltage measured as a function of the impact momentum for glass and teflon projectiles.

8.2. Correction of the signal

So far the raw data from sensor A was used to show the basic characteristics of the dependency between impact momentum and maximum voltage. As mentioned at the start of this chapter, the effect of energy dissipation should be considered for a more accurate analysis of the data. In this section the correction of the signal will be described and the results will be used to reduce uncertainty in the estimation of the impact momentum of debris and micrometeoroids.
Impacts act as localised sources of vibration in the plates. As the waves are travelling from the point of impact and through the plate, the amplitude of the vibrations is reduced due to two factors: geometric reduction and dissipation. The first factor refers to the fact that as waves travel further from the source, the wave-front is bigger and bigger leading to a reduction in the amplitude of the waves. The second factor is due to the material absorbing part of the energy of the wave as it travels.
The reduction in wave amplitude with distance can be modelled by Equation 8.1 [58].

$$A = A_0 \frac{e^{\alpha x}}{\sqrt{x}} \tag{8.1}$$

A is the amplitude of the signal, the subscript ”0” refers to the original amplitude which can be assumed as the amplitude at the point of impact. x is the distance travelled by the wave and α is the coefficient of attenuation. The coefficient of attenuation can be found for many engineering materials expressed in $dB/(m \cdot MHz)$. For more complex materials (composites, multi-layer materials and non-isotropic materials) it is usually not available. Finite elements simulations can be employed to determine the coefficient (which usually depends on frequency). The Dispersion Calculator of DLR offers the possibility of calculating curves of attenuation that are more precise than a single coefficient.
To overcome the unavailability of data on the coefficient of absorption for the sandwich panel used in this research, the signal captured by the piezo-sensors was used to experimentally determine the coefficient. Two impacts at the same speed but in different locations were performed, the parameteres needed to determine the attenuation coefficient are listed in Table 8.5. It was found that the coefficient of attenuation is: $\alpha = -0,056cm^{-1}$, calculated as average of the attenuation over the four sensors.

	Experiment 67	Experiment 74
X impact [cm]	36,24	36,24
Y impact [cm]	25,12	28,76
d_A [cm]	30,29	28,09
d_B [cm]	20,44	26,76
d_C [cm]	28,42	28,55
d_D [cm]	36,16	29,80
V_A [V]	0,764	0,888
V_B [V]	1,70	1,08
V_C [V]	0,695	0,689
V_D [V]	0,424	0,760

Table 8.5: Parameters used to determine the attenuation of the signal in the sandwich panel. The point of impact, distance of the point of impact from sensors A, B, C, D and the maximum voltage registered by these sensors are given.

This coefficient was used to correct the maximum voltage detected. This was done for the signal from every sensor: the raw and corrected voltage are given in a table in Appendix B. Once the adjusted voltage was available, for every sensor a linear fit of momentum vs maximum adjusted voltage was performed. This resulted in an estimated momentum based on the measured maximum voltage for every sensors. Averaging over the estimation of the four sensors gives the final estimation of the impact momentum. Once again, this data is given in Appendix B.

8.3. Limits in the detection

Now that a calibration curve that takes into account the data of four sensors and is corrected for the dissipation of vibrational energy, the limits in the detection technology can be studied. By limits the maximum distance at which an impact with a given momentum can be detected is considered. This is the distance at which an impact-induced vibrations result in a voltage that is twice as large as that of the

noise level recorded in the data (0.1 V) or, equivalently, the minimum momentum needed to achieve this voltage at a given distance.
Given a distance of the point of impact from a sensor, the minimum voltage needed can be scaled to find the voltage at the point of imapct and, using the calibration curves, the minimium momentum that a particle should have, as shown in Figure 8.7.

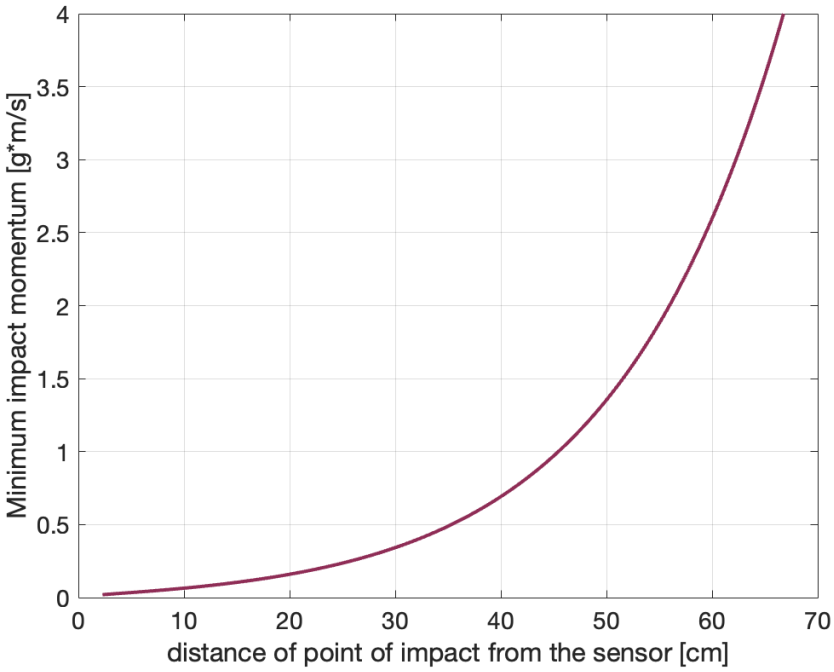

Figure 8.7: Minimum impact momentum for successful detection of the impact for a given distance of the piezo-sensor from the point of contact.

This information can guide the installation of sensors on board satellites. Given the minimum momentum that the researchers want to detect, the location of sensors on the satellite structure can be determined. As momentum is the product of (normal) velocity and mass, for every value there is an infinite combination of mass and speed. Considering the research is focused on small particles at low speed, the speed range considered was from 0 to 200 meters per second, while the mass range was was from 0.02 to 0.2g. The minimum distance for successful detection was calculated for every combination of mass and speed and the results are given in Figure 8.8.

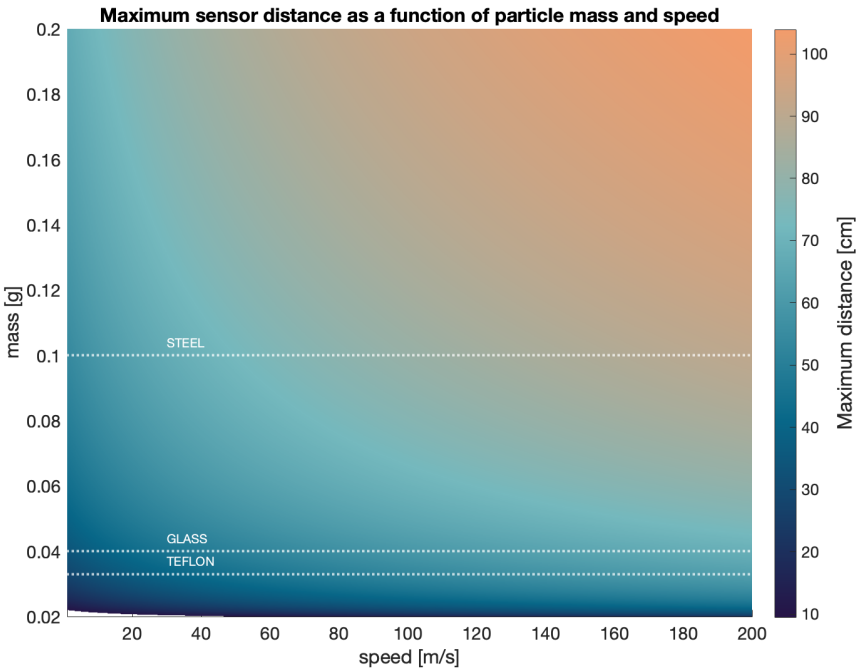

Figure 8.8: Maximum distance of piezo-sensors from the point of impact as a function of the mass and speed of the impacting particle.

9

Experiments on the solar panel

At a later stage in the research a solar panel was found to be used for impact tests. The solar panel is a flight spare model of one of the panels of OTS. The structure of the solar panel consists of a sandwich panel with carbon-fiber skin and aluminium honeycomb core. One one of the sides solar cells are glued with a thin glass coating. The solar panel, a square of roughly 1.5 meters sides wouldn't fit the support structure developed for the aluminium and sandwich panels used in previous experiments. Due to the difference in the mounting of the impact panel and the very different nature of solar panels from structural panels it was decided to dedicate a separate chapter to the analysis of these experiments.
Given the big size of the solar panel a way of placing it on top of the coil of the accelerator had to be found. A movable winch for lifting laboratory equipment was used to hang the solar panel from. This solution allowed to move the solar panel in order to hit different spots and to raise it and lower it to charge the projectiles in the accelerator, inspect the impact damage and assess the results of the experiment. A series of shots with steel and glass beads were performed, with 4 sensors placed on the corners of the solar panel.
The impact of the flyer plate on the stopper plate generates sound waves[1] that travel and hit the solar panel, generating vibrations and thus noise. The fact that the solar panel is not rigidly attached to a stand but is freely hanging means that dampening of these vibrations is very low resulting thus is a substantial amount of noise in the data obtained. The noise reduction strategies already used in the case of the sandwich panel were used. This consisted in adding a layer of soft material (foam) for the flyer plate to impact on. Nonetheless, at higher charging voltages this still resulted in non-negligible noise in the data.

9.1. Frequency content of the signal

As done for all the other experiments the frequency content of the impact was investigated: at first via inspection of the wavelet transform and later by extracting the frequency distribution. As mentioned earlier, the acoustic noise generated during impact of the flyer plate on the stopper plate leads to a big amount of noise in the data recorded. It was observed that, as opposed to the aluminium panel and the sandwich panel, the dissipation of vibrational energy is much stronger and noticeable even at short distances. This means that the further away a sensor is from the coil will lead to a lower amplitude of the noise. At the same time, the further away a sensor is from the coil, the further it is from the point of impact of the projectile (as the point of impact is vertically aligned with the coil) resulting thus in a very attenuated signal from the impact. A compromise had to be found: have a strong enough signal for data processing while limiting the amount of noise. Figure 9.1 shows the position of the sensors on the solar panel and the location of the glass and steel impacts. Sensors A and B are too far from the impact point: despite the impact generating bigger vibration than the acoustic noise of the acceleration process, by the time the waves get to the sensors they are too dampened. This is why for the generation of scalograms and the determination of the frequency distribution of the signal sensors C and D were used. Most of the time sensor C gave the best results.

[1] The fact that this happens, as in the case of the previous setup, is confirmed by the time of arrival of these vibrations that coincides with the expected time of arrival of sound waves travelling at 340 m/s

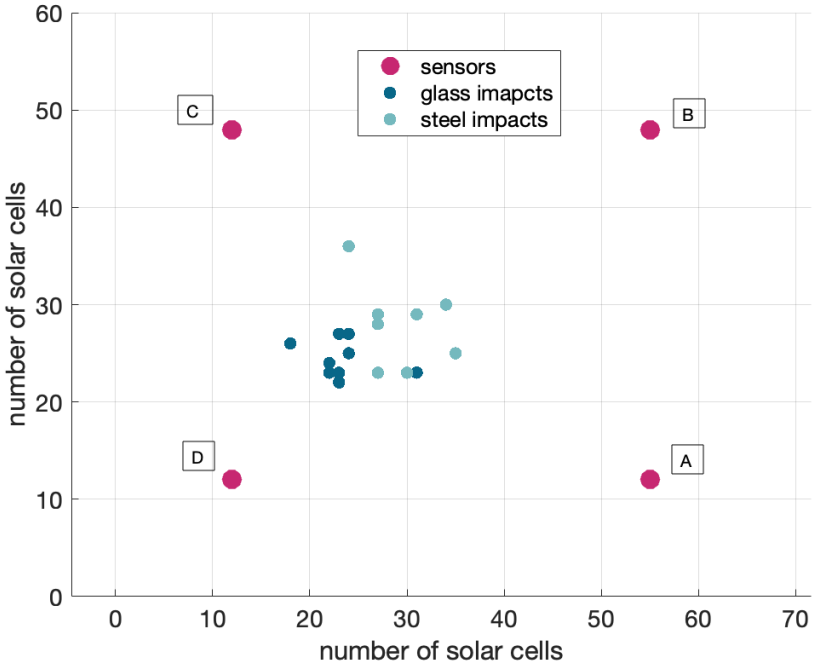

Figure 9.1: Location of impacts on the solar panel and sensor layout for data acquisition.

Looking at the plots in Figure 9.2 both the raw data and the relative scalogram for experiment 15 on the solar panel. After the first peak at 0 seconds, due to the discharge of the capacitor, the oscillations due to the acoustic noise can be seen (at roughly 2 ms). At around 6 ms the vibrations due to the projectile impact can be seen. Comparing the raw data of this plot with that of other experiments (like experiment 29 on aluminium Figure 6.2) shows a much lower frequency of vibrations, confirmed by the scalogram that shows no oscillatory content above 15 kHz.

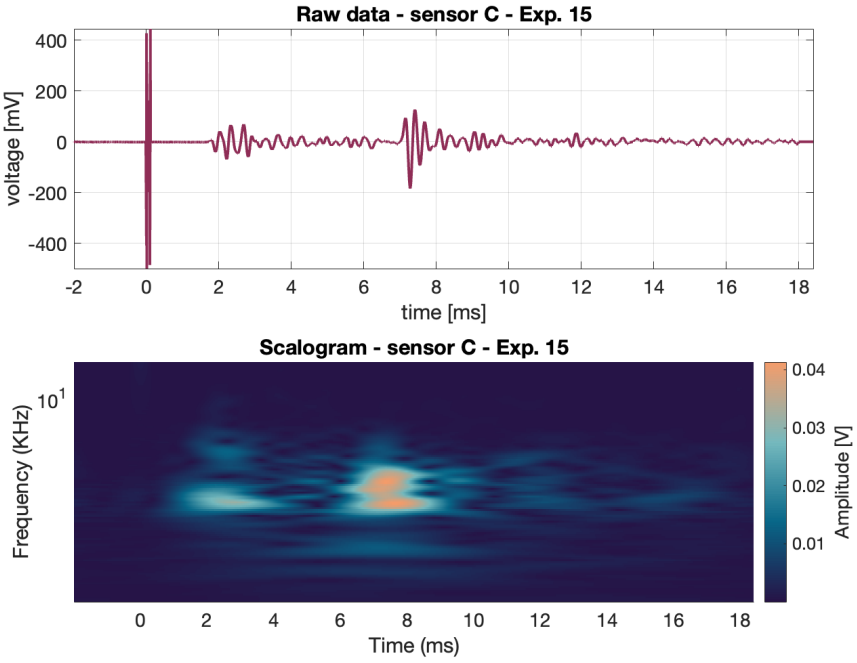

Figure 9.2: Raw data and scalogram for experiment number 15. Target material: solar panel. Projectile: steel bead.

The lower frequency of the vibrations leads to faster data processing due to reduction in computational difficulty of the wavelet transform (keeping the same frequency resolution on a smaller frequency band).

For shots on aluminium and sandwich panel, the data processing was done on part of the signal: from the start of the impact-induced vibrations to the moment the amplitude gets to 20% of the maximum. This was possible due to the high signal to noise ratio. In the case of impacts on the solar panel this method did not succeed. To overcome this the part of the signal containing the impact-induced vibrations was selected by visual inspection and then processed to obtain the frequency distribution.
Selecting the part of the waveform to analyse results in the generation of plots similar to the one in Figure 9.3, where the frequency distribution of the signal shown in Figure 9.2 is shown. It is immediately evident that the frequency of vibration is much lower than for any other target used in this research.

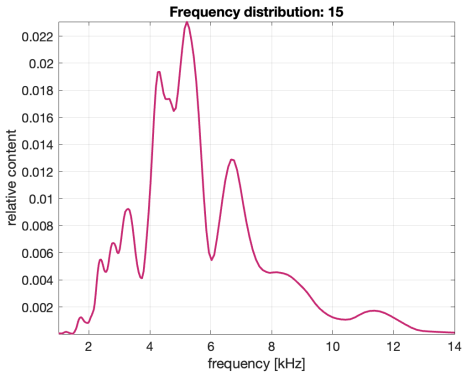

Figure 9.3: frequency distribution for experiment 15. Target material: solar panel. Projectile: steel bead.

The frequency distribution was calculated for every experiment and the results are given in Figure 9.4. The plot, with two colours for the two projectile types, is very chaotic without any clear trend or common behaviour in the curves. As a result further investigation of the behaviour of the frequency distribution.

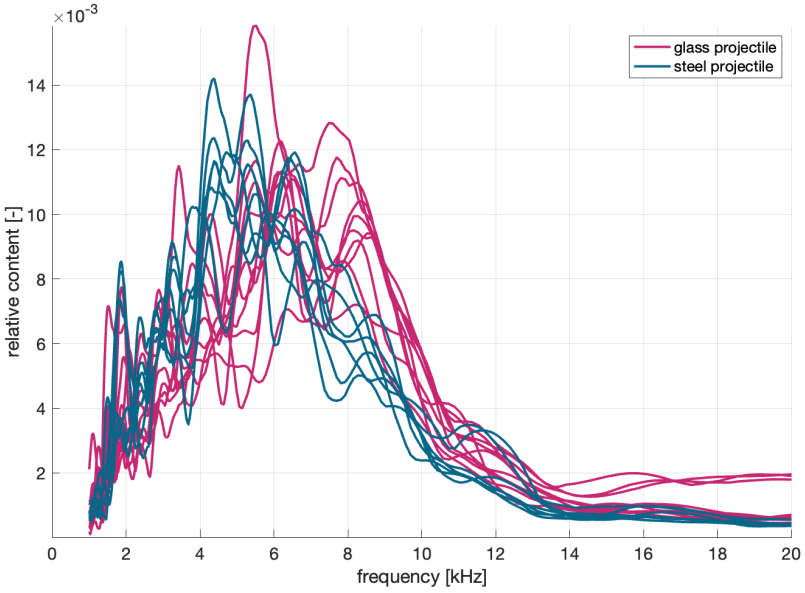

Figure 9.4: frequency distribution for all of the experiments with the solar panel.

Looking at Figure 9.4, it can be seen that at the higher frequencies most curves tend towards zero, except those for three experiments: namely impacts number 2, 3 and 4, all performed with glass. The three shots were performed at different speeds and impacts happened on different parts of the solar cells, with impacts 2 and 4 being on the glass protection of the solar cells and impact 3 in between two cell, as Figure 9.5a shows. The only commonality between the shots is the point of impact: the impacts are in close proximity to each other. Although this may be a reason for having a similar frequency distribution of the vibrations generated, it doesn't explain why other impacts in the same area (Figure 9.5b shows there are many) do not have the same structure in the frequency content of the vibrations generated. The frequency distribution for shots number 2, 3 and 4 is shown in Figure 9.6: not only do the curves match at higher frequencies but they show very similar behaviour in the whole

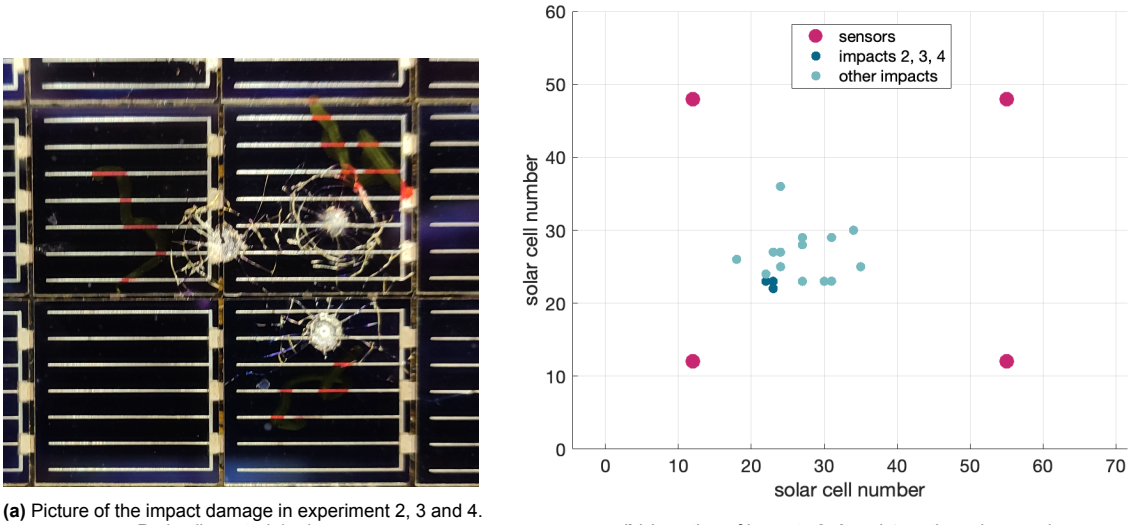

(a) Picture of the impact damage in experiment 2, 3 and 4. Projectile material: glass.

(b) Location of impacts 2, 3 and 4 on the solar panel

Figure 9.5: Location of impacts 2, 3 and 4 on the solar panel

frequency band detected.

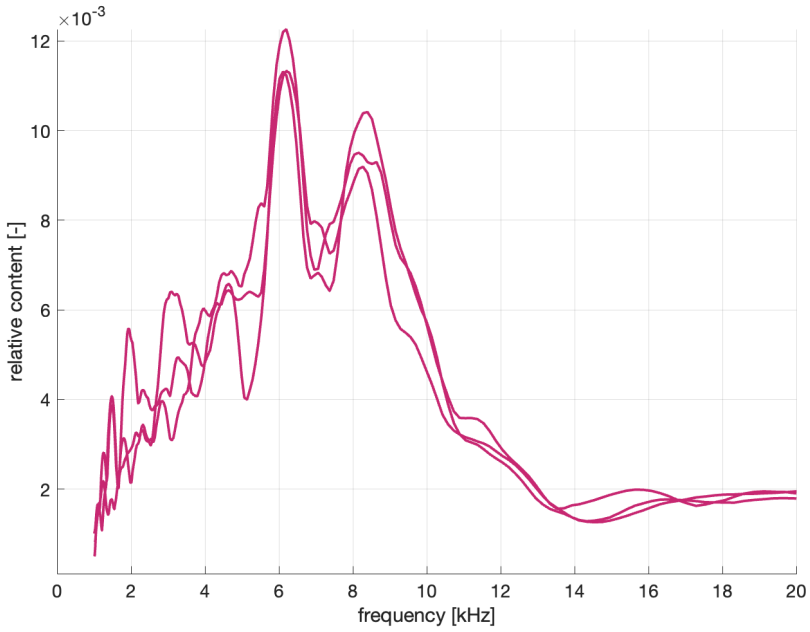

Figure 9.6: frequency distribution for experiment 2, 3, and 4 on the solar panel. Projectile material: glass.

9.2. Effect of impact speed on the signal

As previously done in the case of the aluminium and sandwich panel targets, the effect of speed (i.e. momentum) will be investigated. The target was raised and lowered during experiments, as a result the distance travelled by projectiles was not kept constant for every experiment. The only effect of a change in distance is the effect on the speed of the projectile due to extra deceleration from air drag and gravity. In chapter 5 the strategy for determining the speed of the projectiles is described. In that chapter the model for determination of the calibration curves[2] has been described and compared to the

[2]The calibration curves give the speed of the projectile as a function of the time of flight.

measurements of the high speed camera, showing very good estimation of the speed. If the model is used to determine the change of speed for targets at different heights, results show that the difference in impact speed is negligible. This is why the same curves were used for the determination of impact speed of the projectiles on the solar panel.
The maximum voltage measured and the momentum of the projectile are shown in Figure 9.7. The lower voltage generated upon impact (as compared to impacts on aluminium and honeycomb-sandwich panel) is once again clear. What the figure shows is that no clear trend can be seen in the data. Looking at impacts with glass, increasing the projectile momentum does lead to higher voltages, but it seems like a plateau is reached. Additionally, there is a very clear jump in the maximum voltage, when going from 200 mV to more than 350 mV with a very small change in momentum. For steel, despite the much higher momentum of the impacts (as compared to glass), the voltage generated is much lower than that of glass. Additionally, increasing the impact momentum doesn't necessarily lead to an increase in the maximum voltage detected by the sensors.

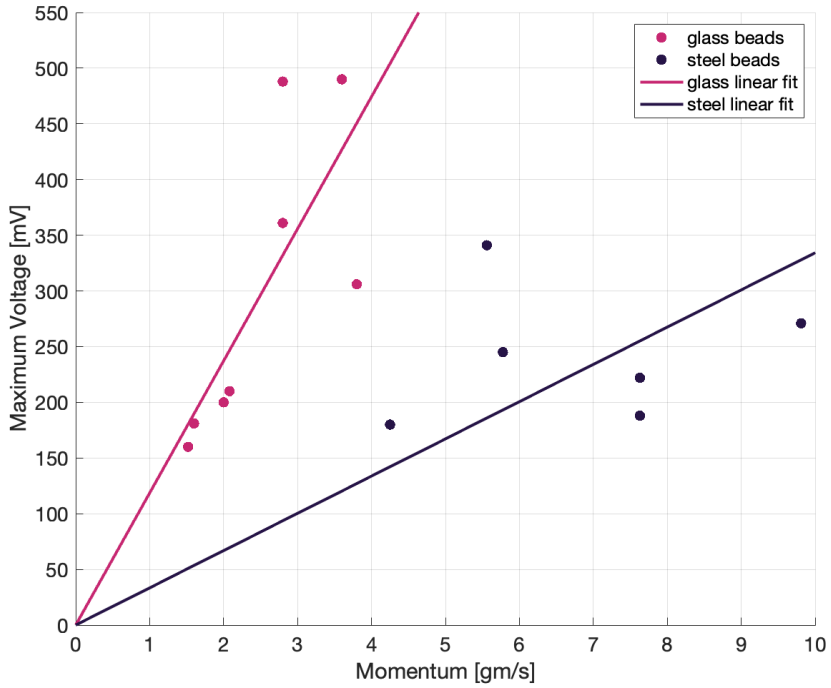

Figure 9.7: Maximum voltage as a function of the impact momentum of the projectiles. Target material: solar panel.

The reason for the sudden jump in voltage was investigated. Impacts at low speeds result in damage to the glass layer on top of the solar cells but no penetration (see Figure 9.5a), while the impacts at a higher momentum resulted in a higher degree of damage with complete destruction of the silicon layer of the solar cell (no destruction of the carbon layer beneath the cell was observed), as seen in Figure 9.8 for shot number 5 and 7. The lower voltage measured during impacts at lower speeds can be the result of the vibration being dampened by the glass-silicon and silicon-carbon interfaces (glues and adhesives). At higher speeds the beads may be interacting directly with the carbon-fiber structure, resulting thus in a higher amplitude of vibrations. The fact that perforating the solar cell until the carbon layer leads to higher amplitudes of vibra-

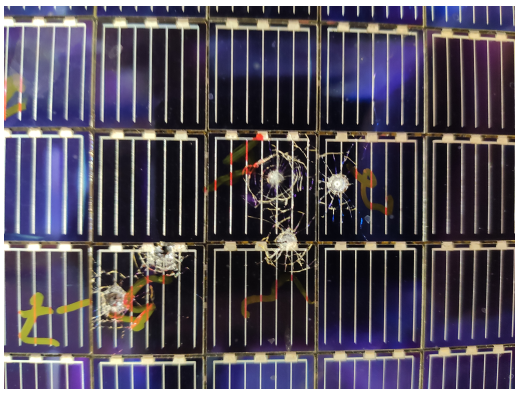

Figure 9.8: Impact damage on the solar panel, the experiment number relative to each shot is indicated.

tion is confirmed by the fact that the two shots with
steel beads with momentum around 5.7 g/ms, resulted in an amplitude of the vibration that sits in between that of low speed glass impacts and high speed glass impacts. Looking at the impact damage of these shots it can be seen how extensive damage has been done to the solar cells, without reaching the carbon layer.

This is visible in Figure 9.9, where impact number 13 is shown. Impacts at higher speeds with steel result in damage both to the cell and to the carbon-fiber structure and led to a lower voltage being measured by the sensors. No impact with steel resulted in perforation of only the solar cell (glass and substrate): either only the glass and part of the silicon layer were perforated, without reaching the carbon-fiber structure, or the cell and the structure were completely perforated.

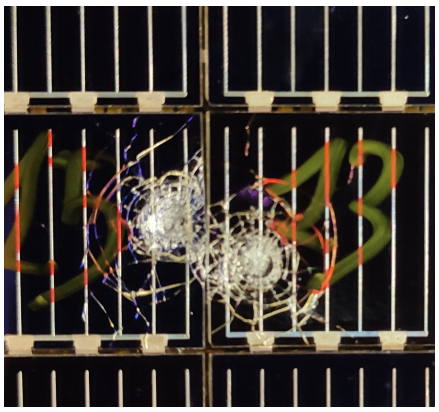

Figure 9.9: Impact damage on the solar panel, the experiment number relative to each shot is indicated.

Experiments seem to indicate a complex vibration generation and propagation mechanism which was to be expected given the composite nature of the solar array: carbon-fiber skin, aluminium honeycomb and solar cells. The amplitude of the vibrations (and thus the voltage detected by the piezo-sensors) is dependent on the momentum (as in the case of the metallic targets previously tested) and on the level of perforation of the solar panel. The degree of damage seems to not depend solely on the momentum of the particle, as impacts with steel beads (with a momentum always higher than that of glass beads) generated in some instances a shallower crater in the solar panel.
Considering the application of the detection technology being investigated in this research, this complexity in the vibrations is a hurdle that needs to be overcome. In a real-life setting only the maximum voltage is available as data and the frequency content of the signal doesn't seem to provide information on the material of the impactor. This would lead to a very high degree of uncertainty in the estimation of the impact momentum.

9.3. Localisation of the impact point

As done previously for the other targets, the waveforms received by each sensor were used to try and determine the point of impact.
The algorithm used was the same and it requires as input the time of arrival of the vibrations at each sensor. For the aluminium and sandwich panel targets the arrival of the extensional mode was used as an indicator of the time of arrival of the vibrations. In the case of experiments on the solar panel the extensional mode was either not present, dissipated too quickly or indistinguishable from the noise generated during shots. To be able to use the algorithm in the same way a different setup should be used, in order to generate data with reduced noise: this would allow for the detection of the extensional mode, if present.
The algorithm was used with a different definition of time of arrival of the vibrations. Instead of using the arrival of the extensional mode, the time of the maximum amplitude was used, this proved unsuccessful and didn't lead to the algorithm converging. A second method was considered: the time the signal exceeds the noise by a given factor was used. The issue with this method is that the factor used is not constant: it has to be manually adjusted for every sensors and for every experiment. This strategy also proved unsuccessful.
Localising the impact using the time of arrival of the vibration waves proved unsuccessful. It can not be concluded that this is a consequence of the algorithm not being adequate or the uncertainty in estimating the time of arrival of the waves. Further research is needed to draw more solid conclusions.

10

Conclusion

Space debris and micrometeoroid impacts on spacecraft structures were simulated in a laboratory environment with the objective of studying the feasibility of an Acoustic Emission (AE) based Space Debris and Micrometeoroid (SDMM) detector. Projectiles of different material (glass, teflon and stainless steel) were accelerated using an electromagnetic accelerator to achieve impact speeds ranging from 10 m/s to 200 m/s. The projectiles impacted a target plate representing the structure of a spacecraft: a 3mm aluminium panel, a 5mm aluminium skin honeycomb sandwich panel and a flight spare model of a solar panel were used for testing. The target plate was equipped with piezo-sensors connected to a data acquisition system with a sampling rate more than double the Nyquist frequency as calculated from the resonant frequency of the sensors.

An algorithm that can estimate the impact location was developed. The algorithm takes as input the time of arrival of the extensional mode of vibration generated upon impact and outputs, in addition to the impact coordinates the time of impact and the speed of sound in the plate. The algorithm provides accurate estimation of the point of impact, with errors equal or lower than those found in literature. This is due to better identification of the time of arrival of the vibrations done by using the the extensional mode to determine the arrival time of the waves to be used as input to the algorithm, as opposed to the time at which the signal exceeds a given threshold. Only in the case of the impacts of the solar panel the impossibility to observe the extensional mode lead to the algorithm not being able to converge. Initial steps in the development of a fully autonomous algorithm were taken to overcome the need of manual identification of the time of arrival of vibrations. This is based on the identification of a time-window in which the extensional mode is contained via a Butterworth band-pass filter, the part contained in this time-window is then processed using the Wigner-Ville trasnform. This transform gives a high-resolution output of the frequency content of the signal over time that allows for a precise identification of the time of arrival of the vibrations.

The signal detected by sensors is a time-varying signal that was processed using the continuous-wavelet transform function of MATLAB: the complex nature of the signal makes tools such as a Fourier transform inadequate a they can't capture the evolution of the signal over time. This allows for the identification of the frequency components of the signal. Extracting the energy content of the signal shows that projectiles of different material generate vibrations that differ in the energy carried by each frequency. This is a promising result in using solely impact-vibrations to extract information on the material class of the impactor. The classification of the material class based on the frequency content of the generated signal was more successful with impacts on aluminium as opposed to the aluminium-skin sandwich panel or the solar panel. The big difference in the two was the amount of plasticity of the target: the less plastic effects the wider the frequency spectrum of the signal and thus the easier classification of the material. For this reason more rigid parts of a spacecraft are better suited for the SDMM detection method under investigation: this includes protective skins (Whipple shield) on the ISS. Solar arrays, due to the diverse set of materials present, present complex vibrational mechanics phenomena due to the difference components of the solar panel that can be impacted: the solar cell, the adhesive layer or the support structure. This means that not only the projectile material but also the impact location plays a role in the waveform generated.

Efforts were spent in determining if estimation of the momentum of the impactor is possible simply by

analysis of the vibrations. The maximum voltage detected by the sensors was used as an indicator of the energy transferred from the projectile to the plate. In the case of impacts on the sandwich panel, the maximum voltage detected is strongly correlated with the impact momentum. In particular, the maximum voltage is very similar in the case of glass and teflon beads with similar momentum. This is an important result as in a real life application of the detector, the material of the impactor is not known. The fact that the maximum voltage does not strongly depend on the material of the projectile is thus beneficial. In the case of impacts on the solar panel only a weak correlation was found between impact momentum and the maximum voltage measured: the solar panel has multiple layers and additionally, having a structure made of carbon fiber, leads to non-plastic phenomena during impact and as a consequence complex damage mechanics. Despite this it has to be noted that the biggest source of noise in the experiments was due to the acceleration of particles: this will be absent in space so it is possible that even very small particles could be detected with sensors placed on solar arrays.
This thesis was an initial research into the possibility of using acoustic emissions as a means to detect debris and micrometeoroids. Promising results were obtained with impact location, time, material rigidity and momentum upon impact being among the parameters that can be estimated. Further research is needed to improve on the many aspects that make up the detector: sensor location, mechanical coupling of sensor and structure and data processing among others. But this is a good first step in a simple and scalable approach to characterise the yet unknown environment made up by small objects around our planet.

10.1. Answer to the research questions

In this section the conclusions will be written as explicit answers to the research questions proposed at the start of the research.

What does the waveform of impact-generated vibrations look like?
The waveform acquired by the piezo-sensors is a time-varying signal. The signal generated by impacts on the aluminium plate and the aluminium-skin sandwich plate shows to distinct component of the vibration: the extensional mode (travelling at higher speed) and the flexural mode. The flexural mode exhibits frequency dispersion, due to higher frequency waves travelling at a higher speed, as described in section 2.5.

Which sensors should be used to pick up vibrations in a spacecraft?
Vibration sensors that are small in size should be preferred, to make the assumption of localised detection of vibrations more sound. It was observed that the signal generated by different projectiles have more noticeable differences at higher frequencies: this is why sensors with a higher resonant frequency should be preferred. Despite higher resonant frequencies being preferred, the most important vibrations modes are the zero-modes of the plate. Higher modes (that are generated at higher frequencies) are usually very small in amplitude making them less useful from a signal-to-noise ratio perspective [61] [62]. Additionally, satellites are equipped with vibration sensors used for pre-launch testing. These sensors are not removed before launch and can thus be reused for detection of vibrations in space.

How can impacts on a spacecraft be simulated in a laboratory environment?
Impacts in a laboratory environment can be simulated in a number of ways. Given the objective of this research to investigate impacts at low speeds, an electromagnetic accelerator was chosen due to its simplicity, ease of use and time to prepare for experiments. The accelerator can shoot projectiles up to speeds of 150 m/s. The method of acceleration is not strongly influenced by the mass of the projectiles, allowing high-speed impacts also with heavy projectiles.

Which data processing techniques can be used to extract data from the sensor signal
Given the time-varying nature of the signal acquired by the sensors, time-frequency methods should be employed to properly analysed the complexities of the waveform. The wavelet transform was chosen

as the primary data processing tool, that served as input for further processing and analysis.

Which information on the impactor can be obtained from the waveforms?
In the case of the the aluminium plate and the aluminium skin honeycomb sandwich the point of impact can be estimated with centimetre precision. For both plates, the analysis of the frequency content of the signal seems to suggest that different materials generate waves at different frequencies. Additionally, in the case of the sandwich panel, the momentum of the impacting particle can be estimated as it was found to be linearly proportional to the maximum voltage picked up by the sensors. In the case of the solar panel, the noise in the data reduced the amount of information that can be derived about the impactor. The absence of the extensional mode in the data doesn't allow for precise determination of the time of arrival of the vibrations. The complexity of the solar panel in terms of materials used and, as a consequence materials that make contact with the projectiles, results in vibrations that not only depend on the speed, mass and material of the projectile but also on the point of impact. The rigidity and the other material properties of the point of impact have a big influence on the amplitude and frequency of the generated vibrations. This results in the impossibility of determining the momentum of the impacting object and its material class. The dependence of voltage from the impact momentum together with the experimentally calculated coefficient of vibration dissipation for the sandwich panel of -0.05 cm^{-1} was used to determine the maximum distance of sensors from the point of impact as a function of particle speed and mass for successful detection of the impact. Particles as light as 0.03 g (the lightest used in the experiments) travelling at speeds as low as 15 m/s are expected to be detectable from sensors as far as 50cm, while for objects of 0.2 g travelling at speeds exceeding 200 m/s it is expected that a sensor can be as far as 1 meter away from the point of impact.

Are there better suited materials or locations for such an application?
From the experiments, homogeneous parts of the satellite with isotropic properties reduce the dependence of the vibration modes from the point of impact: this makes the influence of projectile material and mass more visible in the data. Additionally, the simpler the structure where the sensors will be placed, the simpler the vibration phenomena taking place. Additionally, the rigidity of the structural materials should be considered. As discussed in subsection 4.2.5, deformation and plasticity phenomena reduce the frequency of vibration of the target: this is why limiting the deformation to the impactor as much as possible can help in characterising the material class of the debris or micrometeoroid based on the frequency content of the signal. Whipple shields, for example, are a possible part of a spacecraft suited for the application of the detection technology under investigation in this master thesis.

Can the impact location be estimated?
Using at least 4 sensors, the point of impact can be estimated with cm-level accuracy. The algorithm for the estimation of the point of impact is based on the time of arrival of the vibrations to the sensors: for accurate estimation the time of arrival of the extensional mode should be identified. For a small number of impacts this can be done by visual inspection while in the case of bigger amounts of data an automated process should be used. A first automated algorithm was developed: the algorithm performs a Wagner-Wille transform of part of the signal to determine the time of arrival of the extensional mode.

11

Reccomendations and future work

The work done in this MSc thesis was an initial step into the study of a novel detection method for space debris and micrometeoroids. Many topics have been investigated, from sensor placement to multilateration algorithms to frequency analysis and they can all be expanded with further research and experiments.

11.1. Effect of Mass and Speed

In this research thesis the effect of momentum was investigated and it was observed that the maximum voltage detected grows linearly with the momentum of the impacting momentum. Nonetheless, momentum is the combined effect of mass and speed. Most space debris catalogues and environmental models use mass as one of the defining parameters of the debris. Further research can be made to determine whether it is possible to separate the effect of mass and speed on the signal.

11.2. Sensors and sensor placement

The type of sensors used was chosen based on two main features: ease of use and frequency band. In real life, space-worthy sensors should be used and considering that during spacecraft testing accelerometers are already installed on the structures they could be reused to reduce cost and complexity. When it comes to the placement of sensors, reusing accelerometers wouldn't give too much freedom but if new sensors are to be added a study on the optimal placement coud be carried out, with optimal being, for example, the lowest number needed or the location for best detection performance. Additionally, the code developed to assess the sensitivity of detection based on sensor location can be expanded to account for non - isotropic materials or spacecraft parts with discontinuities (like joints, glued parts...)

11.3. Impact speed

In literature there is a relatively high amount of information on hypervelocity impacts and low velocity impacts (the object of the current thesis), investigating the performance of the detection technique being developed at the transition speeds could not only be beneficial to the detection of debris and micrometeoroids but also to material science and structural engineering in general. When impact energies start increasing many materials experience deformation in the plastic regime (this was already observed for PTFE), this has an effect on the waveform measured by the sensors and could impact the data processing techniques developed for lower velocity regimes.

11.4. Material used

The target material used was aluminium and honeycomb structure, both material that present symmetry and thus quasi-uniform properties when it comes to propagation speed of vibrations. Non-isotropic materials can be used, for example carbon-fiber based plates or more complex structures made of

multiple materials that more closely represent a spacecraft, like a plate covered with MLI or an antenna. The solar panel used for testing is a good example of a target that matches real space hardware, a target that sits in between the very simple metal plates and the complex solar panel might be used.
When it comes to the projectiles used only materials representative of space debris were used. This choice was made for reproducibility reasons. Now that the detection technology is better understood and seems promising, analogue micrometeoroids and dust can be tested, in addition to more man-made materials of different shapes and sizes.

11.5. Data processing

Determining the arrival time of the extensisional mode of vibration (that was chosen as the input time for the location detection algorithm) was not an easy task. This was in part due to the experimental setup itself and the vibrations generated by the acceleration of the projectiles. Better data processing techniques can be developed to automate the identification of the arrival of the extensional mode, ideally applicable to impacts from any type of projectile and easily adaptable to different impact characteristics. Using wavelet decomposition seems promising as CPU time is low and a lot of information can be seen in the transform. Studying the energy content showed promising results for distinguishing different types of materials from the vibrations generated. The algorithm used can be improved to reduce noise and the variability within a single class of materials to make the identification faster and more accurate.

11.6. Setup

Given the working principle of the accelerator, any shot performed also generated sound waves due to the impact of the flyer plate on the stopper plate that resulted in noise picked up by the sensors. Low in magnitude in the case of aluminium, the noise during impacts on the sandwich panel and the solar panel was not negligible making data processing more challenging.
Solutions can be found to mitigate this problem. Adding a layer of foam proved to be a simple yet effective solution, with the only downside or requiring replacement every 4 to 5 shots due to wear. Another option, more complex, would also open up more possibilities in terms of research. Despite the accelerator taking up significant space, the only parts that do accelerate the projectile are relatively small: a coil and the cable connecting it to the energy storage part of the setup. The coil, together with the stopper plate and the target can thus be placed inside a vacuum chamber. This can have two major advantages: elimination of sound waves creating noise in the data and possibility to use high area to mass ratio projectiles. For projectiles with a low density, or very small in size, the effect of drag is so high that the particles don't even hit the target. Performing the experiments in a vacuum chamber would allow to study the detection capabilities for impactors like paint flocks, (analogue) space dust, MLI pieces and so on.

11.7. Penetration impacts: diameter

The algorithm developed, relying on a least-squares approach to estimate the point of impact of the projectile, as part of the process estimates the impact time and speed of sound in the medium too. This speed doesn't necessarily have to equal the real speed of sound in the plate: errors in measurement of the arrival time of the extensional mode of vibration can lead to the estimated speed being higher or lower than the real one.
The experiments performed simulated debris and micrometeoroid impacts with projectiles of at most a diameter of 3mm which allowed for the hypothesis of point-like impact location. In a real-life scenario impacts due to bigger objects are possible, even without penetration, like on the solar array of Sentinel 1A in 2016 [63]. Bigger impactors could have different contact-mechanics phenomena taking place during impact that lead to different waveforms being generated and thus picked up by the sensors: all these effects can be analysed in future studies. Additionally, piezo-sensors can act both as passive sensors or as active vibration generating devices: this can be exploited with SHM tools to estimate the size of the impact crater.

11.8. Simulations and model validation

This research was completely experimental: testing all the possible combination of impactor and target that in a real life situation can happen is a long and costly endeavour. Models can be developed to simulate impacts and the response of the material after an impact, in particular the amplitude of the vibrations (and thus voltage detected by the sensors) should be investigated. The experiments performed (and further experiments) can be used to validate the models and make sure that they accurately represent reality.

References

[1] ESA. *ESA's Space Environment Report 2021*. URL: https://www.esa.int/Safety_Security/Space_Debris/ESA_s_Space_Environment_Report_2021 (visited on 04/12/2022).

[2] ESA. *Scanning and Observing*. URL: https://www.esa.int/Safety_Security/Space_Debris/Scanning_and_observing2 (visited on 04/07/2022).

[3] Gerhard Drolshagen. "Impact effects from small size meteoroids and space debris". In: *Advances in space Research* 41.7 (2008), pp. 1123–1131.

[4] ESA. *About Space Debris*. URL: https://www.esa.int/Safety_Security/Space_Debris/About_space_debris (visited on 04/12/2022).

[5] Stephen A Schwartz et al. *Space program: Space debris a potential threat to Space Station and shuttle*. Tech. rep. 1990.

[6] Robin Biesbroek et al. "The clearspace-1 mission: Esa and clearspace team up to remove debris". In: *Proc. 8th Eur. Conf. Sp. Debris*. 2021, pp. 1–3.

[7] J-C Liou. "Risks from orbital debris and space situational awareness". In: *IAA Conference on Space Situational Awareness (ICSSA)*. JSC-E-DAA-TN76975. 2020.

[8] TS Kelso et al. "Analysis of the Iridium 33-Cosmos 2251 collision". In: *Advances in the Astronautical Sciences* 135.2 (2009), pp. 1099–1112.

[9] ESA. *ESA & UNOOSA space debris infographics and podcast*. URL: https://www.esa.int/Safety_Security/Space_Debris/ESA_UNOOSA_space_debris_infographics_and_podcast (visited on 04/12/2022).

[10] National Research Council et al. *Orbital debris: A technical assessment*. National Academies Press, 1995.

[11] Giovanni Domenico Cassini. "Découverte de la lumière celeste qui paroist dans le zodiaque". In: *Academie Royale de Sciences* (1685).

[12] Arthur W. Wright. "III. On the polarization of the zodiacal light". In: *The London, Edinburgh, and Dublin Philosophical Magazine and Journal of Science* 48.315 (1874), pp. 13–21. DOI: 10.1080/14786447408641068.

[13] MS Hanner et al. "Zodiacal light and the asteroid belt: The view from Pioneer 10". In: *Journal of Geophysical Research* 79.25 (1974), pp. 3671–3675.

[14] AoL Baker et al. "The imaging photopolarimeter experiment on Pioneer 11". In: *Science* 188.4187 (1975), pp. 468–472.

[15] Joseph A Burns, Philippe L Lamy, and Steven Soter. "Radiation forces on small particles in the solar system". In: *Icarus* 40.1 (1979), pp. 1–48.

[16] J Klačka et al. "The Poynting–Robertson effect: A critical perspective". In: *Icarus* 232 (2014), pp. 249–262.

[17] JS Dohnanyi. "Particle dynamics." In: *Cosmic Dust* (1978), pp. 527–605.

[18] DE Brownlee and RS Rajan. "Micrometeorite craters discovered on chondrule-like objects from Kapoeta meteorite". In: *Science* 182.4119 (1973), pp. 1341–1344.

[19] Fred L Whipple. "56. On Maintaining the Meteoritic Complex". In: 15. Scientific, Technical Information Division, National Aeronautics, and Space Administaration, 1967, p. 409.

[20] George W Wetherill. "Solar system sources of meteorites and large meteoroids". In: *Annual Review of Earth and Planetary Sciences* 2.1 (1974), pp. 303–331.

[21] Martin Harwit. "Origins of the zodiacal dust cloud". In: *Journal of Geophysical Research* 68.8 (1963), pp. 2171–2180.

[22] CH Leinert, S Roser, and J Buitrago. “How to maintain the spatial distribution of interplanetary dust”. In: *Astronomy and Astrophysics* 118 (1983), pp. 345–357.

[23] Heiner Klinkrad. *Space debris: models and risk analysis*. Springer Science & Business Media, 2006.

[24] NASA. *EUROPA CLIPPER*. URL: https://europa.nasa.gov/ (visited on 04/08/2022).

[25] Sascha Kempf, Ralf Srama, and Amara Graps. *The Cosmic Dust Analyser Data Handbook*. 2012.

[26] S Kempf et al. “SUDA: A Dust Mass Spectrometer for compositional surface mapping for the JUICE mission to the Galilean moons”. In: *AGU Fall Meeting Abstracts*. Vol. 2012. 2012, P51A–2015.

[27] Robert D Corsaro et al. “Characterization of space dust using acoustic impact detection”. In: *The Journal of the Acoustical Society of America* 140.2 (2016), pp. 1429–1438.

[28] Luigi Colangeli et al. “GIADA: the grain impact analyser and dust accumulator for the Rosetta space mission”. In: *Advances in Space Research* 39.3 (2007), pp. 446–450.

[29] F Esposito et al. “Physical aspect of an “impact sensor” for the detection of cometary dust momentum onboard the “Rosetta” space mission”. In: *Advances in Space Research* 29.8 (2002), pp. 1159–1163.

[30] NASA. *Long Duration Exposure Facility (LDEF)*. 2000. URL: https://curator.jsc.nasa.gov/mic/ldef/index.cfm (visited on 03/15/2022).

[31] Eberhard Grün et al. “Collisional balance of the meteoritic complex”. In: *Icarus* 62.2 (1985), pp. 244–272.

[32] Heiner Klinkrad et al. “An introduction to the 1997 ESA MASTER Model”. In: *EUROPEAN SPACE AGENCY-PUBLICATIONS-ESA SP* 393 (1997), pp. 217–224.

[33] PH Krisko et al. “ORDEM 3.0 and MASTER-2009 modeled debris population comparison”. In: *Acta Astronautica* 113 (2015), pp. 204–211.

[34] Shinya Fukushige et al. “Comparison of debris environment models; ORDEM2000, MASTER2001 and MASTER2005”. In: *IHI engineering review* 40.1 (2007), p. 31.

[35] André Horstmann et al. “flux comparison of master-8 and ordem 3.1 modelled space debris population”. In: *8th European Conference on Space Debris*. 2021.

[36] Karim Aly and Philip D. Bradford. “Real-time impact damage sensing and localization in composites through embedded aligned carbon nanotube sheets”. In: *Composites Part B: Engineering* 162 (2019), pp. 522–531. ISSN: 1359-8368. DOI: https://doi.org/10.1016/j.compositesb.2018.12.104. URL: https://www.sciencedirect.com/science/article/pii/S1359836818314963.

[37] Byeong-Wook Jang and Chun-Gon Kim. “Real-time detection of low-velocity impact-induced delamination onset in composite laminates for efficient management of structural health”. In: *Composites Part B: Engineering* 123 (2017), pp. 124–135. ISSN: 1359-8368. DOI: https://doi.org/10.1016/j.compositesb.2017.05.019. URL: https://www.sciencedirect.com/science/article/pii/S1359836817310016.

[38] W Lance Richards et al. “NASA applications of structural health monitoring technology”. In: *International Workshop on Structural Health Monitoring*. DFRC-E-DAA-TN11102. 2013.

[39] JM Nelson and BM Lempriere. *Space station integrated wall design and penetration damage control. Task 4: Impact detection/location system*. Tech. rep. 1987.

[40] William H Prosser, Michael R Gorman, and Donald H Humes. “Acoustic emission signals in thin plates produced by impact damage”. In: *Journal of Acoustic emission* 17.1-2 (1999).

[41] Frank Schäfer and Rolf Janovsky. “Impact sensor network for detection of hypervelocity impacts on spacecraft”. In: *Acta Astronautica* 61.10 (2007), pp. 901–911.

[42] Zhidong Liu and Baojun Pang. “A method based on acoustic emission for locating debris cloud impact”. In: *Fourth International Conference on Experimental Mechanics*. Vol. 7522. SPIE. 2010, pp. 246–251.

[43] Lu Cheng et al. “Acoustic emission source location using Lamb wave propagation simulation and artificial neural network for I-shaped steel girder”. In: *Construction and Building Materials* 273 (2021), p. 121706.

[44] Guy Spencer et al. “Design and initial calibration of micrometeoroid/space debris detector (MDD)”. In: *4th European Conference on Space Debris*. Vol. 587. 2005, p. 227.

[45] Herbert Überall. “Surface waves in acoustics”. In: *Physical acoustics*. Vol. 10. Elsevier, 1973, pp. 1–60.

[46] Arthur W Leissa. *Vibration of plates*. Vol. 160. Scientific and Technical Information Division, National Aeronautics and …, 1969.

[47] A. Huber - DLR. *The Dispersion Calculator: An open source software for calculating dispersion curves and mode shapes of guided waves*. 2000. URL: `https://www.dlr.de/zlp/en/desktopdefault.aspx/tabid-14332/24874_read-61142/` (visited on 12/14/2022).

[48] Ho Tro Mi and Detlef Koschny. *The Set Up of a LRT Electrornognetic Accelerotor at ESTEC*. European Space Agency. Spoce Science Deportment, ESTEC/ESA, Keplerlaan 1, NL-2201 AG Noordwijk AZ, 2000.

[49] P Lell, E Igenbergs, and H Kuczera. “An electromagnetic accelerator”. In: *Journal of Physics E: Scientific Instruments* 16.4 (1983), p. 325.

[50] Andrew J Piekutowski et al. “Performance of Whipple shields at impact velocities above 9 km/s”. In: *International Journal of Impact Engineering* 38.6 (2011), pp. 495–503.

[51] Anand Pai et al. “Advances in the Whipple shield design and development: A brief review”. In: *Journal of Dynamic Behavior of Materials* (2022), pp. 1–19.

[52] Adhemar Bultheel. “Learning to swim in a sea of wavelets”. In: *Bulletin of the Belgian Mathematical society-simon stevin* 2.1 (1995), pp. 1–45.

[53] SP Ying, DR Hamlin, and D Tanneberger. “A multichannel acoustic emission monitoring system with simultaneous multiple event data analyses”. In: *The Journal of the Acoustical Society of America* 55.2 (1974), pp. 350–356.

[54] Richard B Langley et al. “Dilution of precision”. In: *GPS world* 10.5 (1999), pp. 52–59.

[55] Hamid Ghaednia et al. “A review of elastic–plastic contact mechanics”. In: *Applied Mechanics Reviews* 69.6 (2017).

[56] Amelie Kolopp et al. “Modeling impact on aluminium sandwich including velocity effects in honeycomb core”. In: *Journal of Sandwich Structures & Materials* 15.6 (2013), pp. 733–757.

[57] Guangyong Sun et al. “High-velocity impact behaviour of aluminium honeycomb sandwich panels with different structural configurations”. In: *International Journal of Impact Engineering* 122 (2018), pp. 119–136.

[58] Kanji Ono. “Experimental Determination of Lamb-Wave Attenuation Coefficients”. In: *Applied Sciences* 12.13 (2022), p. 6735.

[59] JM Sibeaud, C Prieur, and C Puillet. “Hypervelocity impact on honeycomb target structures: experimental part”. In: *The 4th European Conference on Space Debris. Darmstadt, Germany: The European Space Agency*. 2005.

[60] Alessandro Francesconi et al. “Generation of transient vibrations on aluminum honeycomb sandwich panels subjected to hypervelocity impacts”. In: *International Journal of Impact Engineering* 35.12 (2008), pp. 1503–1509.

[61] DC Worlton. *Ultrasonic testing with Lamb waves*. Tech. rep. General Electric Co., Hanford Atomic Products Operation, Richland, Wash., 1956.

[62] Viktorov IA. “Rayleigh and Lamb waves: physical theory and applications”. In: *Moscow: Acoustics Institute, Academy of Science of the USSR* (1967).

[63] H Krag et al. “A 1 cm space debris impact onto the sentinel-1a solar array”. In: *Acta Astronautica* 137 (2017), pp. 434–443.

A

Operation of the electromagnetic accelerator

This appendix serves the purpose of describing how to operate the accelerator, some tips on its use and some suggestions for resolving typical issues encountered during its operation. The strategy for operating the accelerator has been derived from the manual [48], where more information on use and functioning can be found. Figure A.1 shows a picture of the accelerator control panel with the buttons needed for its use. Note that the triggering button to trigger shots has been disconnected due to malfunction and unavailability of a spare part due to the old age of the device. Shots can be triggered externally by using the BNC connector on the control panel of the accelerator. It is sufficient to connect a device that can close the circuit between the inner and outer parts of the coax cable.

A.1. Operating the accelerator

Below the steps needed to operate the accelerator are listed.

- Connect the accelerator to a power source and make sure that all the metallic parts of the casing are grounded. It is possible to use the grounding probe attached to the accelerator for this.
- set the voltage charging knob to 0 (in case it was not). This should result in the accelerator turning on.
- It is now possible to proceed with charging the accelerator. Manual charging has been used as it resulted in less issues as compared to manual charging. For automatic charging the manual [48] shows the step needed to perform a shot. To charge the accelerator manually make sure that the button ”Lade-automatik” (top right of the control panel) is off, if it’s on, press it.
- Press the button ”start” in the top right of the control panel to start the capacitor charging procedure.
- Turn the charging voltage dial. The maximum is 66%, for lower voltages any value will work, with higher values requiring less time to reach the desired voltage. For very high voltages (above 10 kV), at least 50% is needed to reach the desired voltage.
- When the desired voltage is reached (as seen on the voltage indicator) press the ”stop” button.
- Trigger the shot via the external trigger.

A.2. Tips for accelerator use

- Before setting up the data acquisition system it is suggested to charge the capacitor and leave only triggering the shot as step in the operation of the accelerator. Turning on the accelerator, charging the capacitor and stopping the charging generate strong EM fields that tend to trigger data acquisition systems or show false data readings. By turning on the systems after the charging is complete this is avoided.

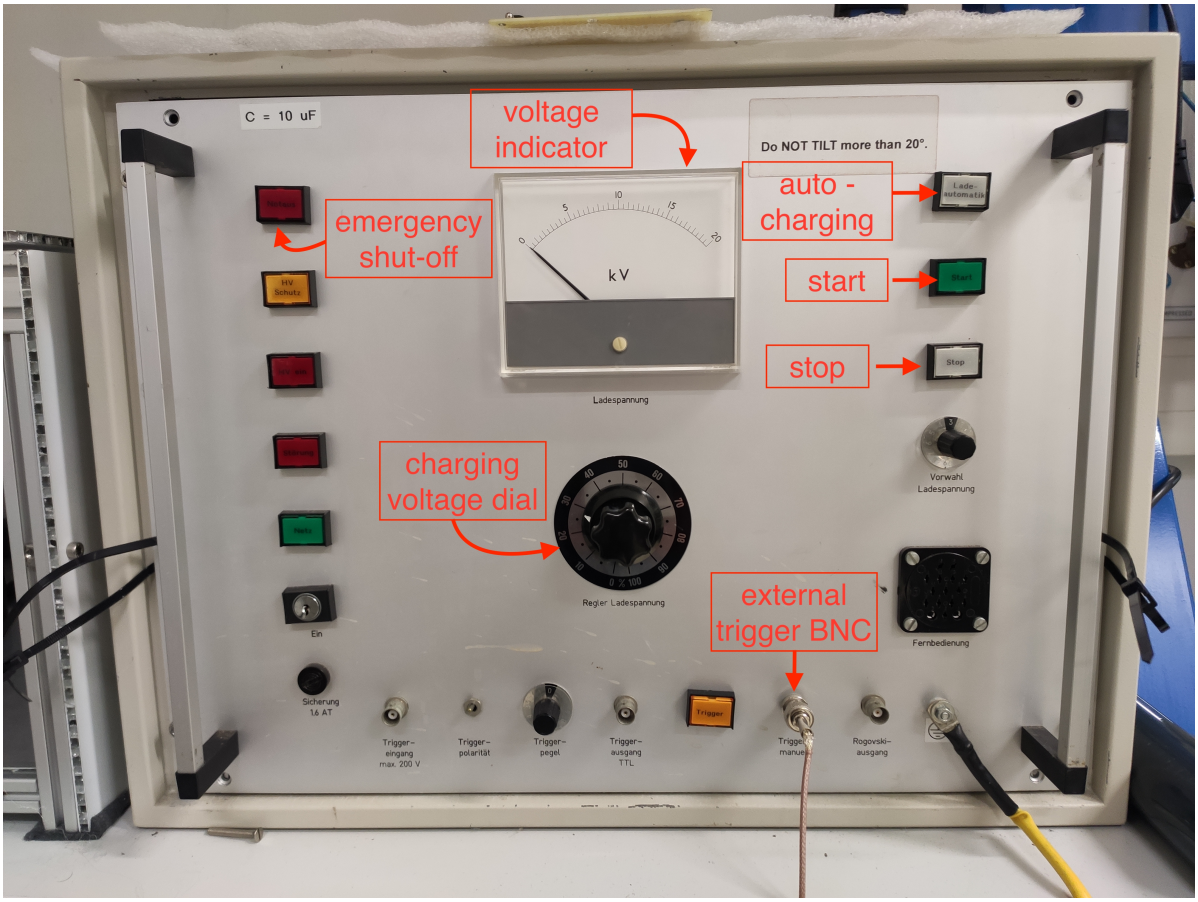

Figure A.1: Picture showing the various buttons on the control panel of the accelerator.

- Due to use of the accelerator the base for the flyer plate has developed a bulge that results in a tilt of the flyer plate resting on it. To compensate for this an o-ring has been added to put the flyer plate on. Any other non-conductive object can be used.

A.3. Solution to common issues with the accelerator

- **Sound of a spark and no shot happening**: multiple times it happened that the accelerator would stop working and, when a shot was triggered, an arching sound could be heard. This could be the result of a real electric-arc and can be thus solved by cleaning the inside with compressed air to remove any possible foreign object (like dust) that can generate sparks. The sound can also be the result of high voltage connections in the back of the machine getting loose and thus not allowing high intensity current to flow. Lastly this can be the result of the ignitron not working properly due to erosion of the electrode that should generate plasma. To compensate this it is possible to tilt the accelerator, a line has been drawn on the front of the accelerator to show the new horizontal.
- **high amount of noise in the data**: The impact of the flyer plate on the stopper plate generates a big amount of vibrations, both in the structure and indirectly via the sound waves emanating from it. Depending on the setup, these can lead to signals that are not the result of projectile impacts making data processing harder. Performing experiments in a vacuum can reduce the effect of sound waves generated upon contact of the flyer plate and stopper plate. Additionally a layer of foam or any other shock-absorbing material can be added under the stopper plate, as long as it does not close the hole for the projectile to go through. Finally, good mechanical isolation of the coil and stopper plate assembly from the target with sensors is suggested.

B

Impact Data

In this appendix the data that was used for the thesis is presented. A first table shows for each experiment the material of the projectile, the target type, the speed of impact, the voltage of the accelerator, the impact speed and momentum and the maximum voltage picked up by the sensors. The second table shows, for a select number of experiments, the impact momentum p, the maximum voltage detected V, the voltage corrected for the effect of dissipation (as described in section 8.2) indicated as V_0, the estimated momentum p_{est} based on the linear fit (chapter 8) and an average of the estimated momentum from the four sensors, compared to the measured momentum.

Parameter	Target	Projectile	Speed	Accelerator Voltage	Mass of the projectile	Impact Momentum	Max Voltage A	Max Voltage B [V]	Max Voltage C [V]	Max Voltage D [V]	Max Voltage G [V]
Unit	[-]	[-]	[m/s]	[V]	[g]	[gm/s]	[V]	[V]	[V]	[V]	[V]
impacts on aluminium											
2	Al	glass	20.00	5.50	0.04	0.80	1.49	5.0-	4.20	2.82	
3	Al	glass	37.84	7.00	0.04	1.51	2.05	7.22	5.56	4.23	
4	Al	glass	13.36	3.60	0.04	0.53	0.69	2.20	1.50	1.65	
5	Al	glass	12.72	3.60	0.04	0.51	0.63	2.99	2.01	1.72	
6	Al	glass	210.00	8.60	0.04	8.40	2.12	12.02	7.71	6.34	
7	Al	glass	30.00		0.04	1.20	1.86	10.09	6.63	5.53	
8	Al	glass	63.06		0.04	2.52	2.49	14.72	7.09	6.13	
9	Al	glass	61.58	8.50	0.04	2.46	0.18	Inf	8.58	8.46	
10	Al	glass	-	8.00	0.04		0.05	0.10	0.08	0.05	
11	Al	glass	-		0.04		0.00	0.00	0.00	0.00	
12	Al	glass	58.82	7.50	0.04	2.35	6.92	Inf	9.23	7.42	
13	Al	glass	90.13	10.20	0.04	3.61	10.41	17.56	13.31	11.81	
14	Al	glass	91.30	13.00	0.04	3.65	10.31	17.44	9.19	12.28	
15	Al	glass	21.15	3.50	0.04	0.85	3.16	0.96	2.96	3.02	
16	Al	glass	16.27	3.50	0.04	0.65	0.00	0.00	0.00	0.00	
17	Al	Steel	18.26	3.50	0.11	1.99	3.21	Inf	Inf	3.87	
18	Al	Steel	79.85	10.00	0.11	8.70	0.00	0.00	0.00	0.00	
19	Al	glass	16.27	2.00	0.04	0.65	0.00	0.00	0.00	0.00	
20	Al	glass	8.33	2.00	0.04	0.33	0.84	1.08	0.89	0.78	
25	Al	Steel	10.75	2.50	0.11	1.17	1.82	2.36	3.05	2.16	
26	Al	Steel	23.60	3.70	0.11	2.57	4.45	Inf	Inf	Inf	
27	Al	Steel	16.71	3.40	0.11	1.82	3.42	4.26	4.17	3.11	
28	Al	Steel	34.94	5.30	0.11	3.81	7.67	Inf	8.42	6.25	
29	Al	Steel	30.43	7.20	0.11	3.32	5.84	11.56	7.13	7.38	
30	Al	Steel	43.03	7.00	0.11	4.69	4.04	6.07	6.43	5.12	
31	Al	Steel	53.16	8.50	0.11	5.79	4.24	10.18	6.08	4.81	
32	Al	Steel	-	10.20	0.11		0.00	0.00	0.00	0.00	
33	Al	Steel	96.77	11.50	0.11	10.55	25.49	21.62	27.84	17.37	
34	Al	Steel	107.69	12.50	0.11	11.74	8.97	13.00	13.42	12.70	
35	Al	Steel	107.69	13.50	0.11	11.74	16.46	14.21	15.18	16.74	
36	Al	glass	-		0.04						
tests with high speed camera						0.00					
38	Al	PTFE	25.93	5.00	0.03	0.86					
39	Al	PTFE	20.85	4.00	0.03	0.69					
40	Al	glass	41.34	8.00	0.04	1.65					
41	Al	PTFE	101.45	10.00	0.03	3.35	2.19	3.23	2.37	2.23	
42	Al	glass	106.87	15.00	0.04	4.27	9.91	7.91	7.63	15.73	
comparative shots: same kinetic energy						0.00	0.00	0.00	0.00	0.00	
44	Al	PTFE	37.30	6.00	0.03	1.23	0.83	1.38	0.94	0.68	
45	Al	PTFE	42.42	6.00	0.03	1.40	0.82	1.44	1.03	0.92	
46	Al	glass	16.06	6.00	0.04	0.64	2.19	1.37	1.52	3.99	
47	Al	PTFE	32.61	6.00	0.03	1.08	4.23	3.10	3.33		
48	Al	PTFE	43.03	7.00	0.03	1.42	0.00	0.00	0.00	0.00	
49	Al	glass	36.21	7.00	0.04	1.45	4.40	3.88	3.17		
impacts on sandwich panel						0.00	0.00	0.00	0.00	0.00	
51	Sandwich	glass	45.85	6.00	0.04	1.83	1.19	0.98	0.94	1.03	
52	Sandwich	glass	29.09	5.00	0.04	1.16	0.78	0.74	0.70	0.66	0.65

53	Sandwich	blank		5.00			0.05	0.08	0.07	0.09	0.07
54	Sandwich	blank		5.00			0.10	0.14	0.23	0.36	0.19
55	Sandwich	blank		5.00			0.03	0.10	0.13	0.16	0.10
56	Sandwich	glass	28.00	5.00	0.04	1.12	1.47	0.77	0.39	0.55	1.79
57	Sandwich	PTFE	25.93		0.03	0.86	0.00	0.00	0.00	0.00	0.00
58	Sandwich	steel	31.20	6.00	0.11	3.40	2.62	1.39	0.70	1.23	3.63
59	Sandwich	PTFE	51.22	8.50	0.03	1.69	1.22	1.94	0.59	0.60	0.75
60	Sandwich	PTFE	80.46	11.00	0.03	2.66	1.09	1.41	0.98	0.83	1.20
61	Sandwich	PTFE	85.02	13.00	0.03	2.81	2.14	2.70	0.72	0.78	1.21
62	Sandwich	steel	66.67	10.00	0.11	7.27	1.91	1.58	1.42	2.21	2.27
63	Sandwich	regolith		5.00			0.04	0.06	0.04	0.06	0.05
64	Sandwich	regolith		5.00			0.01	0.02	0.02	0.02	0.03
65	Sandwich	glass	25.70	5.00	0.04	1.03	0.71	0.91	0.45	0.34	0.56
66	Sandwich	glass	37.97		0.04	1.52	1.30	0.94	0.45	0.76	1.43
67	Sandwich	glass	41.53		0.04	1.66	0.76	1.71	0.70	0.43	0.63
68	Sandwich	glass	65.63		0.04	2.63	1.79	1.70	0.77	0.63	0.78
69	Sandwich	glass	70.88		0.04	2.84	1.62	1.76	0.74	0.72	0.88
70	Sandwich	glass	96.66		0.04	3.87	2.12	1.86	0.60	0.69	1.21
71	Sandwich	glass	37.31		0.04	1.49	0.55	2.00	0.84	0.31	0.49
72	Sandwich	glass	59.02		0.04	2.36	0.77	3.65	0.94	0.44	0.66
73	Sandwich	glass	133.02		0.04	5.32	0.57	0.46	0.69	0.80	0.48
74	Sandwich	glass	41.06		0.04	1.64	0.89	1.09	0.71	0.67	0.69
75	Sandwich	glass	66.82		0.04	2.67	1.26	1.28	0.86	0.89	0.87
76	Sandwich	glass	130.33		0.04	5.21	1.67	2.01	0.95	1.56	1.45
77	Sandwich	hot glue	123.53			0.00	0.99	1.42	0.82	1.03	1.23
78	Sandwich	glass	13.04		0.04	0.52	0.43	0.51	0.47	0.29	0.32
79	Sandwich	glass	31.20		0.04	1.25	0.93	1.04	0.72	0.45	0.74
80	Sandwich	glass	38.96		0.04	1.56	1.13	1.35	0.86	0.57	0.92
81	Sandwich	glass	40.38		0.04	1.62	1.11	1.41	0.52	0.52	0.79
82	Sandwich	glass	58.33		0.04	2.33	0.00	0.00	0.00	0.00	0.00
83	Sandwich	glass	-		0.04	#VALUE!	1.40	1.82	1.28	0.80	1.20
84	Sandwich	glass	-		0.04	#VALUE!	0.46	0.62	0.67	0.69	0.40
85	Sandwich	glass	-		0.04	#VALUE!	1.71	1.46	1.36	1.12	1.14
86	Sandwich	glass	-		0.04	#VALUE!	1.36	0.97	1.64	0.74	0.47
87	Sandwich	blank	-			#VALUE!	0.01	0.02	0.03	0.03	0.03
88	Sandwich	PTFE	32.46		0.03	1.07	0.80	0.93	0.34	0.41	0.63
89	Sandwich	PTFE	15.60		0.03	0.51	0.50	0.38	0.39	0.25	0.40
90	Sandwich	PTFE	40.54		0.03	1.34	0.96	0.98	0.59	0.57	0.75
91	Sandwich	PTFE	40.94		0.03	1.35	0.90	0.98	0.38	0.55	0.77
92	Sandwich	PTFE	44.03		0.03	1.45	1.00	1.09	0.66	0.66	0.85
93	Sandwich	PTFE	65.83		0.03	2.17	1.43	1.43	0.60	0.69	1.14
94	Sandwich	PTFE	83.00		0.03	2.74	1.10	1.65	1.24	0.80	1.07
95	Sandwich	PTFE	15.96		0.03	0.53	0.40	0.51	0.23	0.25	0.36
96	Sandwich	PTFE	23.84		0.03	0.79	0.66	0.63	0.45	0.37	0.52
97	Sandwich	steel	28.97		0.11	3.16		1.47	0.65	0.87	1.72
98	Sandwich	steel	11.97		0.11	1.30	0.98	1.00	0.41	0.51	0.73
99	Sandwich	steel	58.66		0.11	6.39	2.60	2.52	1.31	1.34	2.32
100	Sandwich	dust analogue	75.27		0.01	0.38	0.38	0.50	0.35	0.20	0.27
101	Sandwich	steel	70.00		0.11	7.63	2.51	2.46	1.42	1.32	2.56
102	Sandwich	steel	45.55		0.11	4.97	2.12	2.23	1.14	1.21	1.91
103	Sandwich	steel	-		0.11		0.00	0.00	0.00	0.00	0.00
104	Sandwich	steel	-		0.11		0.00	0.00	0.00	0.00	0.00
1	Solar Panel	glass	-		0.04	-	0.02	0.01	0.01	0.03	
2	Solar Panel	glass	-		0.04	-	0.01	0.06	0.05	0.20	

3	Solar Panel	glass	50.00	7.50	0.04	2.00	0.01	0.06	0.05	0.20	
4	Solar Panel	glass	52.00	7.50	0.04	2.08	0.02	0.04	0.03	0.20	
5	Solar Panel	glass	70.00	10.00	0.04	2.80	0.03	0.05	0.09	0.37	
6	Solar Panel	glass	70.00	10.00	0.04	2.80	0.02	0.08	0.14	0.50	
7	Solar Panel	glass	90.00	12.50	0.04	3.60	0.01	0.07	0.10	0.51	
8	Solar Panel	glass	95.00	12.50	0.04	3.80	0.02	0.08	0.09	0.32	
9	Solar Panel	glass	40.00	5.00	0.04	1.60	0.01	0.04	0.05	0.19	
10	Solar Panel	glass	38.00	5.00	0.04	1.52	0.01	0.04	0.05	0.16	
11	Solar Panel	steel	39.00	5.00	0.11	4.25	0.00	0.00	0.00	0.00	
12	Solar Panel	steel	51.00	5.00	0.11	5.56	0.00	0.09	0.11	0.18	
13	Solar Panel	steel	53.00	7.50	0.11	5.78	0.03	0.13	0.17	0.35	
14	Solar Panel	steel	70.00	7.50	0.11	7.63	0.03	0.10	0.14	0.25	
15	Solar Panel	steel	70.00	10.00	0.11	7.63	0.03	0.09	0.18	0.22	
16	Solar Panel	steel	90.00	10.00	0.11	9.81	0.04	0.14	0.09	0.19	
17	Solar Panel	steel		12.50	0.11		0.03	0.10	0.11	0.27	
18	Solar Panel	steel		12.50	0.11		0.04	0.08	0.10	0.16	

Table 1

Data Number	Max Voltage A [V]	Max Voltage B [V]	Max Voltage C [V]	Max Voltage D [V]	p [gm/s]	V0 A [V]	V0 B [V]	V0 C [V]	V0 D [V]	p_est A [g m/s]	p_est B [g m/s]	p_est C [g m/s]	p_est D [g m/s]	p_est_avg [gm/s]	p_est_avg/p [-]		
	[V]	[V]	[V]	[V]	[gm/s]	[V]	[V]	[V]	[V]	[gm/s]	[gm/s]	[gm/s]	[gm/s]	[gm/s]	[-]		
Sandwich panel data																	
61	2.14	2.70	0.72	0.78	3.45	32.26	50.96	18.58	22.46	3.64	3.28	2.17	2.84	2.98	0.87		
65	0.71	0.91	0.45	0.34	1.03	10.75	17.15	11.76	9.69	1.21	1.10	1.37	1.23	1.23	1.20	Average p_est_avg/p [-]	1.04589
66	1.30	0.94	0.45	0.76	1.52	19.70	17.76	11.69	21.80	2.23	1.14	1.37	2.76	1.87	1.23	STD p_est_avg/p [-]	0.19365
67	0.76	1.71	0.70	0.43	1.66	11.55	32.18	18.17	12.43	1.31	2.07	2.12	1.57	1.77	1.06		
68	1.79	1.70	0.77	0.63	2.63	26.99	32.01	19.85	18.20	3.05	2.06	2.32	2.31	2.43	0.93		
69	1.62	1.76	0.74	0.72	2.84	24.54	33.16	19.25	20.79	2.77	2.13	2.25	2.63	2.45	0.86		
70	2.12	1.86	0.60	0.69	3.87	32.05	35.01	15.66	19.79	3.62	2.25	1.83	2.51	2.55	0.66		
71	0.55	2.00	0.84	0.31	1.49	8.27	37.66	21.79	8.83	0.93	2.42	2.55	1.12	1.76	1.18		
72	0.77	3.65	0.94	0.44	2.36	11.57	68.82	24.29	12.53	1.31	4.43	2.84	1.59	2.54	1.08		
78	0.43	0.51	0.47	0.29	0.64	6.45	9.61	12.24	8.32	0.73	0.62	1.43	1.05	0.96	1.50		
79	0.93	1.04	0.72	0.45	1.53	13.98	19.63	18.63	12.90	1.58	1.26	2.18	1.63	1.66	1.09		
80	1.13	1.35	0.86	0.57	1.91	17.03	25.42	22.31	16.26	1.92	1.64	2.61	2.06	2.06	1.07		
81	1.11	1.41	0.52	0.52	1.98	16.84	26.66	13.55	14.90	1.90	1.72	1.58	1.89	1.77	0.89		
88	0.80	0.93	0.34	0.41	1.31	12.10	17.43	8.81	11.88	1.37	1.12	1.03	1.50	1.26	0.96		
89	0.50	0.38	0.39	0.25	0.63	7.55	7.12	10.02	7.10	0.85	0.46	1.17	0.90	0.85	1.34		
90	0.96	0.98	0.59	0.57	1.64	14.51	18.48	15.31	16.26	1.64	1.19	1.79	2.06	1.67	1.02		
91	0.90	0.98	0.38	0.55	1.66	13.65	18.41	9.87	15.68	1.54	1.18	1.15	1.99	1.47	0.88		
92	1.00	1.09	0.66	0.66	1.78	15.16	20.49	17.15	18.87	1.71	1.32	2.00	2.39	1.86	1.04		
93	1.43	1.43	0.60	0.69	2.67	21.62	26.93	15.51	19.79	2.44	1.73	1.81	2.51	2.12	0.80		
95	0.40	0.51	0.23	0.25	0.64	6.09	9.52	5.95	7.07	0.69	0.61	0.70	0.89	0.72	1.12		
96	0.66	0.63	0.45	0.37	0.97	9.98	11.89	11.76	10.53	1.13	0.77	1.37	1.33	1.15	1.19		